

Design and Construction of Water Oxidation Systems via

Rational Assembly of Molecular Catalyst

触媒分子の戦略的配列による

酸素発生触媒システムの設計と構築

Hikaru Iwami

The Graduate University for Advanced Studies, SOKENDAI

School of Physical Sciences

Department of Structural Molecular Science

March 2021

Contents

General Introduction	5
Chapter 1	
Electrochemical Polymerization Provides a Function-Integrated System for Water Oxidation	27
Chapter 2	
Facile Construction of Function-Integrated Water Oxidation System via Electrochemical Polymerization	61
Chapter 3	
Construction of Self-Assembled Frameworks of Cubane-Type Tetranuclear Cobalt Complexes	89
Concluding Remarks	114
Acknowledgement	115

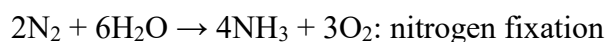
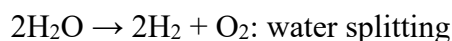
General Introduction

Water oxidation in artificial photosynthesis

Increasing global energy consumption is an urgent issue from the viewpoint of the limited fossil energy resources. Meeting such global energy demand, sustainable and clean energy production has been highly required in recent years.[1] In this context, artificial photosynthesis has attracted considerable attention as one of the methodologies to achieve sustainable and clean energy production. Artificial photosynthesis is a concept established by mimicking the natural photosynthetic system. Therefore, initially, a brief introduction of natural photosynthesis will be given.

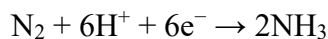
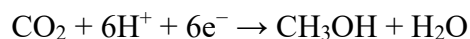
Natural photosynthetic system is capable of converting solar energy to chemical energy sources. In the scheme of natural photosynthesis, CO_2 is reduced to carbohydrates ($6\text{CO}_2 + 12\text{H}_2\text{O} \rightarrow \text{C}_6\text{H}_{12}\text{O}_6 + 6\text{O}_2 + 6\text{H}_2\text{O}$), and the formed carbohydrates are used as chemical energy (i.e. fossil fuels), which is important to human society. The considerable feature of natural photosynthesis is that the useful chemical energy sources are produced from abundant sources, CO_2 and H_2O , with the assistance of solar energy.

In artificial photosynthetic systems, several chemical energy sources can be generated from earth-abundant sources. The following equations are typical examples of artificial photosynthesis reactions.

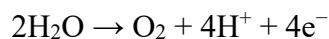


Evidently, the production of chemical energy (H_2 , CH_3OH , and NH_3) from the earth-abundant sources (H_2O , CO_2 , and N_2) can be achieved in artificial photosynthetic reactions. Importantly, these reactions can essentially be divided into two half reactions; reduction and oxidation reactions. The following equations show the half reactions that consist artificial photosynthetic reactions.

<Reduction reactions>



<Oxidation reaction>



Reduction reaction can produce chemical energy sources and require protons and electrons. For supplying the protons and electrons from abundant resources, oxidation reaction, four-electron oxidation of water ($2\text{H}_2\text{O} \rightarrow \text{O}_2 + 4\text{H}^+ + 4\text{e}^-$) is essential.[2] In other words, four-electron oxidation of water is indispensable to construct the artificial photosynthetic system. However, this reaction is an energetically difficult because the O-O bond formation with the loss of four protons and four electrons is involved.[3] Therefore, water oxidation requires high potential and occurs at +1.23 V vs. NHE in pH 0 (Eq. 1).



For the aforementioned reasons, water oxidation reaction is considered the bottleneck of artificial photosynthesis, and the development of an efficient water oxidation catalyst is highly desired.

Water oxidation in natural photosynthetic system

In nature, water oxidation reaction is catalyzed by a metal-complex-based catalyst, the oxygen evolving complex (OEC) embedded in photosystem II (PSII, Figure 1).[4] The OEC is known as a highly active and robust catalyst that can drive water oxidation reaction under mild conditions. The structure of OEC is clarified by X-ray crystallographic and spectroscopic studies.[5] The OEC has a cubane-like represented as CaMn_4O_4 , which is supported by several amino acid residues (Figure 2). In the water oxidation catalyzed by the OEC, not only the catalytic center (CaMn_4O_4 cluster), but also the surrounding amino acid residues play important roles. As shown in Figure 3, photosynthesis is initiated by the absorption of light at the chlorophyll P_{680} . Consequently, the charge-separated $\text{P}_{680}^+ \text{-Pheo}_A^-$ state is formed. The generated hole is transported to the OEC, while the electron is transferred to the plastoquinone.[6] The existence of these charge transporting paths is essential to promote the catalysis efficiently, and the amino acid residues around the OEC greatly contribute to constructing the charge transport pathways. Collectively, the synergetic effect of the catalytic center and charge transporting units is one of considerable factors for efficient water oxidation in natural photosynthetic systems.

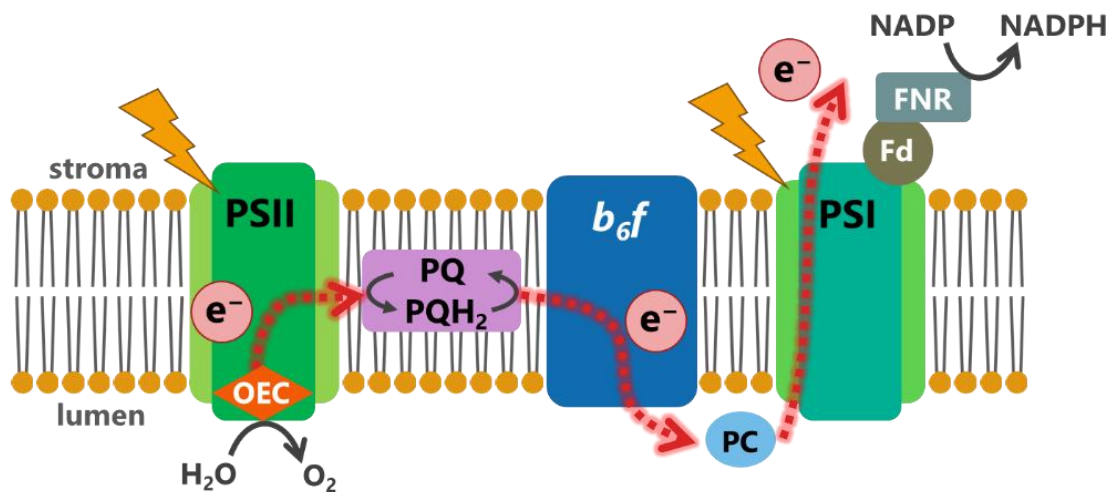


Figure 1. An overview of natural photosynthetic system.

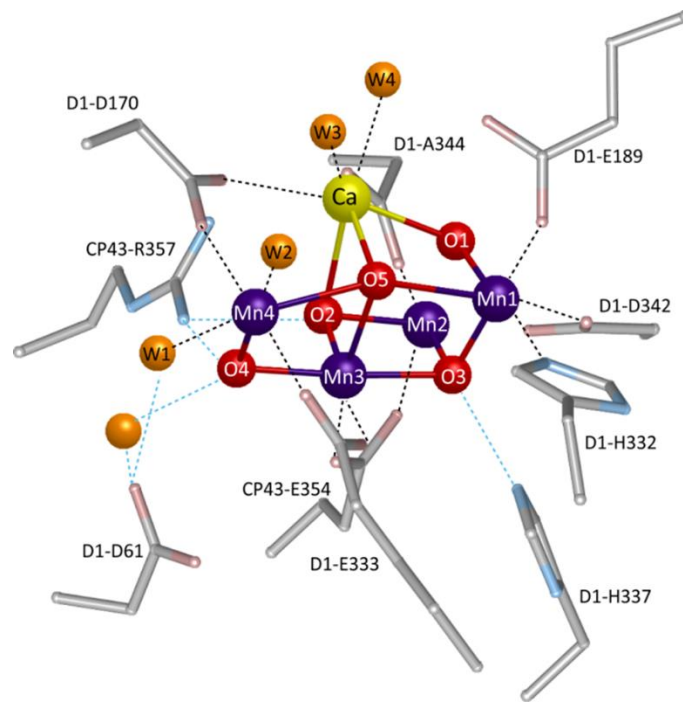


Figure 2. The structure of the CaMn_4O_4 cluster and its ligand environment in the OEC. Manganese: purple, calcium: yellow, oxygen: red, oxygen atoms in water molecules: orange.

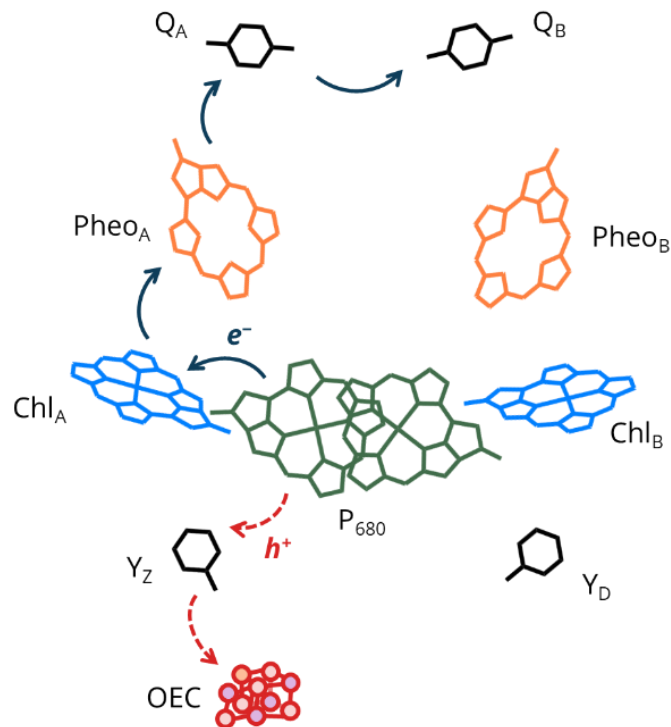


Figure 3. A diagram of charge transfer reactions in PSII.

In addition, there is another key for achieving efficient water oxidation in PSII. As shown in Figure 4, the OEC is located at the node of five water channels. Water molecules form hydrogen-bonded networks, and these water channels play the role of proton release, balancing the net charge of OEC, and supply of substrate water.[7] Therefore, the substrate inlet and the product outlet also contribute efficient water oxidation reaction. In other words, the construction of a reaction field suitable for catalysis is also essential to drive water oxidation efficiently.

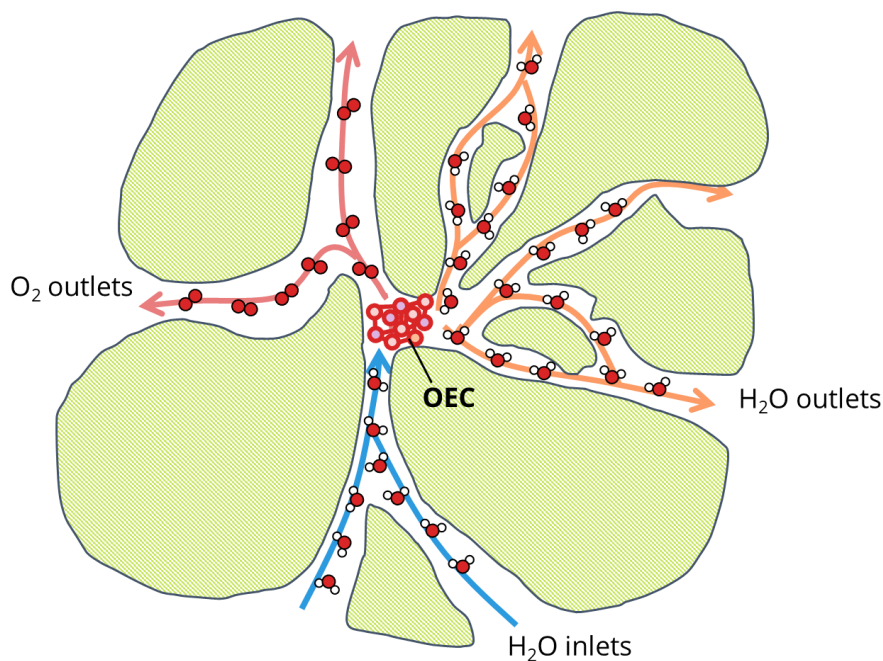


Figure 4. A schematic illustration of water inlets/outlets and oxygen outlets in PSII.

Molecular-based water oxidation catalysts

As described in the first section of this chapter, water oxidation reaction is at the heart of artificial photosynthesis, and the development of highly active catalysts for the reaction is highly desired. In this context, a lot of efforts have been devoted to the development of the molecule-based catalytic system for water oxidation since the discovery of the first example of such a catalyst, “blue dimer” (**1**, Figure 5) in 1982.[8] The blue-dimer has two ruthenium centers bridged by a μ -oxo moiety and exhibits a strong electronic coupling between the two ruthenium centers. Due to such features of the complex, the high oxidation states can be stabilized, which contributes to the promotion of catalytic water oxidation.[9] Inspired by the discovery of the blue dimer and the natural water oxidation catalyst, the OEC, it was considered that multi-nuclear structures are favorable for water oxidation reaction. There have been several examples of molecule-based artificial water oxidation catalysts, which has more than two metal ions (Figure 5). In the case of multi-nuclear metal complexes, ruthenium, manganese, iron, cobalt, and copper complexes have been investigated.[8, 10-16] The turnover frequency reached up to $1,900 \text{ s}^{-1}$ for the pentanuclear iron complex (**8**, Figure 5),[16] which is considerably higher than the reaction rate of the OEC ($\sim 400 \text{ s}^{-1}$).[17]

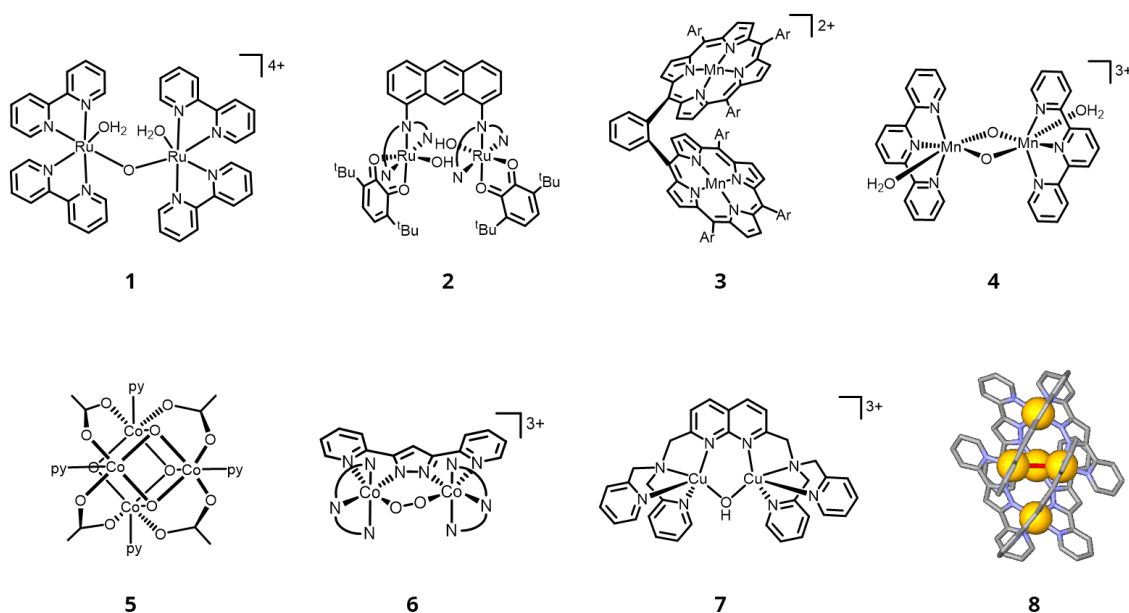


Figure 5. Typical multi-nuclear complexes for catalytic water oxidation. N[^]N[^]N = terpyridine, py = pyridine.

Because of the multi-nuclear feature of OEC, it was long considered that a multi-nuclear core is essential to promote four-electron oxidation of water. However, in 2005, Thummel and co-workers reported the single-site metal complexes which could catalyze four-electron oxidation of water (**9**, Figure 6).[18] The discovery of the water oxidation catalysts with a single ruthenium center is regarded as a paradigm shift for this field. As a result, the studies on single-site catalysts for water oxidation begun to be widely explored. At the present day, various mononuclear catalysts for water oxidation are widely investigated, and complexes with ruthenium, iridium, manganese, iron, cobalt, and copper ions are reported.[18-25]

As described above, there are a large number of molecule-based water oxidation catalysts reported so far.[26] However, these studies mainly focus on the development of catalytic centers and the synergetic effect of catalytic center and charge transporting unit or reaction field have not been explored.

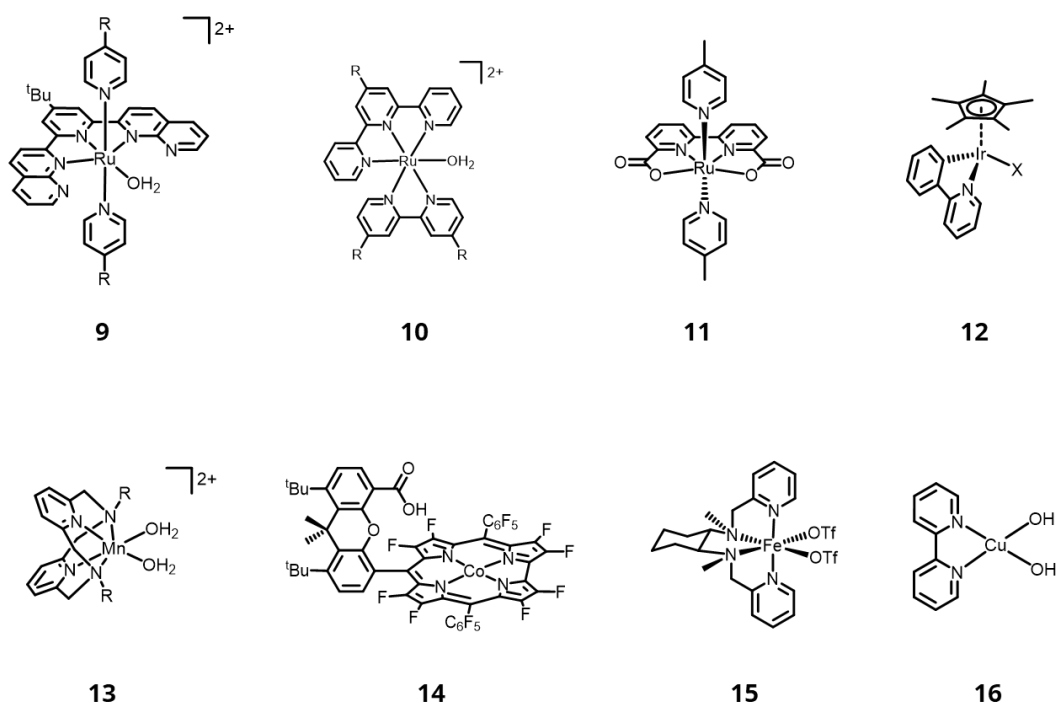


Figure 6. Typical mononuclear complexes for catalytic water oxidation.

Function-integrated systems for water oxidation

Inspired by the natural system, artificial catalytic systems for water oxidation in which two kinds of functions are integrated have attracted interests in recent years. In these studies, molecular-based catalysts are used as catalytic centers and are combined with an extra functional material (i.e. conductive supports, photosensitizers, porous supports, etc.) to form multi-functional catalytic systems. By combining two or more functional units into one system, synergistic effects between these units could be achieved, and the effect enables enhancement of catalytic activity and/or promotion of catalytic reaction under milder conditions. Several examples of such function-integrated systems are described below.

(i) Grafting catalysts on the surface of conductive supports

In water oxidation reaction, strong chemical oxidants (ex. cerium ammonium nitrate) are commonly required to generate catalytically active species. However, the use of strong oxidants is environmentally unfavorable. In contrast, electrochemical water oxidation can proceed without these reagents, and the reaction is considered as one of the promising processes for clean energy production. Generally, heterogeneous catalysts are favorable for the electrochemical process because of good electrical contact with substrates without considering diffusion, and reusability of the catalysts. Therefore, lots of efforts have been devoted to heterogenizing molecule-based catalysts by immobilizing such catalysts on the surface of conductive supports.

The methods to immobilize catalysts onto the electrode can be divided into three categories: loading through covalent bonds, noncovalent interactions, and ionic interactions.[27] For the covalent bindings, anionic functional groups such as carboxylates, phosphates, silica are widely used to form covalent bonds (Figure 7a). In addition, catalyst immobilization methods by bond formation via chemical reactions of diazonium salts, click reaction, and aryl radicals were also reported (Figure 7b-d).[27a]

On the other hand, catalyst bindings with non-covalent interactions were generally reported for carbon-based supports (i.e. carbon nanotubes and graphene) by π - π or hydrophobic interactions.[28] Typically, aromatic carbon surfaces like pyrene and carbon nanotubes are modified on the surface of the electrode.

In the case of ionic binding, substrates are functionalized with ionic groups. Subsequently, the substrates are immersed in the catalyst solution.[29] Therefore, it is required that catalyst molecules are ionic.

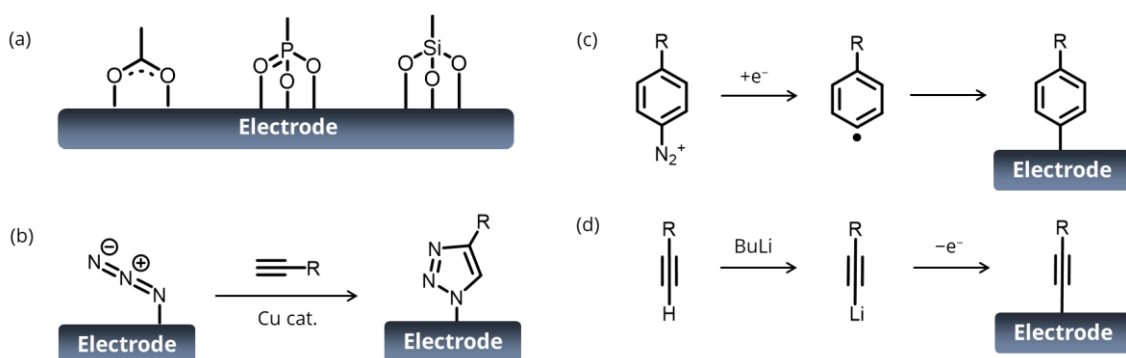


Figure 7. (a) Typical functional groups for surface modification. (b-d) Catalyst immobilization methods by bond formation via chemical reactions.

Focused on the electrocatalytic water oxidation reaction, covalent and non-covalent bindings of catalysts have been commonly investigated. In most cases, turnover number (TON) was enhanced by the immobilization of molecular catalysts as shown in Figure 8.[27,30-33] For an extended approach, Meyer and coworkers reported that the assembly of the redox mediator and water oxidation catalyst immobilized on the surface of the electrode in 2009. The catalytic ability was improved compared with the electrode without redox mediators (Figure 9a).[34] As one of the prominent studies, the hybrid catalyst system composed of a mononuclear ruthenium complex bearing pyrene moieties and multi-walled carbon nanotubes deposited on glassy carbon electrode showed excellent water oxidation ability with a maximum TON of 670,000 (Figure 9b),[35] which is reported by Llobet *et al.* in 2016. However, in this system, the current was gradually decreased during electrolysis, which indicated the deactivation of the complex attributed to the oxidation of methylene linkers. In contrast, the modified anode shown in Figure 9c successfully suppressed the loss of current during catalysis.[35] Therefore, the design of the linker groups is also an important factor for catalysts immobilization.

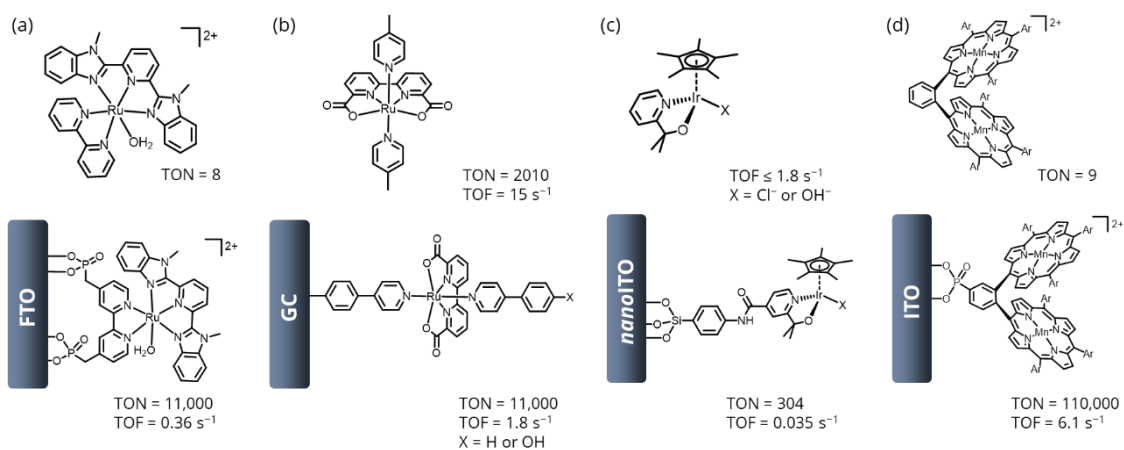


Figure 8. Examples of immobilized catalysts on the electrodes for water oxidation.

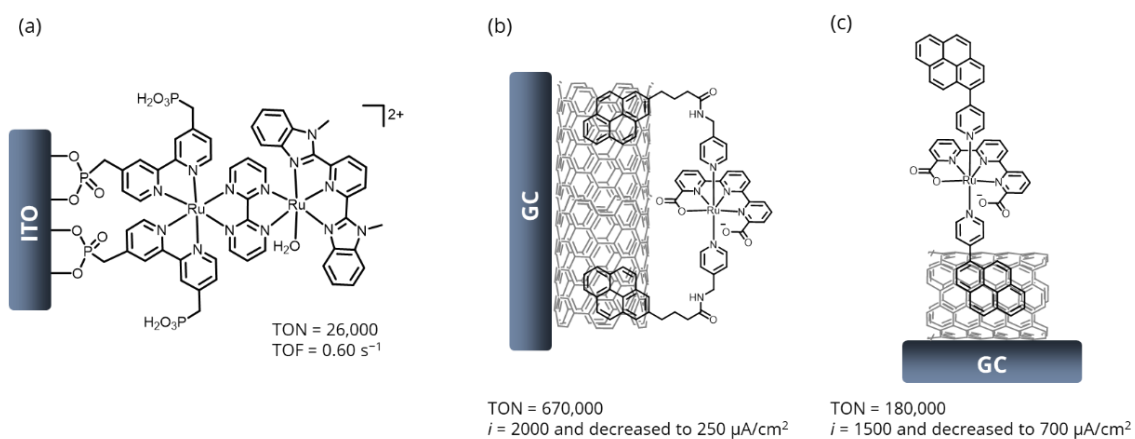


Figure 9. Examples of hybrid electrocatalyst systems by surface modifications.

It should be mentioned that electrochemical polymerization is an effective method for attaching catalysts onto electrodes. Early reports on electropolymerization were in the 1980s,[36] and examples of applications for water oxidation have been increasing recently.[37] Typically, pyrrole or vinyl substituents are used as a polymeric backbone (Figure 10), and the solubility decrease drives surface functionalization with the polymers.

As described above, the incorporation of molecule-based catalysts and conductive substrates is one of the efficient approaches, which can make a heterogenized catalytic system and improve the catalytic performance.

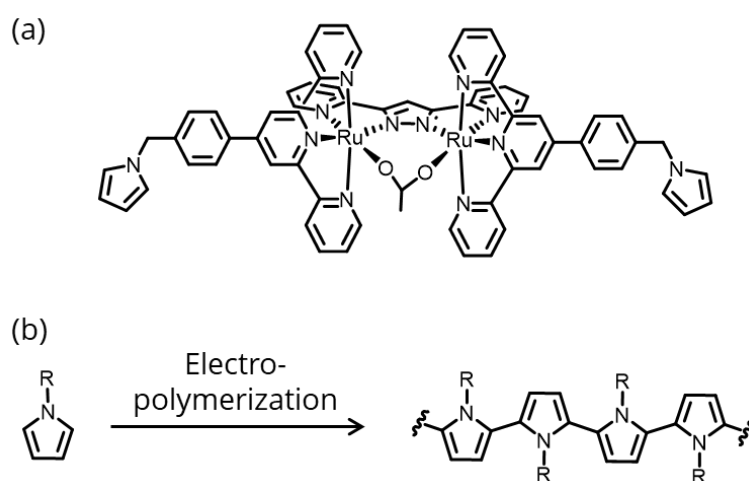


Figure 10. (a) Structure of the catalyst which polymerize under oxidative condition.[37a]
(b) Scheme of electropolymerization of substituted pyrrole.

(ii) Photosensitizing electrocatalysts

The conversion of solar energy to chemical energy is the goal of artificial photosynthesis. For this purpose, the construction of photosensitizing catalyst systems is a valuable approach. The examples described below are photoelectrocatalysts which are one of the photosensitizing systems. Photoelectrocatalysts can drive catalytic reaction at lower potential under photo irradiation.

Photosensitizing electrocatalysts are comprised of photosensitizers and catalytic centers. Both semiconductors and molecule-based dyes are available for light-absorbing materials. Semiconductors have the advantages of good stability and charge separation ability. Generally, semiconductor materials are deposited on the electrode. Subsequently, molecular catalysts are immobilized on the surface of the semiconductor using the method as described in the previous section. There are some reports on the assembly of semiconductor photoanodes and molecular catalysts, so far.[38] On the other hand, all molecular-based photoelectrocatalysts could be constructed by the electro assembly of chromophores and catalysts (Figure 11).[39] Regardless of the kind of photosensitizers, the photocurrent was observed and the onset potential was decreased under the light illumination.

Collectively, photosensitizing electrocatalysts enable the integration of catalytic centers and photosensitizing units and thus are regarded as one of function-integrated systems.

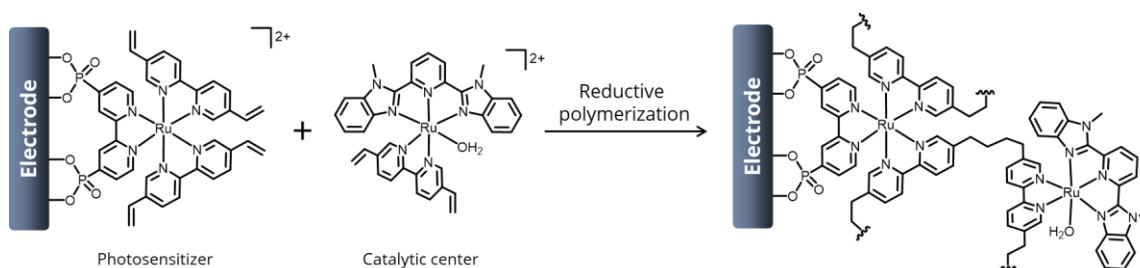


Figure 11. An example of all molecular-based photosensitizer-catalyst assembly for water oxidation.[39a]

(iii) Water oxidation catalysts derived from porous materials

In the viewpoint of the construction of the substrate transfer path (and reaction field), porous materials have been attracted for the platform of catalysis. Recently, metal-organic frameworks (MOFs) have been attracted much attention because of their high porosity and structural flexibility.[40] MOFs are comprised of metal nodes called secondary building units (SBUs) and organic linkers, and numerous combinations provide structural variations of MOFs.

Catalytic water oxidation by MOFs can be divided into two categories: MOF-derived catalysts, and direct MOF-based catalysts.[41] In MOF-derived catalysts, synthesized MOFs are treated by etching, annealing, or secondary growth. Due to these fabrication processes, MOFs act as a sacrificial or self-template. In general, amorphous catalysts are formed with high porosity originated from MOFs. In contrast, direct MOF-based catalysts can be used without the transformation into amorphous materials. SBUs mainly work as catalytic centers, however, the structures of SBUs are usually difficult to control because of the synthetic methods. It is a critical issue for the construction of catalytic centers. For the aforementioned reasons, the reports on MOFs that catalyze water oxidation are limited. Therefore, alternative approaches have been investigated.

It is one of the effective methods that the use of linker molecules which can coordinate another metal ion. For example, 2,2'-bipyridine-5,5'-dicarboxylic acid has two kinds of coordination sites: carboxylates to construct MOFs, and bipyridine structure to form active centers (Figure 12).[42] Although the introduction of catalytic centers is easier than the design of SBUs, the variation of MOFs and catalytic centers are still limited, and porosity must be decreased.

The other method is the encapsulation of catalysts in MOFs. Catalyst molecules can be isolated and stabilized in the pore of MOFs by suppressing deactivation due to recombination of excited states or intermolecular interactions. The catalyst-loaded MOFs are prepared by entrapment of catalyst molecules (Figure 13).[43] However, in the case of the encapsulation of catalysts, the distribution of catalytic centers is difficult to control, and the decrease of porosity is also a disadvantage for catalysis.

Although the utilization of MOFs is an intriguing approach to integrate catalytic centers and mass transport paths, there are several limitations in the development of MOF-based systems for water oxidation as described above.

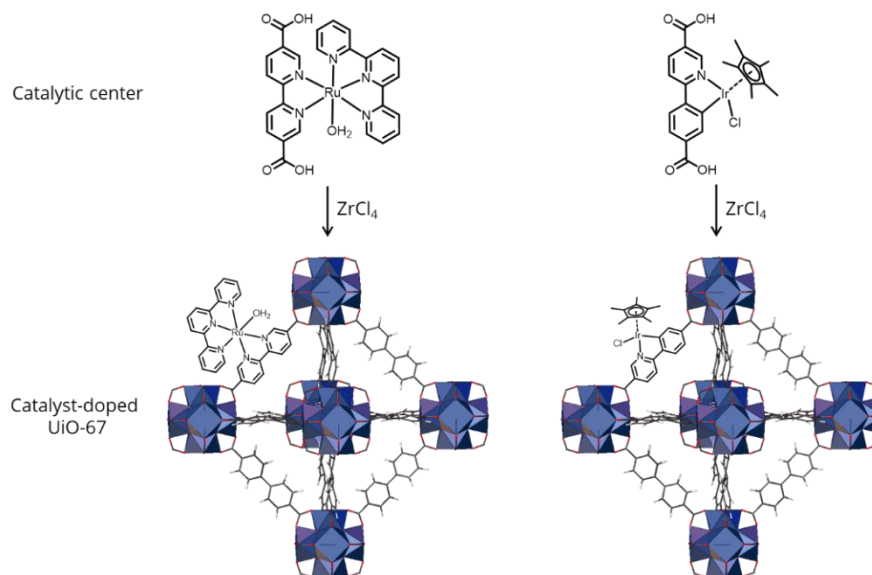


Figure 12. Synthetic scheme of catalyst-doped MOFs with catalyst molecules containing another coordination substituents.

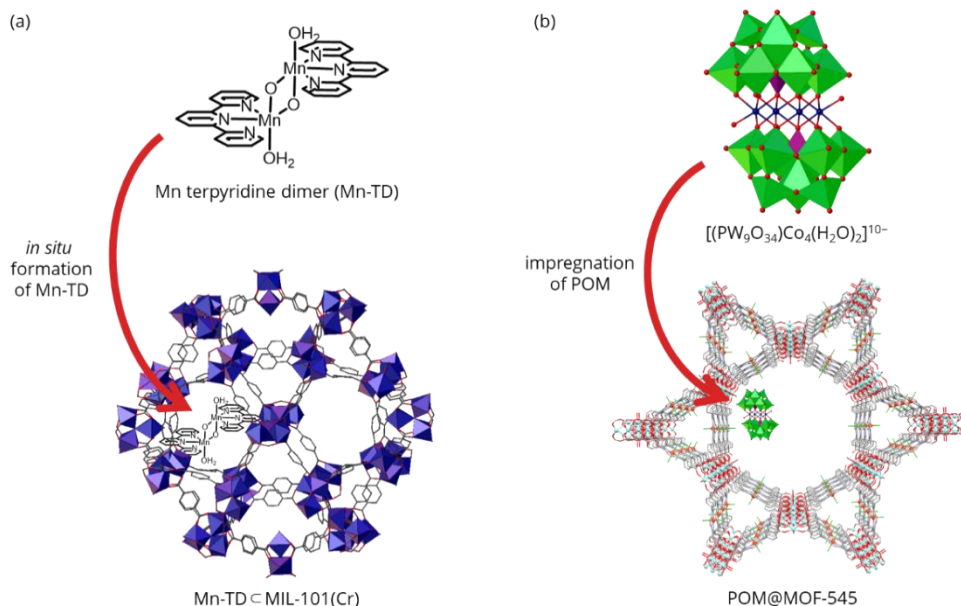


Figure 13. Schemes of reported example that catalyst molecules are encapsulated into MOFs.

Aim of this thesis

As described above, electrocatalytic water oxidation is an important reaction for clean energy production. Although great attention have been devoted to constructing active centers and catalyst composites, there are fewer examples for the construction of the environment surrounding the catalytic centers. In this thesis, I aimed to construct function-integrated systems for water oxidation by a rational assembly of molecular-based catalysts.

Survey of this thesis

Chapter 1 describes the development of electrochemical polymerization-derived electrocatalytic system for water oxidation. Inspired by the natural system, I hypothesized that the integration of charge transporters and catalytic centers would enhance the catalytic activity. Based on this strategy, the function-integrated catalyst module, $\text{Co}_4\text{O}_4(\text{czp})_4(\text{py})_4$ (**1**) (Hczp = carbazole-9-propionic acid, py = pyridine), was newly designed. The catalyst module, **1**, was comprised of two distinct functions: (i) Co_4O_4 cubane-shaped core for water oxidation, (ii) carbazole backbones for the charge transporter and electrochemically polymerizing motif. Cyclic voltammetry (CV) measurement revealed that **1** polymerized under oxidative condition via dimerization of the carbazole moieties. Obtained polymer (**Poly-1**) was further analyzed by electrochemical impedance spectroscopy (EIS) to investigate the charge transport ability. As a result, **Poly-1** showed lower charge transfer resistance than the bare electrode and the non-polymer system. Controlled potential electrolysis experiments showed high catalytic activity of **Poly-1** for water oxidation, which suggested that the introduction of the charge transporting group enhanced the catalytic activity.

Chapter 2 presents the application of function-integrated strategy which demonstrates in chapter 1 to a mononuclear Ru complex. Ru based catalyst module, Ru(bda)(czpy)₂ (**2**) (H₂bda = 2,2'-bipyridine-6,6'-dicarboxylic acid, czpy = 9-[2-(4-pyridinyl)ethyl]carbazole) was designed and synthesized. In a similar manner to **1**, **2** was polymerized during oxidative scans in a CV measurement. Low charge transfer resistance was observed in EIS analysis, and the high electrocatalytic ability for water oxidation was revealed by controlled potential electrolysis. These results clearly demonstrated that the function-integrated strategy is an effective method to enhance electrocatalytic activity and applicable to various metal-complex-based systems.

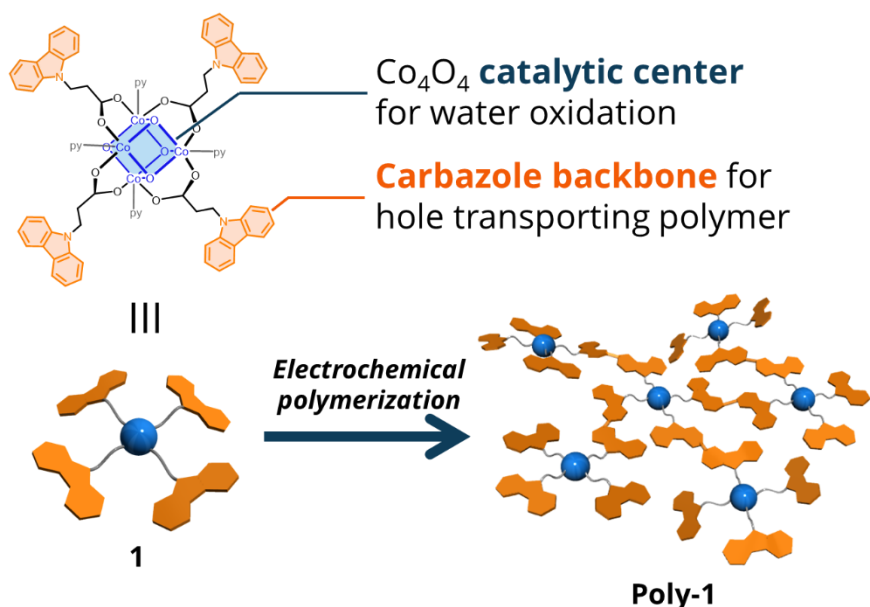


Figure 14. The schematic illustration described in chapter 1.

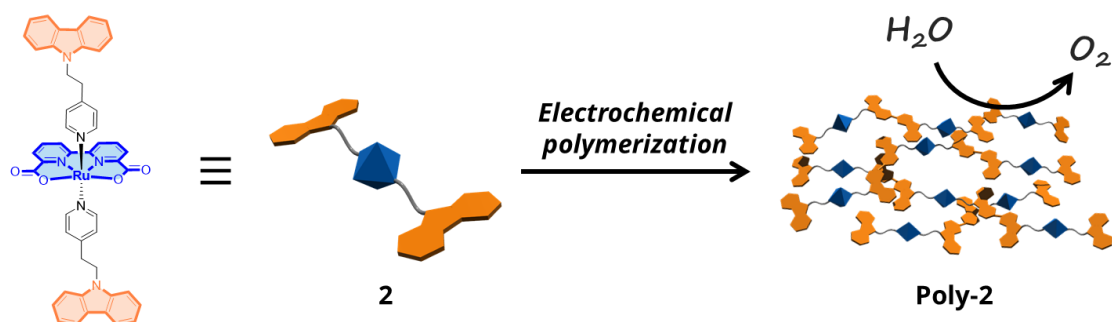


Figure 15. The diagram of the complex **2** investigated in chapter 2.

Chapter 3 reports the construction of the supramolecular framework catalysts driven by the self-assembly of molecular catalysts via noncovalent interactions. 4-[(perfluorophenyl)ethynyl]-benzoic acid (Hppeb) ligand, which has multi-point arene-perfluoroarene (Ar-Ar^F) interaction sites, was introduced into tetranuclear Co complex, Co₄O₄(OAc)₄(py)₄ (HOAc = acetic acid). Two substituted complex, Co₄O₄(OAc)₂(ppeb)₂(py)₄ (**L2**) and four substituted complex, Co₄O₄(ppeb)₄(py)₄ (**L4**) were successfully isolated and characterized by single crystal X-ray diffraction analysis. Moreover, the electrocatalytic activity of the obtained framework was investigated.

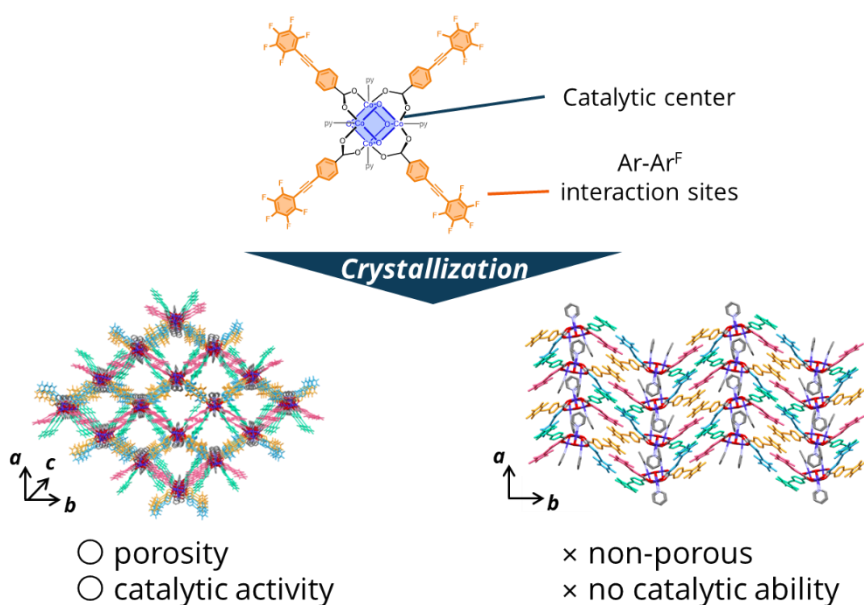


Figure 16. The structure (top) and packing diagrams (bottom) of the complexes studied in chapter 3.

References

- [1] (a) D. G. Nocera, M. P. Nash, *Proc. Natl. Acad. Sci.* **2007**, *104* (43), 15729–15735. (b) P. V. Kamat, *J. Phys. Chem. C* **2007**, *111* (7), 2834–2860. (c) T. R. Cook, D. K. Dogutan, S. Y. Reece, Y. Surendranath, T. S. Teets, D. G. Nocera, *Chem. Rev.* **2010**, *110* (11), 6474–6502.
- [2] (a) X. Liu, F. Wang, *Coord. Chem. Rev.* **2012**, *256*, 1115–1136. (b) A. Singh, L. Spiccia, *Coord. Chem. Rev.* **2013**, *257*, 2607–2622. (c) M. D. Kärkäs, O. Verho, E. V. Johnston, B. Åkermark, *Chem. Rev.* **2014**, *114* (24), 11863–12001. (d) J. D. Blakemore, R. H. Crabtree, G. W. Brudvig, *Chem. Rev.* **2015**, *115*, 12974–13005. (e) M. Kondo, S. Masaoka, *Chem. Lett.* **2016**, *45* (11), 1220–1231. (f) B. Zhang, L. Sun, *Chem. Soc. Rev.* **2019**, *48* (7), 2216–2264. (g) S. Ye, C. Ding, M. Liu, A. Wang, Q. Huang, C. Li, *Adv. Mater.* **2019**, *31* (50), 1902069. (h) Z. N. Zahran, Y. Tsubonouchi, E. A. Mohamed, M. Yagi, *ChemSusChem* **2019**, *12* (9), 1775–1793.
- [3] (a) A. J. Bard, M. A. Fox, *Acc. Chem. Res.* **1995**, *28* (3), 141–145. (b) E. Amouyal, *Sol. Energy Mater. Sol. Cells* **1995**, *38*, 249–276.
- [4] (a) K. N. Ferreira, T. M. Iverson, K. Maghlaoui, J. Barber, S. Iwata, *Science*, **2004**, *303*, 1831–1838. (b) T. J. Meyer, M. H. V. Huynh, H. H. Throp, *Angew. Chem. Int. Ed.* **2007**, *46* (28), 5284–5304.
- [5] (a) Y. Umena, K. Kawakami, J. Shen, N. Kamiya, *Nature* **2011**, *473*, 55–60. (b) M. Saga, F. Akita, G. Ueno, H. Murasugi, Y. Nakajima, T. Shimizu, K. Yamashita, M. Yamamoto, H. Ago, J. Shen, *Nature* **2015**, *517*, 99–103.
- [6] (a) J. P. McEvory, G. W. Brudvig, *Chem. Rev.* **2006**, *106* (11), 4455–4483. (b) J. Barber, *Chem. Soc. Rev.* **2009**, *38* (1), 185–196. (c) F. Rappaport, B. A. Diner, *Coord. Chem. Rev.* **2008**, *252*, 259–272. (d) F. Müh, C. Glöckner, J. Hellmich, A. Zouni, *Biochim. Biophys. Acta Bioenerg.* **2012**, *817* (1), 44–65.
- [7] (a) J. Shen, *Annu. Rev. Plant Biol.* **2015**, *66*, 23–48. (b) N. Sakashita, H. C. Watanabe, T. Ikeda, K. Saito, H. Ishikita, *Biochemistry* **2017**, *56* (24), 3049–3057.
- [8] J. A. Gilbert, D. S. Eggleston, W. R. Murphy Jr, D. A. Geselowitz, S. W. Gersten, D. J. Hodgson, T. J. Meyer, *J. Am. Chem. Soc.* **1985**, *107*(13), 3855–3864.
- [9] P. Doppelt, T. J. Meyer, *Inorg. Chem.* **1987**, *26*(13), 2027–2034.
- [10] T. Wada, K. Tsuge, K. Tanaka, *Angew. Chem. Int. Ed.* **2000**, *39* (8), 1479–1482.

- [11] Y. Naruta, M. Sasayama, T. Sasaki, *Angew. Chem. Int. Ed.* **1994**, *33* (18), 1839-1841.
- [12] J. Limburg, J. S. Vrettos, L. M. Liable-Sands, A. L. Rheingold, R. H. Crabtree, G. W. Brudvig, *Science* **1999**, *283*, 1524-1527.
- [13] N. S. McCool, D. M. Robinson, J. E. Sheats, G. C. Dismukes, *J. Am. Chem. Soc.* **2011**, *133* (30), 11446-11449.
- [14] M. L. Rigsby, S. Mandal, W. Nam, L. C. Spencer, A. Llobet, S. S. Stahl, *Chem. Sci.* **2012**, *3* (10), 3058-3062.
- [15] X. Su, M. Gao, L. Jiao, R. Liao, P. E. M. Siegbahn, J. Cheng, M. Zhang, *Angew. Chem. Int. Ed.* **2015**, *54* (16), 4909-4914.
- [16] M. Okamura, M. Kondo, R. Kuga, Y. Kurashige, T. Yanai, S. Hayami, V. K. K. Praneeth, M. Yoshida, K. Yoneda, S. Kawata, S. Masaoka, *Nature* **2016**, *530*, 465-468.
- [17] G. C. Dismukes, R. Brimblecombe, G. A. N. Felton, R. S. Pryadun, J. E. Sheats, L. Spiccia, G. F. Swiegers, *Acc. Chem. Res.* **2009**, *42* (12), 1935-1943.
- [18] R. Zong, R. P. Thummel, *J. Am. Chem. Soc.* **2005**, *127* (37), 12802-12803.
- [19] (a) M. Yoshida, S. Masaoka, K. Sakai, *Chem. Lett.* **2009**, *38* (7), 702-703. (b) D. J. Wasylenko, C. Genesamoorthy, M. A. Henderson, B. D. Koivisto, H. D. Osthoff, C. P. Berlinguette, *J. Am. Chem. Soc.* **2010**, *132* (45), 16094-16106. (c) M. Yagi, S. Tajima, M. Komi, H. Yamazaki, *Dalton Trans.* **2011**, *40* (15), 3802-3804.
- [20] L. Duan, F. Bozoglian, S. Mandal, B. Stewart, T. Privalov, A. Llobet, L. Sun, *Nat. Chem.* **2012**, *4*, 418-423.
- [21] J. F. Hull, D. Balcells, J. D. Blakemore, C. D. Incarvito, O. Eisenstein, G. W. Brudvig, R. H. Crabtree *J. Am. Chem. Soc.* **2009**, *131* (25), 8730-8731.
- [22] W. Lee, S. B. Muñoz, III., D. A. Dickie, J. M. Smith, *Angew. Chem., Int. Ed.* **2014**, *53* (37), 9856-9859.
- [23] D. K. Dogutan, R. McGuire Jr., D. G. Nocera, *J. Am. Chem. Soc.* **2011**, *133* (24), 9178-9180.
- [24] J. L. Fillol, Z. Codolà, I. Garcia-Bosch, L. Gómez, J. J. Pla, M. Costas, *Nat. Chem.* **2011**, *3*, 807-813.
- [25] S. M. Barnett, K. I. Goldberg, J. M. Mayer, *Nat. Chem.* **2012**, *4*, 498-502.

- [26] (a) H. Yamazaki, A. Shouji, M. Kajita, M. Yagi, *Coord. Chem. Rev.* **2010**, *254*, 2483–2491. (b) M. D. Kärkäs, O. Verho, E. V. Johnston, B. Åkermark, *Chem. Rev.* **2014**, *114* (24), 11863–12001. (c) M. Kondo, S. Masaoka, *Chem. Lett.* **2016**, *45*, 1220–1231. (d) L. Zhang, S. Mathew, J. Hessels, J. N. H. Reek, F. Yu, *ChemSusChem* **2020**, DOI: 10.1002/cssc.202001876.
- [27] (a) R. M. Bullock, A. K. Das, A. M. Appel, *Chem. Eur. J.* **2017**, *23* (32), 7626–7641. (b) F. Li, H. Yang, W. Ji, L. Sun, *Joule* **2018**, *2* (1), 36–60. (c) Z. N. Zahran, Y. Tsubonouchi, E. A. Mohamed, M. Yagi, *ChemSusChem* **2019**, *12* (9), 1775–1793.
- [28] (a) F. Li, L. Li, L. Tong, Q. Daniel, M. Göthelidb, L. Sun, *Chem. Commun.* **2014**, *50* (90), 13948–13951. (b) F. Li, B. Zhang, X. Li, Y. Jiang, L. Chen, Y. Li, L. Sun, *Angew. Chem. Int. Ed.* **2011**, *50* (51), 12276–12279.
- [29] (a) R. M. Kellett, T. G. Spiro, *Inorg. Chem.* **1985**, *24* (15), 2378–2382. (b) F. M. Toma, A. Sartorel, M. Iurlo, M. Carraro, S. Rapino, L. Hooper-Burkhardt, T. Da Ros, M. Marcaccio, G. Scorrano, F. Paolucci, M. Bonchio, M. Prato, *ChemSusChem* **2011**, *4* (10), 1447–1451.
- [30] Z. Chen, J. J. Concepcion, J. W. Jurss, T. J. Meyer, *J. Am. Chem. Soc.* **2009**, *131* (43), 15580–15581.
- [31] R. Matheu, L. Francàs, P. Chernev, M. Z. Ertem, V. Batista, M. Haumann, X. Sala, A. Llobet, *ACS Catal.* **2015**, *5* (6), 3422–3429.
- [32] K. L. Materna, B. Rudshiteyn, B. J. Brennan, M. H. Kane, A. J. Bloomfield, D. J. Huang, D. Y. Shopov, V. S. Batista, R. H. Crabtree, G. W. Brudvig, *ACS Catal.* **2016**, *6* (8), 5371–5377.
- [33] E. A. Mohamed, Z. N. Zahran, Y. Naruta, *J. Catal.* **2017**, *352*, 293–299.
- [34] J. J. Concepcion, J. W. Jurss, P. G. Hoertz, T. J. Meyer, *Angew. Chem. Int. Ed.* **2009**, *48* (50), 9473–9476.
- [35] J. Creus, R. Matheu, I. Peñafiel, D. Moonshiram, P. Blondeau, J. Benet-Buchholz, J. García-Antón, X. Sala, C. Godard, A. Llobet, *Angew. Chem. Int. Ed.* **2016**, *55* (49), 15382–15386.
- [36] (a) Abruña, H. D.; Denisevich, P.; Umaña, M.; Meyer, T. J.; Murray, R. W. *J. Am. Chem. Soc.* **1981**, *103* (1), 1–5. (b) P. Denisevich, H. D. Abruña, C. R. Leidner, T. J. Meyer, R. W. Murray, *Inorg. Chem.* **1982**, *21* (6), 2153–2161.

- [37] (a) J. Mola, E. Mas-Marza, X. Sala, I. Romero, M. Rodríguez, C. Viñas, T. Parella, A. Llobet, *Angew. Chem. Int. Ed.* **2008**, *47* (31), 5830-5832. (b) L. Wang, K. Fan, Q. Daniel, L. Duan, F. Li, B. Philippe, H. Rensmo, H. Chen, J. Sun, L. Sun, *Chem. Commun.* **2015**, *51* (37), 7883-7886.
- [38] (a) B. M. Klepser, B. M. Bartlett, *J. Am. Chem. Soc.* **2014**, *136* (5), 1694-1697. (b) B. Liu, J. Li, H. L. Wu, W. Q. Liu, X. Jiang, Z. J. Li, B. Chen, C. H. Tung, L. Z. Wu, *ACS Appl. Mater. Interfaces.* **2016**, *8* (28), 18577-18583. (c) Y. Wang, F. Li, X. Zhou, F. Yu, J. Du, L. Bai, L. Sun, *Angew. Chem. Int. Ed.* **2017**, *56* (24), 6911-6915.
- [39] (a) Ashford, D. L.; Lapidés, A. M.; Vannucci, A. K.; Hanson, K.; Torelli, D. A.; Harrison, D. P.; Templeton, J. L.; Meyer, T. J., *J. Am. Chem. Soc.* **2014**, *136* (18), 6578-6581. (b) Ashford, D. L.; Sherman, B. D.; Binstead, R. A.; Templeton, J. L.; Meyer, T. J., *Angew. Chem. Int. Ed.* **2015**, *54* (16), 4778-4781. (c) J. Li, Y. Jiang, Q. Zhang, X. Zhao, N. Li, H. Tong, X. Yang, L. Xia, *RSC Adv.* **2017**, *7* (7), 4102-4107.
- [40] (a) G. Férey, *Chem. Soc. Rev.* **2008**, *37* (1), 191-214. (b) H. Furukawa, K. E. Cordova, M. O’Keeffe, O. M. Yaghi, *Science* **2013**, *341*, 1230444.
- [41] (a) K. Meyer, M. Ranocchiari, J. A. van Bokhoven, *Energy Environ. Sci.* **2015**, *8* (7), 1923-1937. (b) Q. Shao, J. Yang, X. Huang, *Chem. Eur. J.* **2018**, *24* (57), 15143-15155. (c) D. Li, H. Xu, L. Jiao, H. Jiang, *EnergyChem* **2019**, *1* (1), 100005.
- [42] (a) C. Wang, Z. Xie, K. E. deKrafft, W. Lin, *J. Am. Chem. Soc.* **2011**, *133* (34), 13445-13454. (b) C. Wang, J. Wang, W. Li, *J. Am. Chem. Soc.* **2012**, *134* (48), 19895-19908. (c) S. Lin, Y. Pineda-Galvan, W. A. Maza, C. C. Epley, J. Zhu, M. C. Kessinger, Y. Pushkar, A. J. Morris, *ChemSusChem* **2017**, *10* (3), 514-522.
- [43] (a) B. Nepal, S. Das, *Angew. Chem. Int. Ed.* **2013**, *52* (28), 7224-7227. (b) G. Paille, M. Gomez-Mingot, C. Roch-Marchal, B. Lassalle-Kaiser, P. Mialane, M. Fontecave, C. Mellot-Draznieks, A. Dolbecq, *J. Am. Chem. Soc.* **2018**, *140* (10), 3613-3618. (c) A. Bhunia, B. A. Johnson, J. Czapla-Masztafiak, J. Sá, S. Ott, *Chem. Commun.* **2018**, *54* (56), 7770-7773.

Chapter 1

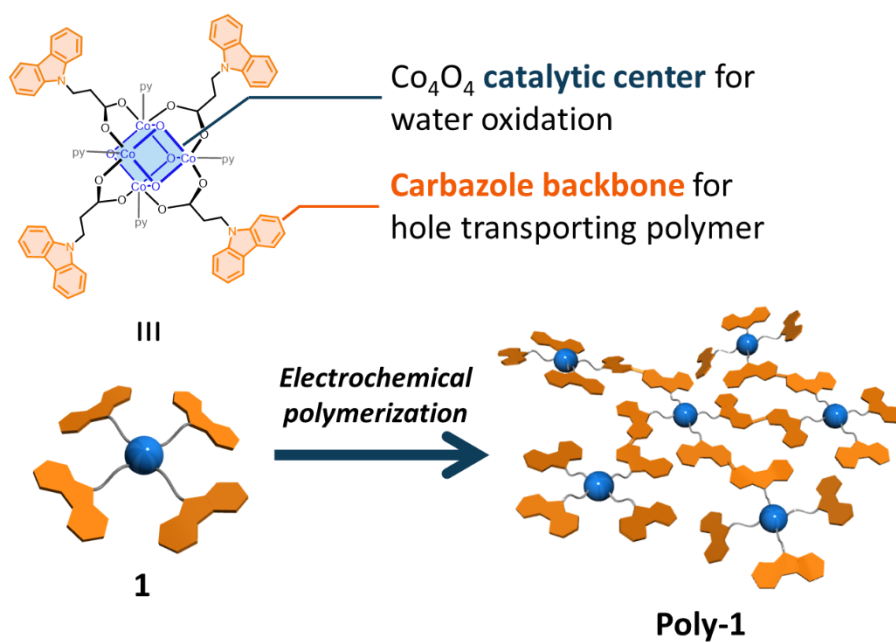
Electrochemical Polymerization Provides a Function-Integrated System for Water Oxidation

Introduction

Demand for a sustainable society and clean energy production has increased in recent years.[1] Four-electron oxidation of water ($2\text{H}_2\text{O} \rightarrow \text{O}_2 + 4\text{H}^+ + 4\text{e}^-$) is an important reaction for supplying the protons and electrons required to generate reduced products (i.e., chemical energy) from abundant resources in a clean manner.[2] In nature, the reaction is catalyzed by a metal-complex-based catalyst, the oxygen-evolving complex (OEC), embedded in photosystem II.[3,4] The OEC is known as a highly active and robust catalyst that can drive the reaction under mild condition. In the OEC, a manganese-based multinuclear cluster, which serves as the catalytic center, is surrounded by several amino acid residues, and these residues play an important role in transferring electrons/holes to the catalytic center.[3,4] This fact indicates that the presence of hole transporters close to the metal-complex based catalytic center is a key to efficiently promoting water oxidation reactions. Thus far, there have been many reports on the molecule-based catalytic system for water oxidation. However, the works mainly focus solely on the construction of catalytic centers[2a-g,5,6] or the immobilization of catalytic centers on electrode surfaces.[2h, 7] Thus, the literature contains no report on the development of catalytic systems that have a catalytic center surrounded by hole transporting units.

In this chapter, I disclose a novel approach for developing an artificial catalytic system for water oxidation. Inspired by the natural water oxidation system, I hypothesized that the integration of catalytic centers and hole transporters into one material could be a promising strategy. Based on this strategy, a polymer-based catalytic system was constructed by assembling catalytic center and hole transporter units. The several spectroscopic measurements clearly demonstrated that these functional units are successfully incorporated in the assembled system (**Poly-1**). It was also revealed that

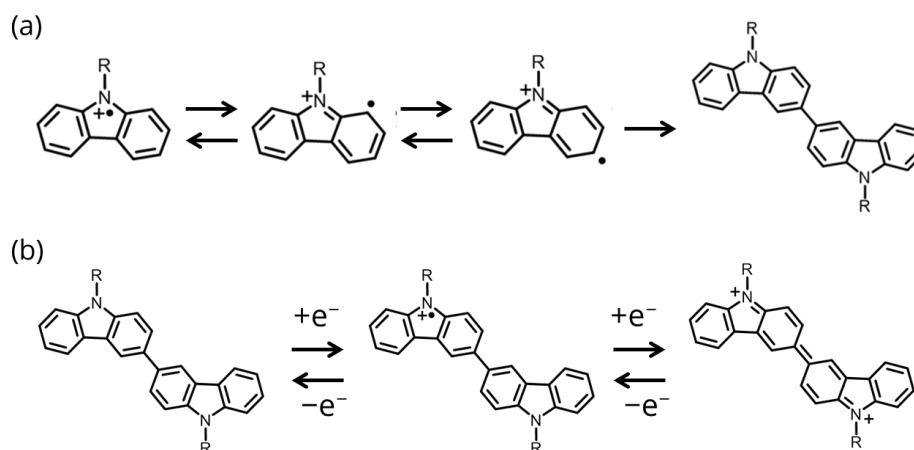
Poly-1 exhibited high hole transporting ability. Moreover, **Poly-1** can promote electrocatalytic water oxidation with a high faradaic efficiency (>90%) and a low overpotential ($\eta = 413$ mV) in aqueous media. This performance of **Poly-1** is of the highest class compared to the relevant systems.



Scheme 1. (Top) Structure of the metal-complex-based precursor (**1**) developed in this study. (Bottom) Schematic illustration of the preparation of function-integrated catalytic system for water oxidation via the electrochemical polymerization of **1**.

Results and discussions

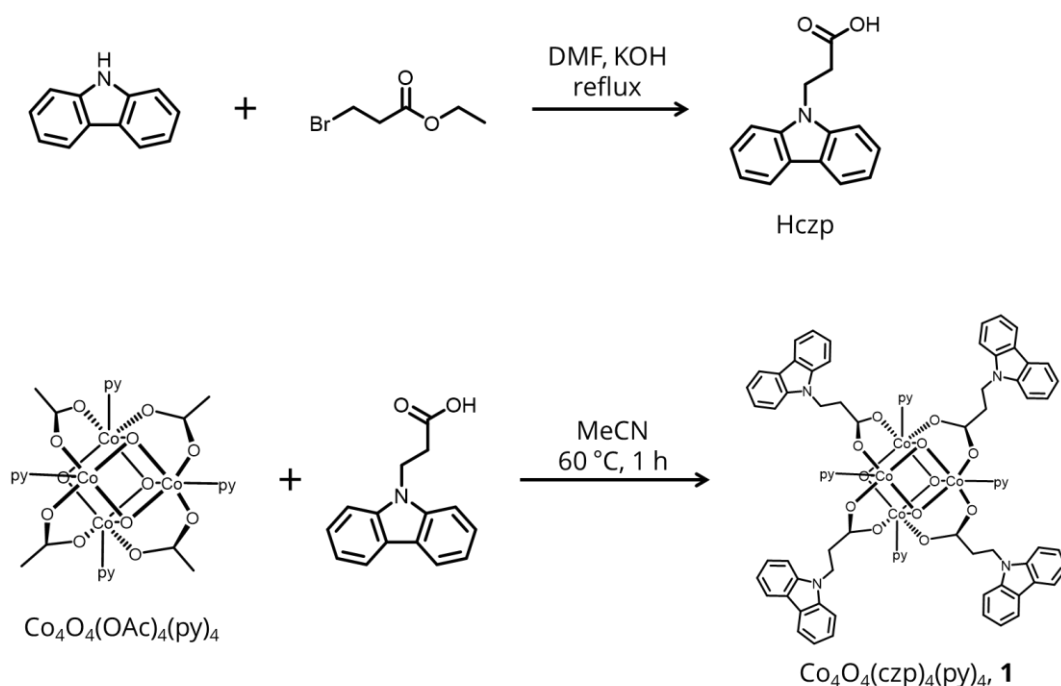
The key to my success is the utilization of a newly designed metal-complex-based precursor, **1**, shown in Scheme 1. **1** is comprised of two distinct functional units: a tetranuclear cobalt complex and carbazole moieties (Scheme 1, top). The tetranuclear cobalt complex has a cubane-shaped structure, which is also observed in the OEC, and it serves as an artificial catalyst for water oxidation.[8] Carbazole derivatives are known to dimerize under oxidative conditions (Scheme 2a).[9] In addition, the formed biscarbazole exhibits hole-transfer ability (Scheme 2b),[10] which should favor the oxidative catalytic reaction. Therefore, materials with catalytic centers and hole transporters should be accessible (**Poly-1**, Scheme 1, bottom) by the electrochemical polymerization of **1**.



Scheme 2. Oxidative dimerization of carbazole derivatives to form biscarbazole derivatives. (b) Redox properties of biscarbazole derivatives.

Synthesis of complex **1**

The metal-complex-based precursor, **1**, was synthesized by following Scheme 3. Initially, carbazole-9-propionic acid (Hczp) was synthesized by modifying a previously reported procedure[11] (yield: 57%) and was characterized by ^1H NMR spectroscopy. Subsequently, Hczp was reacted with $\text{Co}_4\text{O}_4(\text{OAc})_4(\text{py})_4$ (^-OAc = acetate anion, py = pyridine)[12] in MeCN at 60 °C for 1 h. The reaction was monitored by thin-layer chromatography and quenched after the consumption of $\text{Co}_4\text{O}_4(\text{OAc})_4(\text{py})_4$. Notably, the ligand substitution reaction at 90 °C led to the decomposition of the starting materials, and thus, the reaction was conducted at a moderate temperature (60 °C). The crude product was further purified by silica-gel column chromatography, and the desired complex **1** was obtained in 66% yield. The complex was characterized by ^1H NMR spectroscopy, single-crystal X-ray structural analysis and elemental analysis.



Scheme 3. Synthesis of Hczp and complex **1**.

Single crystal X-ray structure analysis

Single crystals of **1** suitable for X-ray diffraction measurements were obtained by vapor diffusion of Et₂O into a CH₂Cl₂ solution of **1** at room temperature. An ORTEP diagram of **1** is shown in Figure 1. **1** crystallized in $P\bar{1}$, and the asymmetric unit contains one complex and 2.5 CH₂Cl₂ molecules as solvents of crystallization. In **1**, all the acetate ligands were exchanged for czp⁻ ligands. The average bond distances between the Co ions and the oxygen atoms in the μ -oxo bridging ligand (Co-O_{oxo}) and between the Co ions and the oxygen atoms of czp⁻ ligands (Co-O_{cpz}) are 1.855(3)-1.867(2) and 1.947(3)-1.995(3) Å, respectively (Table 2). These values are comparable to those reported previously.[13]

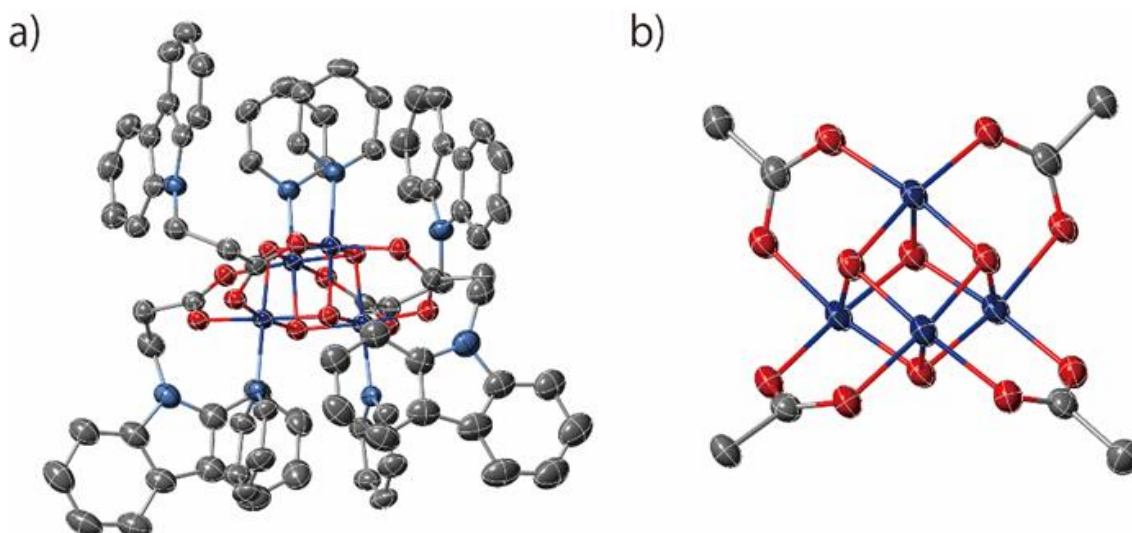


Figure 1. ORTEP drawings of (a) **1** and (b) the core structure of **1**. Solvent molecules and hydrogen atoms are omitted for clarity. Thermal ellipsoids are shown at the 50% probability level. Color chart: purple: Co, grey: C, cyan: N, red: O.

Table 1. Crystallographic parameters of complex 1.

Formula	$C_{80}H_{68}Co_4N_8O_{12} \cdot 2.5CH_2Cl_2$
Fw	1781.45
Crystal color, habit	Black, needle
Crystal size (mm ³)	0.482 × 0.049 × 0.046
Crystal System	triclinic
Space Group	$P\bar{1}$
a (Å)	14.3729(3)
b (Å)	17.2850(4)
c (Å)	17.9135(3)
α (°)	95.760(2)
β (°)	108.817(2)
γ (°)	110.650(2)
V (Å ³)	3824.95(15)
Z	2
$F(000)$	1826
T (K)	123(2)
R_1	0.0646
wR_2	0.1888
GooF	1.033

Table 2. Selected bond lengths in **1**.

Co-O _{oxo} (average)	1.861	Co-O _{czp} (average)	1.968
Co1-O1	1.864(2)	Co1-O5	1.968(3)
Co1-O2	1.855(3)	Co1-O7	1.991(3)
Co1-O3	1.865(2)	Co2-O6	1.964(3)
Co2-O1	1.860(3)	Co2-O12	1.947(2)
Co2-O2	1.862(3)	Co3-O9	1.967(3)
Co2-O4	1.865(3)	Co3-O11	1.995(3)
Co3-O1	1.859(2)	Co4-O8	1.947(2)
Co3-O3	1.867(2)	Co4-O10	1.964(3)
Co3-O4	1.858(2)		
Co4-O2	1.864(3)		
Co4-O3	1.855(3)		
Co4-O4	1.862(3)		

Electrochemistry

The electrochemical behaviors of **1** were investigated by cyclic voltammetry (CV) in an organic medium (0.1 M tetra-*n*-butyl ammonium hexafluorophosphate (TBAPF₆) in CH₂Cl₂), and the results are shown in Figure 2. In the first cycle (Figure 2a), the oxidation peak was observed at approximately 0.278 V (vs. Fc/Fc⁺), and the peak was assigned to the oxidation of the cobalt center, Co^{III}₃Co^{IV}/Co^{III}₄.^[13] Upon further sweeping of the potential to the positive region, a large peak attributed to the oxidation of the carbazole moieties was observed at approximately 0.7 V. In the reverse scan, two new redox waves were observed at 0.323 and 0.601 V. These redox waves were due to the formation of a biscarbazole structure.^[10] In the second and subsequent cycles (Figure 2b), the intensity of the current attributed to the redox couple of biscarbazole ($E_{1/2} = 0.432$ and 0.755 V) was increased, indicating the formation of further biscarbazole moieties upon electrochemical oxidation. Note that the similar trend was also observed when an ITO was used as a working electrode (Figure 3). These results indicate that **1** is electrochemically polymerized via the dimerization of *czp*⁻ ligands.

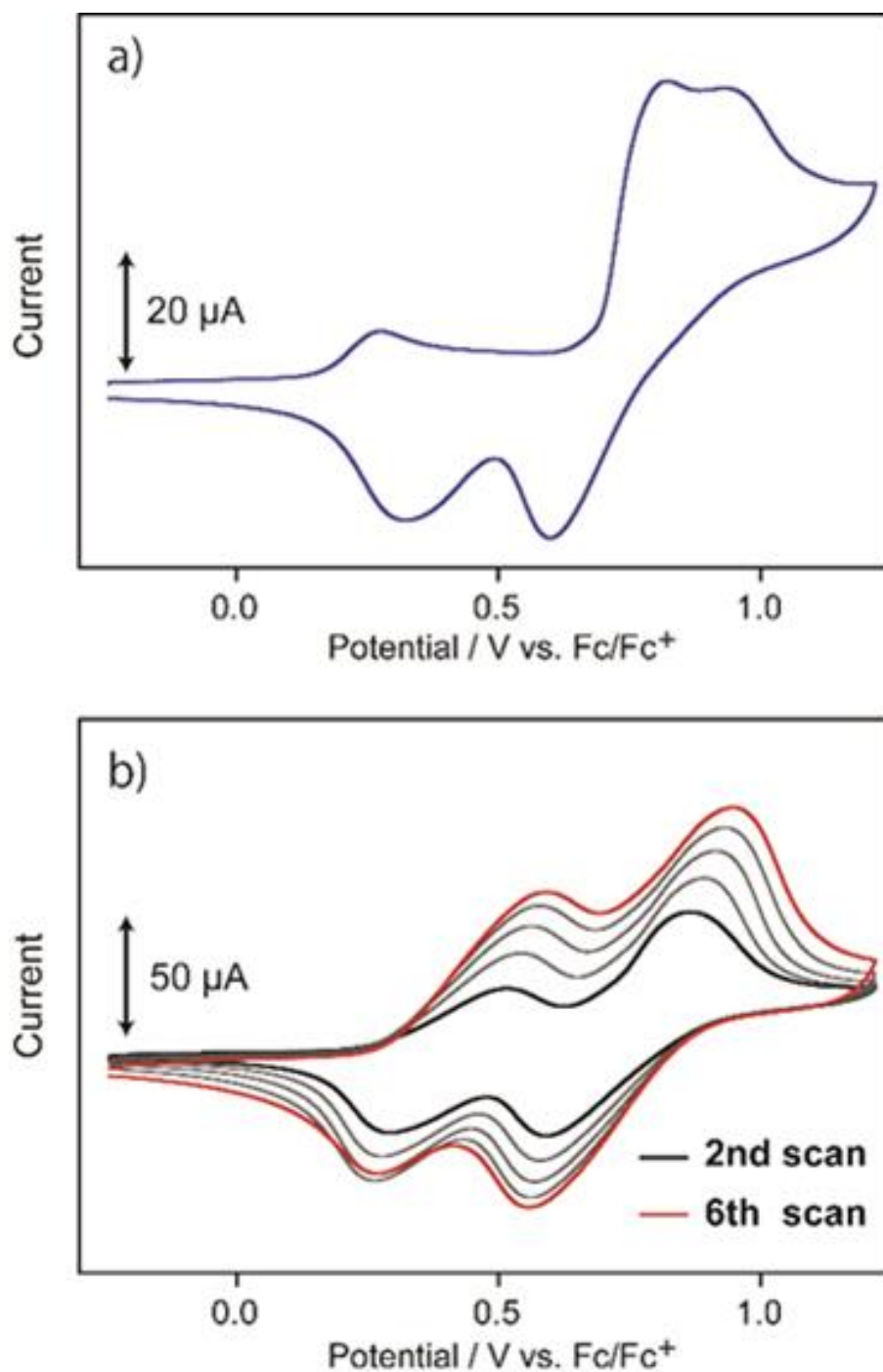


Figure 2. Cyclic voltammograms of a 0.19 mM solution of **1**. (a) 1st scan and (b) 2nd to 6th scans. Measurements were performed in a CH_2Cl_2 solution containing 0.1 M TBAPF_6 under Ar at a scan rate of 100 mV s^{-1} . Working electrode, glassy carbon; counter electrode, Pt wire; reference electrode, Ag/Ag^+ . CV scans were initiated from the open-circuit potential.

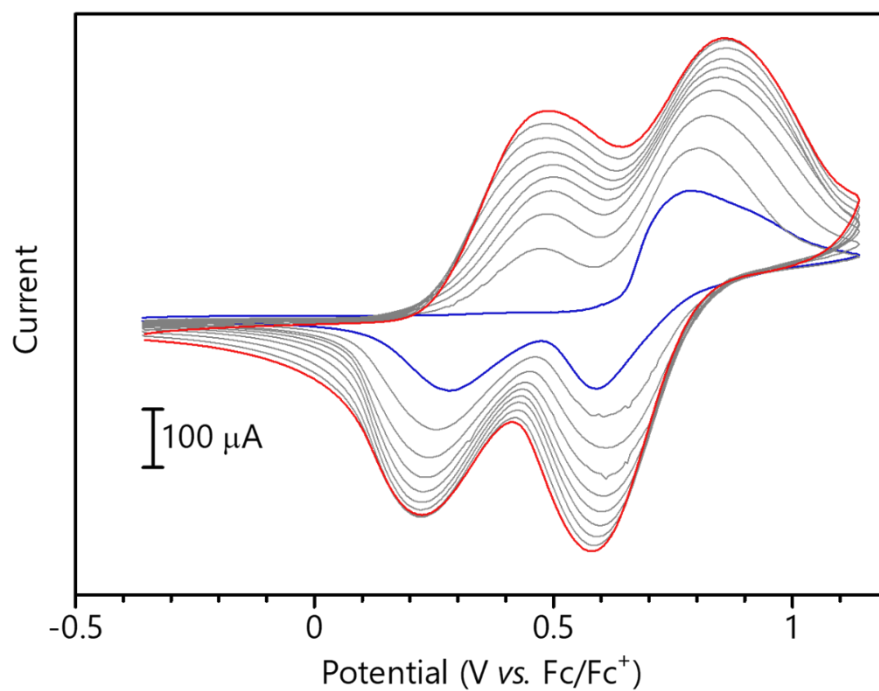


Figure 3. Cyclic voltammograms of a 0.19 mM solution of **1**. Measurements were performed in a CH₂Cl₂ solution containing 0.1 M TBAPF₆ under Ar at a scan rate of 100 mV s⁻¹. Working electrode, ITO plate; counter electrode, Pt wire; reference electrode, Ag/Ag⁺. CV scans were initiated from the open-circuit potential.

Characterization of Poly-1

To elucidate the polymerization behavior of **1**, electrochemical measurements were also conducted using a transparent electrode (ITO plate) as the working electrode. In this experiment, a constant potential (1.3 V vs. Ag/Ag⁺) was applied to the ITO electrode in a 0.1 M TBAPF₆-CH₂Cl₂ solution containing 0.19 mM **1** for 10 – 90 s, and after electrolysis, the electrodes were analyzed by UV-vis absorption spectroscopy. The UV-vis absorption spectra of the electrodes are shown in Figures 4. A band center at approximately 420 nm and a broad band at approximately 800 nm were observed in all cases, and the intensities of the bands gradually increased as the electrolysis time increased. The band at 800 nm can mainly be attributed to the intervalence charge transfer (IVCT) transitions of mixed-valent biscarbazole units or charge-resonance bands in the case of Robin-Day class III systems.[10,14] These results clearly demonstrate that the carbazole moieties of **1** were dimerized upon oxidation to afford a polymer with a biscarbazole backbone.

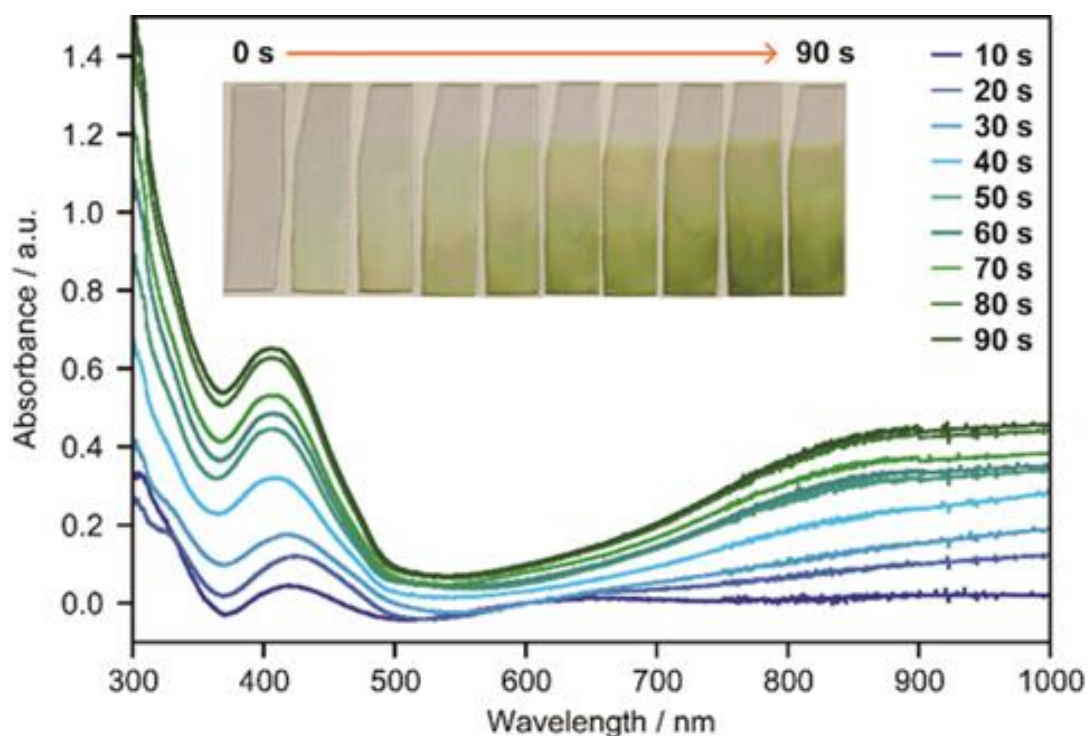


Figure 4. UV-vis absorption spectra of the ITO electrodes electrolyzed at 1.3 V vs. Ag/Ag⁺ for 10-90 s using a 0.1 M TBAPF₆-CH₂Cl₂ solution containing 0.19 mM of **1**. (Inset) Photographs of the ITO electrodes after the electrolysis.

To further verify the structure of the polymer, the infrared spectra of **1** before and after polymerization were measured (Figure 5). Both spectra showed several common vibration peaks, COO⁻ asymmetric vibration (1550 cm⁻¹), pyridine ring vibration (760 cm⁻¹) and Co-O_{oxo} stretching vibration (630 cm⁻¹).^[13] The data strongly indicates that the cobalt-cubane structure is preserved in the polymer.

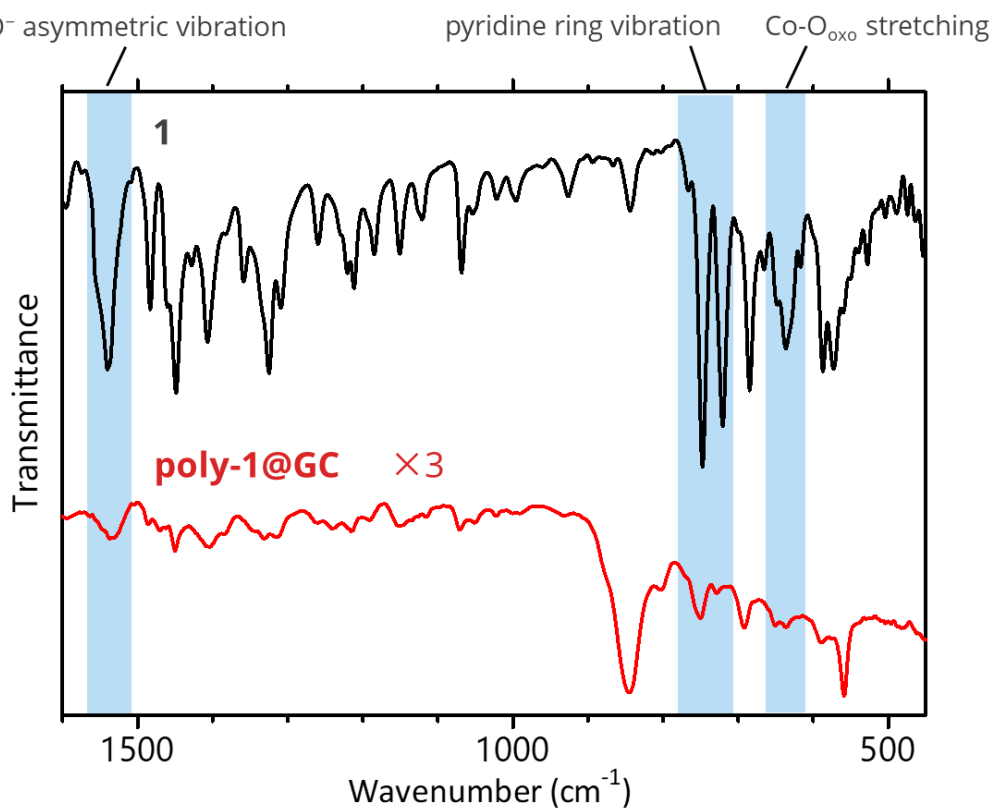


Figure 5. FT-IR spectra of **1** (black line) and **Poly-1@GC** (red line).

I also analyzed the obtained polymer by scanning electron microscopy (SEM). The SEM image of the polymer shows a flat surface structure, indicating the formation of a homogeneous film on the electrode (Figure 6, left). It should be noted that the morphology of the film is completely distinct from that of oxidized Co phosphate inorganic materials (Figure 9, top), which indicates that the oxidized Co phosphate inorganic materials are not formed during the polymerization of **1**. The energy dispersive X-ray (EDX) elemental map of the film showed a uniform distribution of cobalt, which also suggests the homogeneity of the polymer (Figure 6, right). In the EDX spectrum (Figure 7), peaks attributable to fluorine and phosphorus were also detected, suggesting that PF_6^- was doped into the polymer. The control experiments using the oxidized Co phosphate inorganic materials revealed stronger peak intensities of Co and P (Figure 9, bottom) than **Poly-1** (Figure 7), supporting that the film has different composition from oxidized Co phosphate inorganic materials. These observations indicate that **1** is electrochemically polymerized to uniform polymer, **Poly-1**, which has both biscarbazole and cobalt cubane moieties.

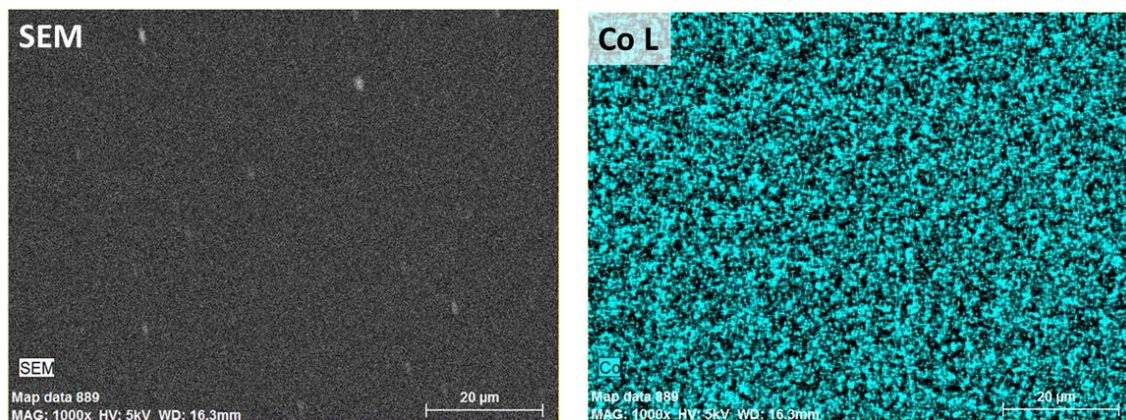


Figure 6. A SEM image (left) and an EDX elemental map (right) of **Poly-1** fabricated on an ITO electrode.

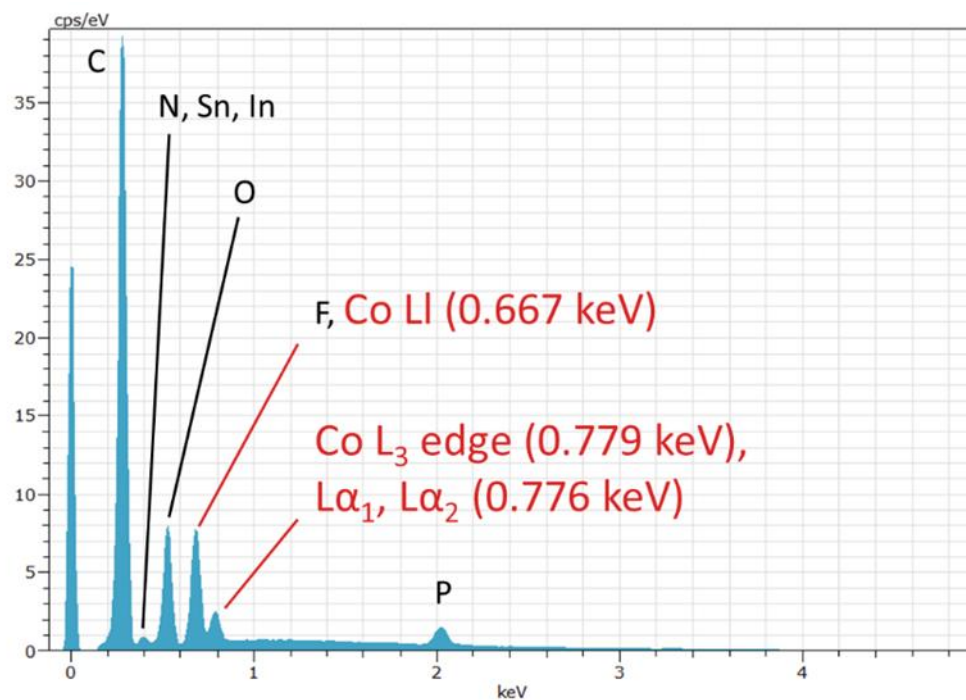


Figure 7. An EDX spectrum of **Poly-1** fabricated on an ITO electrode.

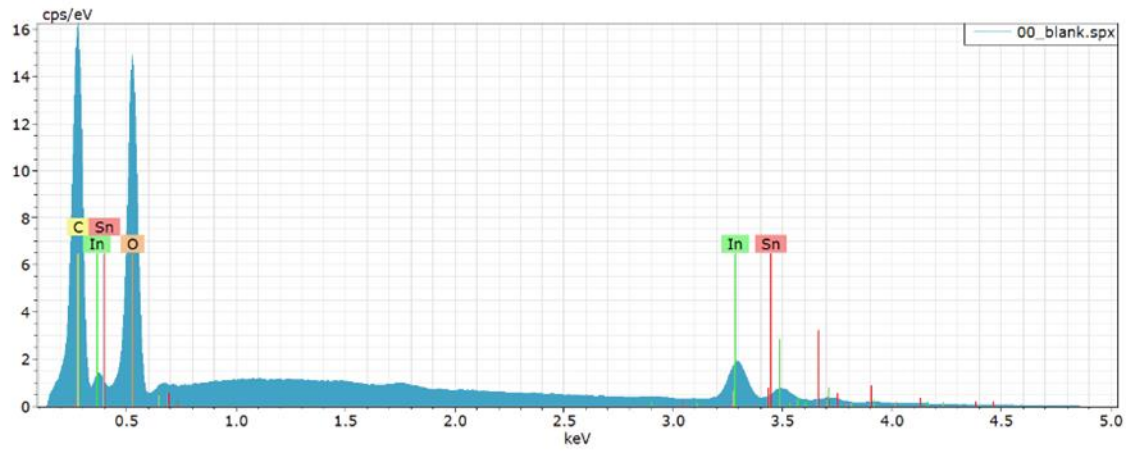
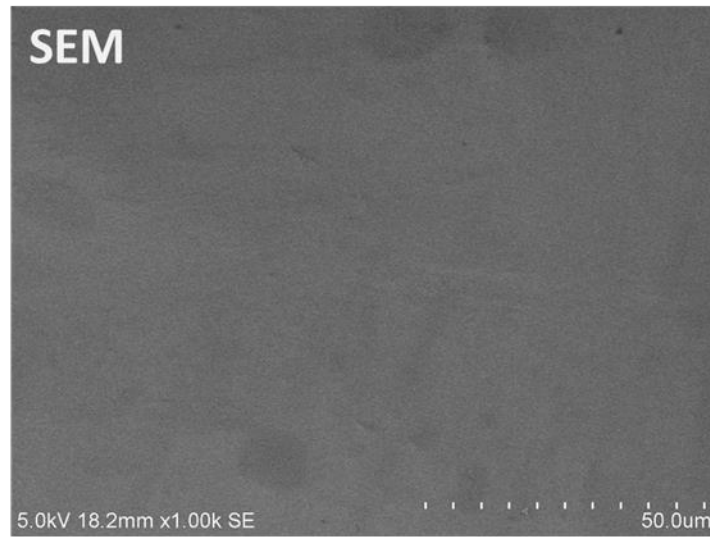


Figure 8. A SEM image (top) and an EDX spectrum (bottom) of a bare ITO electrode.

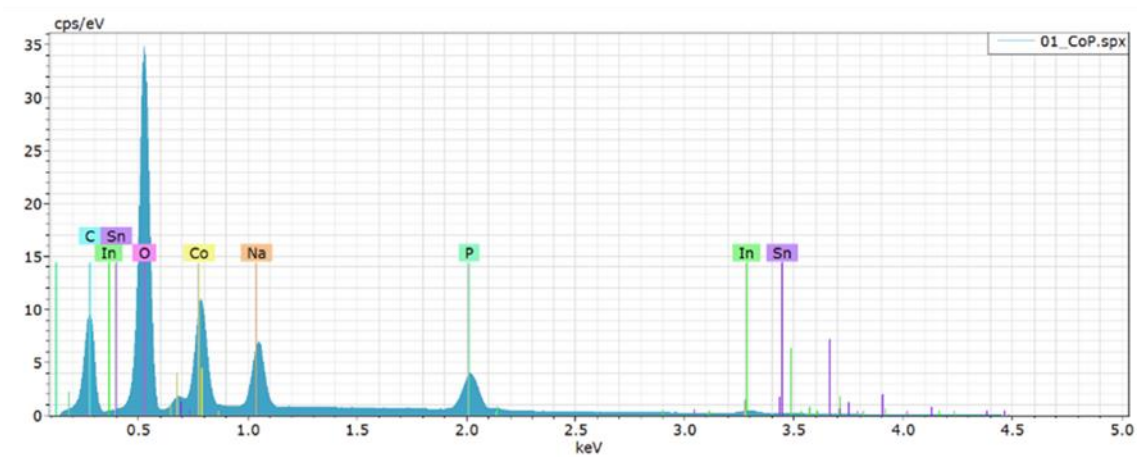
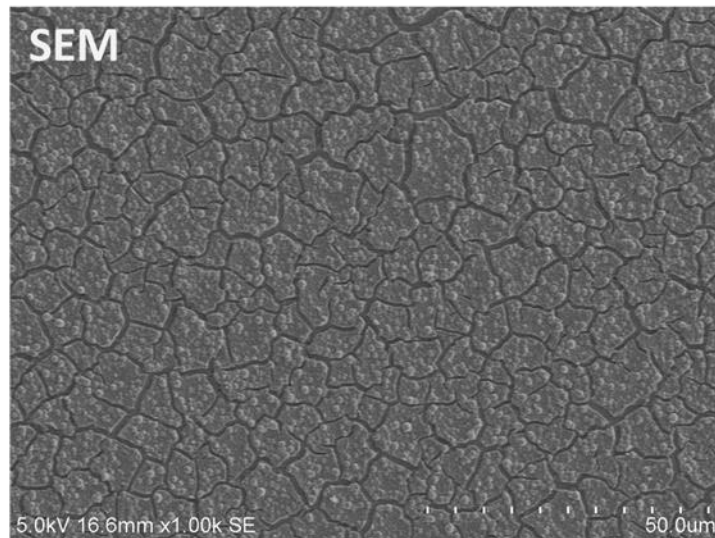


Figure 9. A SEM image (top) and an EDX spectrum (bottom) of oxidized cobalt phosphate inorganic materials on an ITO electrode.

Electrochemical impedance spectroscopy

To clarify charge transfer ability of **Poly-1**, electrochemical impedance spectra (EIS) were measured. EIS were measured for a bare glassy carbon (GC) electrode, the GC electrode modified with the cobalt cubane complex without biscarbazole moieties, $\text{Co}_4\text{O}_4(\text{PhCOO})_4(\text{py})_4$ ($\text{Co}_4\text{O}_4(\text{PhCOO})_4(\text{py})_4@\text{GC}$, PhCOOH =benzoic acid), and the GC electrode modified with **Poly-1** (**Poly-1**@GC). Figure 10 shows the EIS measured at 1.30 V vs. Ag/AgCl of the bias potential. The diameters of semicircles in Nyquist plots were decreased in the order of a bare GC, $\text{Co}_4\text{O}_4(\text{PhCOO})_4(\text{py})_4@\text{GC}$ and **Poly-1**@GC. Fitted charge transfer resistance (R_{CT}) values with the equivalent circuit (Figure 10 inset) of a bare GC, $\text{Co}_4\text{O}_4(\text{PhCOO})_4(\text{py})_4@\text{GC}$, and **Poly-1**@GC were 4606, 1706 and 679 Ω respectively (Table 3). R_{CT} of **Poly-1**@GC was reduced to 15% of bare GC and 40% of $\text{Co}_4\text{O}_4(\text{PhCOO})_4(\text{py})_4@\text{GC}$. These results clearly demonstrate that charge transfer ability is largely enhanced due to the biscarbazole moieties embedded in **Poly-1**.

Table 3. Fitting results of electrochemical impedance spectrometry for different working electrodes. R_{CT} : charge transfer resistance, R_{ele} : electrolyte resistance, Q : constant phase element (CPE) value, α : CPE index.

	GC only	$\text{Co}_4\text{O}_4(\text{PhCOO})_4(\text{py})_4@\text{GC}$	Poly-1 @GC
R_{CT} (Ω)	4606	1776	679
R_{ele} (Ω)	68.57	29.44	55.42
Q (μF)	40.92	213.9	270.1
α	0.894	0.774	0.814

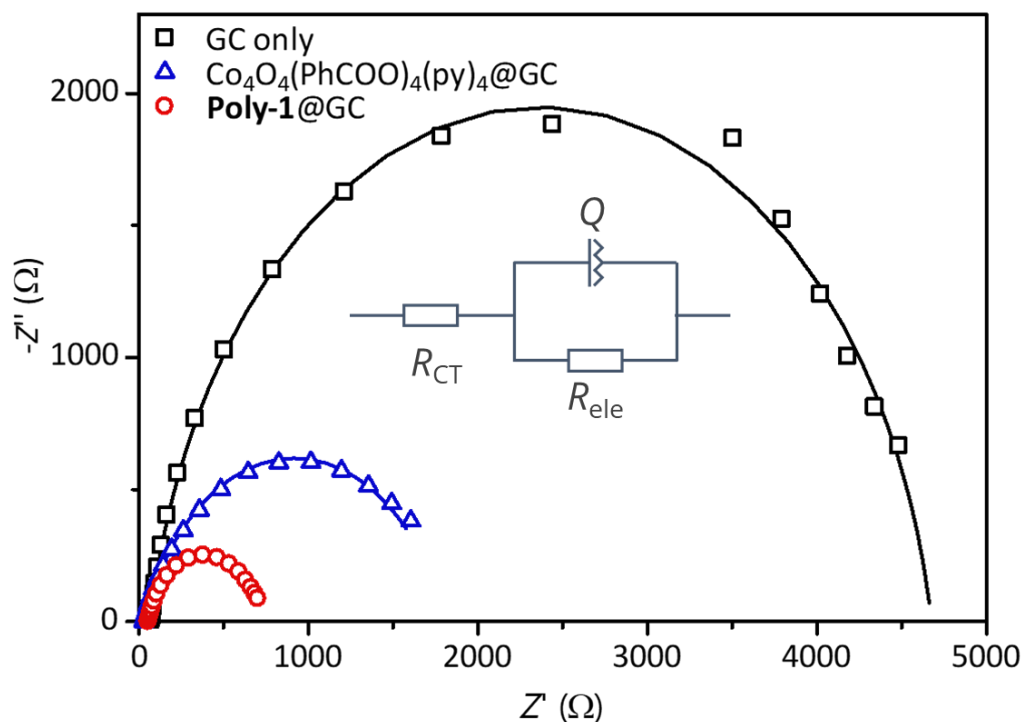


Figure 10. Nyquist plots of a bare GC (black), $\text{Co}_4\text{O}_4(\text{PhCOO})_4(\text{py})_4@\text{GC}$ (blue) and **Poly-1@GC** (red). Measurements were performed in 0.2 M phosphate buffer (pH = 7.06) under an argon atmosphere. (Inset) the equivalent circuit for fitting data. Applied potential: 1.30 V vs. Ag/AgCl, measurement range: 0.1 Hz - 100 kHz. 20 nmol of $\text{Co}_4\text{O}_4(\text{PhCOO})_4(\text{py})_4$ was mounted from a CH_2Cl_2 solution of $\text{Co}_4\text{O}_4(\text{PhCOO})_4(\text{py})_4$ by drop-cast method to prepare $\text{Co}_4\text{O}_4(\text{PhCOO})_4(\text{py})_4@\text{GC}$.

Catalytic activity

Finally, the electrocatalytic activity of **Poly-1** for water oxidation was evaluated. To investigate the catalytic activity, **Poly-1** was immobilized on a glassy carbon electrode. Figure 11 shows the cyclic voltammograms of **Poly-1@GC** in a phosphate buffer solution (pH = 7.06). A large irreversible current was clearly observed at approximately 1.0 V (vs. Ag/AgCl), which confirms the water oxidation ability of **Poly-1**. The overpotential (η) was estimated to be 413 mV.

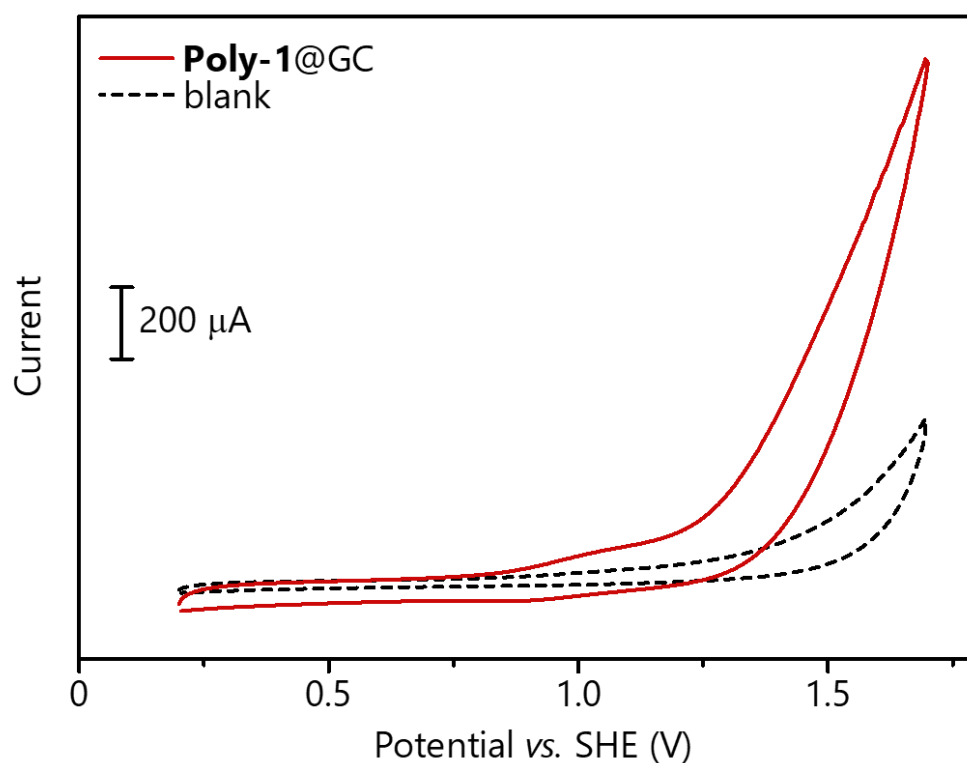


Figure 11. Cyclic voltammograms of a **Poly-1@GC** (red line) and a bare GC (black dashed line) electrode in phosphate buffer solutions (pH = 7.06). Measurements were performed under Ar at a scan rate of 100 mV s^{-1} .

To further verify the water oxidation performance of **Poly-1**, controlled potential electrolysis of **Poly-1** was then performed. After 1 h of electrolysis of **Poly-1@GC** at 1.30 V (vs. Ag/AgCl), 1.55 C of charge was passed, and 3.68 μmol of O_2 as the major product was detected by gas chromatography (Figure 12 and Table 4). The maximum faradaic efficiency of the reaction based on the $4e^-$ process was estimated to be 91.5%.

Table 4. The amounts of evolved O_2 , charge and Faradaic efficiencies over 1 h of controlled potential electrolysis of **Poly-1@GC**.

Potential (V vs. Ag/AgCl)	O_2 (μmol)	Charge (C)	Faradaic efficiency (%)
1.30	3.68	1.55	91.5
1.33	4.11	2.03	78.1
1.35	6.12	2.70	87.5

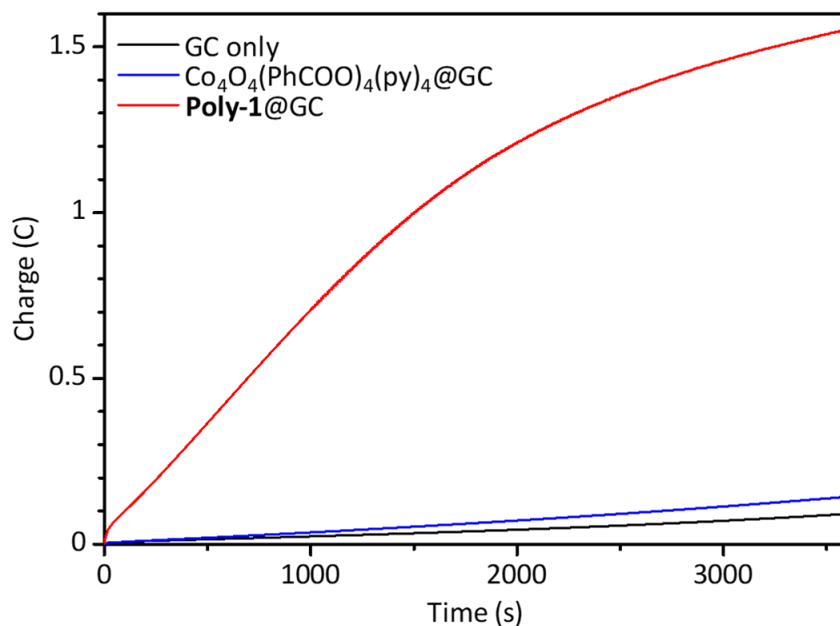


Figure 12. Controlled potential electrolysis data of **Poly-1@GC** (red line), $\text{Co}_4\text{O}_4(\text{PhCOO})_4(\text{py})_4@\text{GC}$ (blue line) and a bare GC (black line) in phosphate buffer solutions (pH = 7.06) under an argon atmosphere. Applied potential: 1.30 V vs. Ag/AgCl.

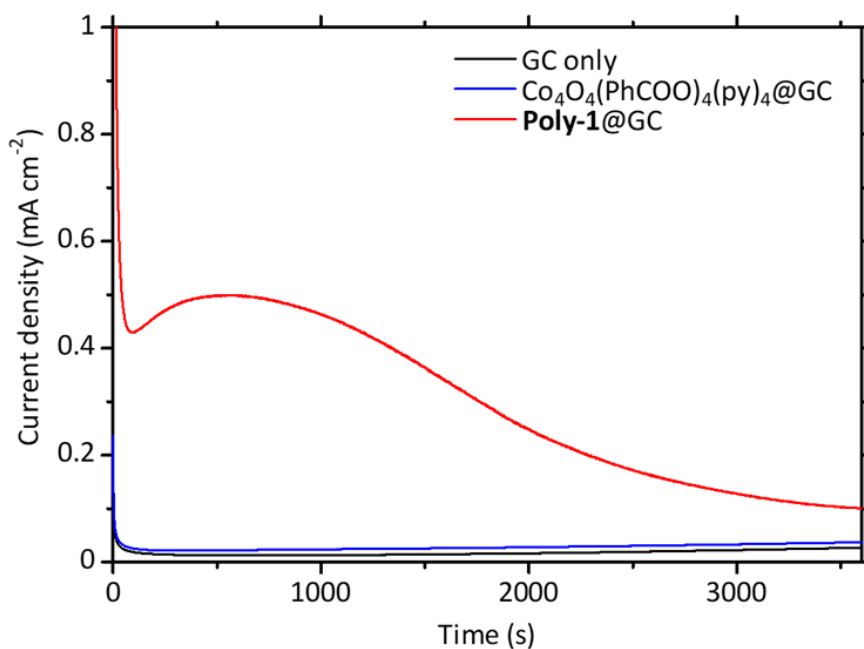


Figure 13. *I-t* curves of **Poly-1@GC** (red line), $\text{Co}_4\text{O}_4(\text{PhCOO})_4(\text{py})_4@\text{GC}$ (blue line), and a bare GC electrode (black line) during 1 h of electrolysis at 1.30 V vs. Ag/AgCl.

The isotope labelling experiments using ^{18}O -labelled water, H_2^{18}O (97%) were also performed. After the 30 min of the electrolysis at 1.30 V (vs. Ag/AgCl), gaseous phase was analyzed by GC-MS. As a result, the formation of $^{18}\text{O}_2$ as a major product was confirmed (Figure 14). Moreover, the ratio between $^{18}\text{O}_2$ and $^{18}\text{O}^{16}\text{O}$ was in good agreement with the theoretical values (exp. $^{18}\text{O}_2 : ^{18}\text{O}^{16}\text{O} = 100 : 7.8$, theor. $^{18}\text{O}_2 : ^{18}\text{O}^{16}\text{O} = 100 : 6.1$). These results clearly demonstrate that the origin of oxygen atoms in evolved dioxygen is water in the catalysis mediated by **Poly-1**.

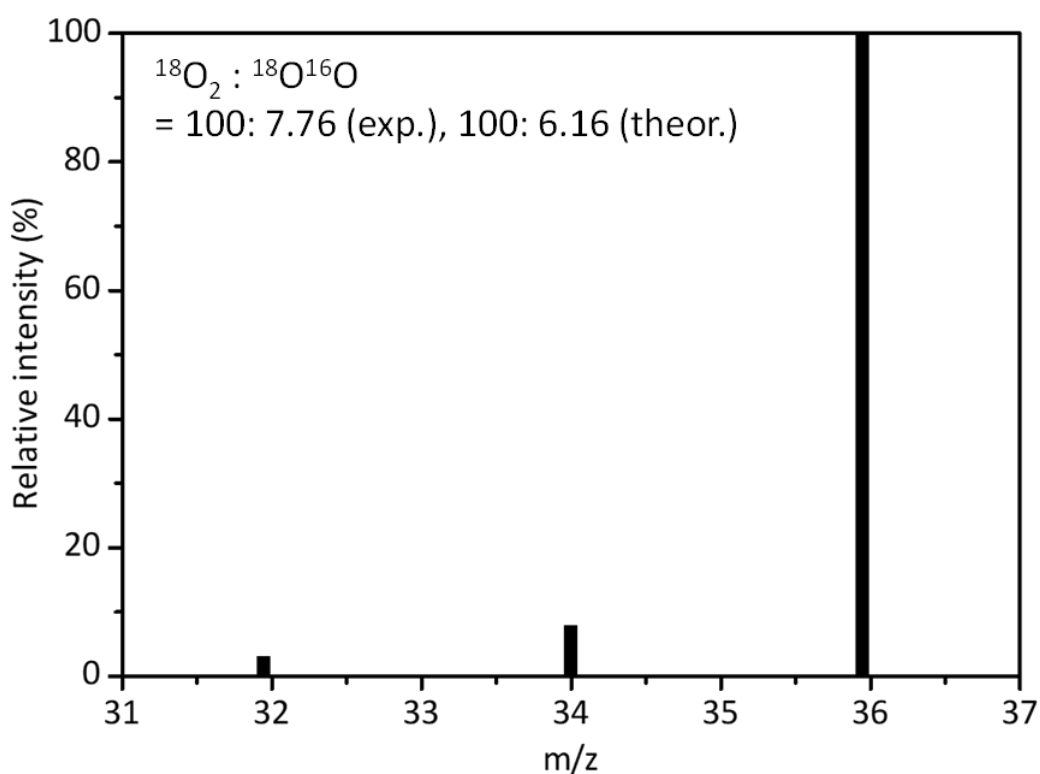


Figure 14. A mass spectrum of O_2 generated after the electrolysis of **Poly-1**@GC in a phosphate buffer prepared by using H_2^{18}O (97%). The data was corrected by the subtraction of background and air leakage calculated from intensity of $\text{N}_2^{16}\text{O}_2$.

To investigate the stability of **Poly-1**, a long-term electrolysis was carried out. During 6 h of electrolysis at 1.30 V (vs. Ag/AgCl), the current passed continuously (Figure 15), and the formation of dioxygen with 88.6% of Faradaic efficiency was confirmed (Table 5), which suggests that **Poly-1** was stable under the catalytic condition. These results clearly demonstrate that **Poly-1** can promote electrocatalytic water oxidation. It should be noted that the catalytic activity is almost suppressed under identical experimental condition when the electrode modified with the complex without biscarbazole moieties, $\text{Co}_4\text{O}_4(\text{PhCOO})_4(\text{py})_4 @\text{GC}$, was used (Figure 12, blue line). The result together with the results of the EIS measurements clearly demonstrate that the existence of biscarbazole moieties as hole transporters is essential to achieve the efficient catalysis. In other words, the importance of the integration of hole transporting units close to the catalytic center is successfully confirmed. In addition, the catalytic performance of **Poly-1** was of the highest class among the reported cobalt-complex-based catalytic system for water oxidation in terms of overpotentials and faradaic efficiencies (for the details of the comparisons with other relevant catalysts, see Table 6).[5g,15-23]

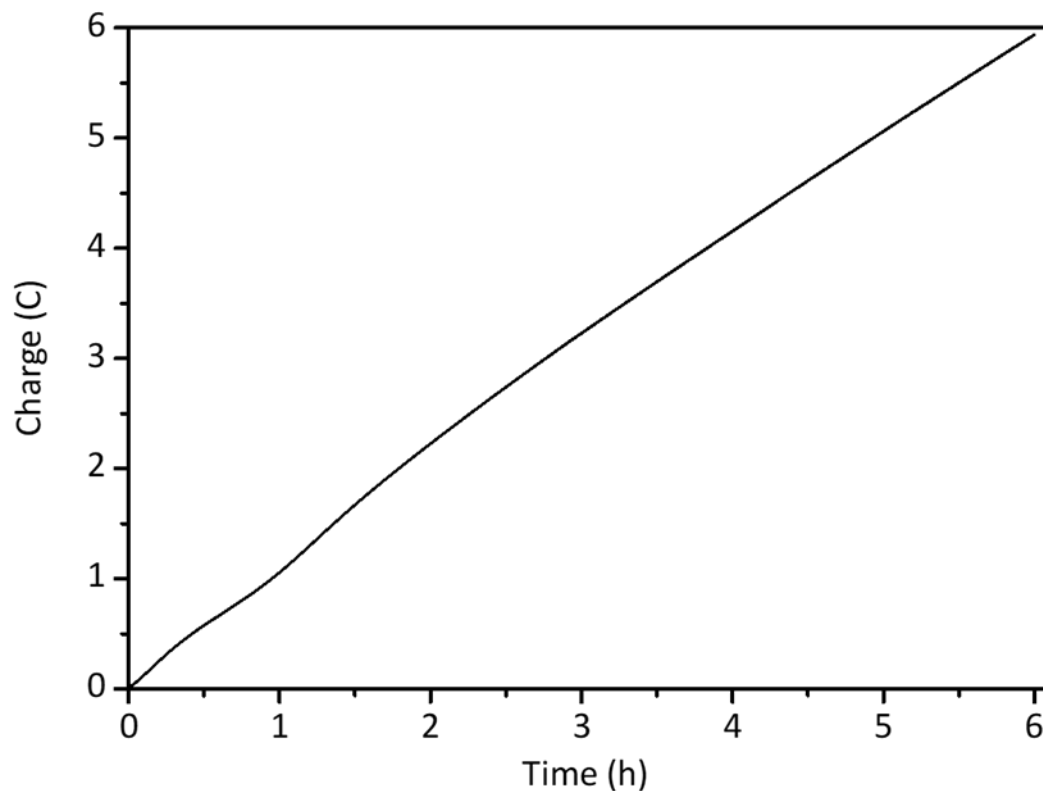


Figure 15. Controlled potential electrolysis data of **Poly-1@GC** in a phosphate buffer solution (pH = 7.06) under an argon atmosphere for 6 h. Applied potential: 1.30 V vs. Ag/AgCl.

Table 5. The amounts of evolved O₂, charge and Faradaic efficiencies over 1 h and 6 h of controlled potential electrolysis of **Poly-1@GC**. The results of the CPE experiments for 1 h is identical to those shown in Table 4.

Potential (V vs. Ag/AgCl)	Duration (h)	O ₂ (μmol)	Charge (C)	Faradaic efficiency (%)
1.30	1	3.68	1.55	91.5
1.30	6	13.6	5.94	88.6

Table 6. Comparison of catalytic activity of the relevant cobalt-complex-based catalysts for water oxidation and **Poly-1**. Molecular structures of **2-11** are shown in Figure 15.

Catalyst	Overpotential (η , mV)	Faradaic Efficiency (%)	Experimental conditions	Ref.
Poly-1@GC	413	91.5	pH 7.02, phosphate buffer, 1.3 V vs. Ag/AgCl	This work
Co ^{II} -TDMImP	~380	85-90	pH 7, 0.2 M Na-Pi buffer, 1.3 V vs. Ag/AgCl	5g
[Co(tpy)] ₂ (μ -bpp) (μ -1,2-O ₂) ³⁺	~800	77	pH 2.1, 0.1 M phosphate buffer, 2.0 V vs. NHE	15
[Co ^{II} (Py ₅ (OH ₂)) (ClO ₄) ₂]	~500	-	pH 9.2, 0.1 M phosphate buffer	16
[Co ^{III} -bTAML] ⁻	-	62	pH 9.2, 0.1 M phosphate buffer, 1.5 V vs. NHE	17
Co(tpfc)(py) ₂	530	>95	pH 7.0, 0.1 M phosphate buffer, 1.4 V vs. Ag/AgCl	18
[CoL ^{DMA} (CH ₃ CN) ₂] [BF ₄] ₂	-	99	0.1 M TBABF ₄ , 95 : 5 CH ₃ CN : H ₂ O (v/v), 1.07 V vs. Fc/Fc ⁺	19
[Co ^{III} (dpaq)(Cl)]Cl	500	81	pH 8.0, 0.1 M phosphate buffer, 1.5 V vs. NHE	20
CoH ^{BF} CX-CO ₂ H	~600	~100	pH 7, 0.1 M phosphate buffer, 1.4 V vs. Ag/AgCl	21
[Co(TPA-tri- α F)Cl] Cl	~420	-	pH 8, borate buffer	22
Co(TCA) ₂ ·2H ₂ O	360	-	pH 6, 0.1 M sodium acetate	23

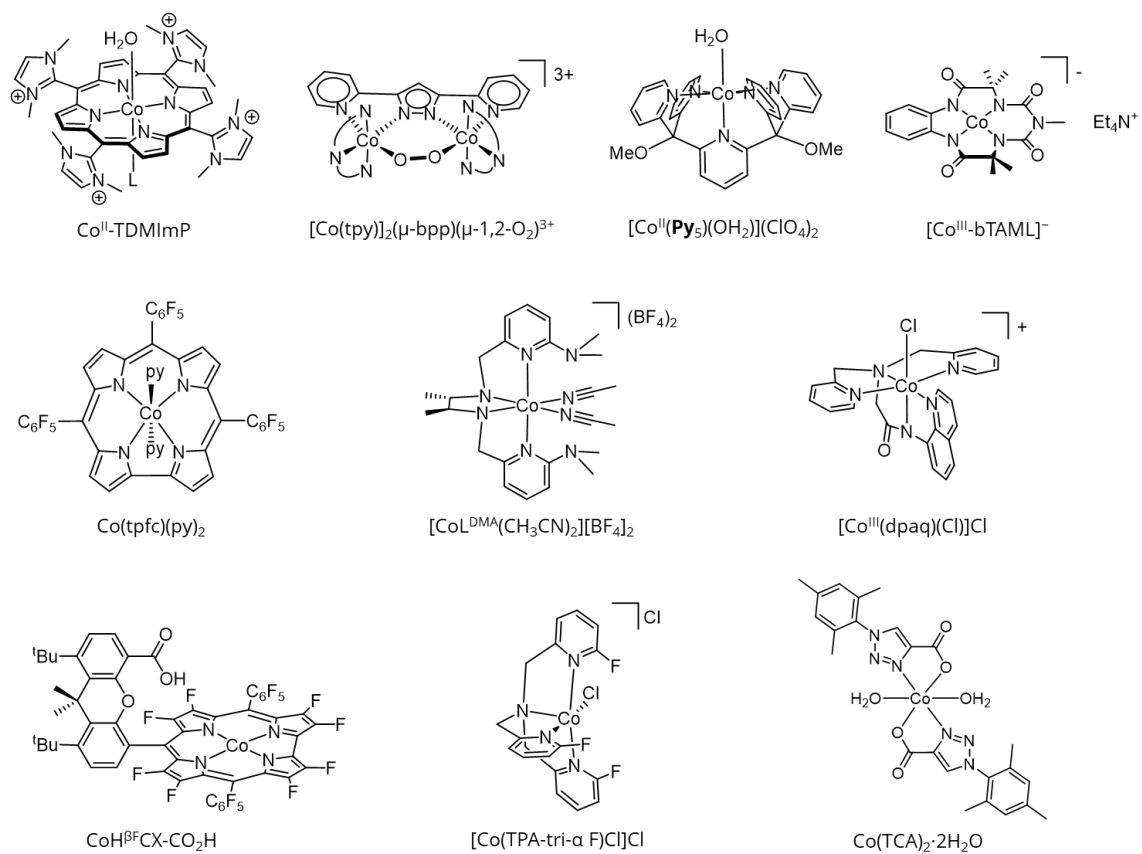


Figure 15. Molecular structures of cobalt-complex-based catalysts for water oxidation shown in Table 6.

Conclusion

In conclusion, we have developed a facile method to integrate molecule-based catalytic centers and hole transporters into one material. The electrochemical polymerization of the precursor with a cobalt-cubane moiety and carbazole units afforded a film-based material (**Poly-1**). The characterization of **Poly-1** was performed by various experimental techniques, including UV-vis absorption spectroscopy IR spectroscopy, SEM and EDX, and the integration of two functional units were confirmed. The properties of **Poly-1** was analyzed by EIS and the high transporting ability was clarified. Moreover, **Poly-1** can catalyze the water oxidation reaction with a high faradaic efficiency and a low over potential. Notably, the results of control experiments disclosed that the integration of two functional units are essential to achieve excellent activity of **Poly-1** (Figure 16). Our study is a significant example of a molecule-based catalytic system that mimics the key features of the OEC; the systems with a catalytic center surrounded by hole transporting units. Collectively, the present study offers a novel concept for obtaining efficient catalytic system for water oxidation.

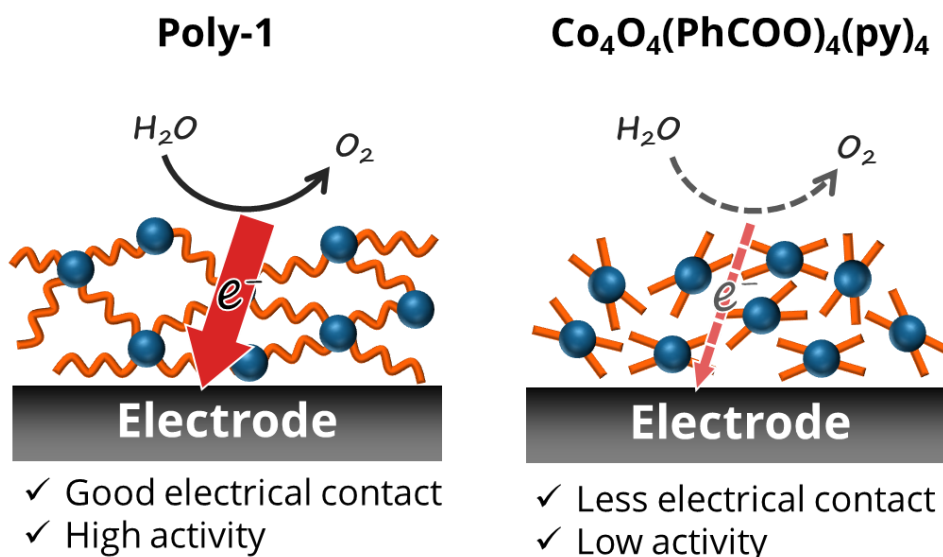


Figure 16. Schematics of the comparison of properties between **Poly-1**@GC, Co₄O₄(PhCOO)₄(py)₄@GC.

Experimental section

Materials

All reagents were purchased from Tokyo Chemical Industry Co., Ltd., FUJIFILM Wako Pure Chemical Co., Kanto Chemical Co. Inc. and used without further purification. Unsubstituted cubane complex $\text{Co}_4\text{O}_4(\text{OAc})_4(\text{py})_4$ and $\text{Co}_4\text{O}_4(\text{PhCOO})_4(\text{py})_4$ was synthesized according to published procedure.[13,24]

Measurement apparatus

^1H NMR spectra were acquired on a JEOL JNM-LA400 spectrometer, where chemical shifts in $\text{DMSO}-d_6$ or CD_2Cl_2 were referenced to internal tetramethylsilane. Elemental analyses were carried out on a J-SCIENCE LAB MICRO CORDER JM10 elemental analyser. UV-Vis absorption spectra were recorded on a Shimadzu UV-3600 UV-Vis-NIR spectrophotometer. FT-IR spectra were measured on a Perkin Elmer Spectrum 100 spectrometer by attenuated total reflection method. Cyclic voltammograms and electrochemical impedance spectra were measured at room temperature on a BAS ALS Model 650DKMP electrochemical analyser. Glassy carbons (disk and plate), platinum wire, and Ag/Ag^+ electrode ($\text{Ag}/0.01 \text{ M AgNO}_3$) were used as the working, auxiliary, and reference electrodes, respectively for the measurements in organic solvents. The redox potentials were calibrated against the redox potential for the ferrocene/ferrocenium (Fc/Fc^+) couple in organic solvents. Ag/AgCl reference electrode were used for measurements in aqueous media. Electrochemical impedance spectra were recorded on a bias potential at 1.30 V vs. Ag/AgCl with 0.1 Hz-100 kHz measurement range. Recorded data was fitted with the equivalent circuit by ALS /CHI50D software. SEM-EDX spectra were recorded a Hitachi high-technologies SU-6600 and a BrukerAXS XFlash5060FQ (5 kV acceleration voltage). Gas analysis for O_2 was performed using a Shimadzu GC-2014 gas chromatograph equipped with a thermal conductivity detector (TCD) and fitted with a molecular sieve 5A column (Ar carrier gas), calibrated with standard O_2 .

X-ray crystal structure analysis

A crystal was mounted in a loop coated with Paratone-N (Hampton Research Corp., Aliso Viejo, CA, USA). Single crystal X-ray diffraction data were collected on a Rigaku MicroMax-007HF/XtalLAB SynergyCustom equipped with confocal monochromated Mo-K α radiation ($\lambda = 0.71069$ Å). Data was processed using CrysAlisPro system software.[25] The structure was solved by dual-space algorithm using SHELXT program[26] through the Olex2 interface[27]. All non-hydrogen atoms were refined anisotropically using a least-squares method, and hydrogen atoms were fixed at calculated positions and refined using a riding model. SHELXL-2014/7 was used for structure refinement.[28] Full-matrix least-squares refinements on F^2 based on unique reflections with unweighted and weighted agreement factors of $R = \Sigma||F_o| - |F_c||/\Sigma|F_o|$ ($I > 2.00 \sigma(I)$) and $wR = [\Sigma w(F_o^2 - F_c^2)^2/\Sigma w(F_o^2)^2]^{1/2}$ were performed. Mercury 4.0.0 was used for visualization and analysis of the structure. Crystallographic data have been deposited with Cambridge Crystallographic Data Centre: Deposition number CCDC 1922963 for **1**. Copies of the data can be obtained free of charge via www.ccdc.cam.ac.uk/data_request/cif.

Synthesis of carbazole-9-propionic acid

Carbazole (802 mg, 4.80 mmol), KOH (1.60 g, 28.5 mmol) and ethyl 3-bromopropionate (0.764 mL, 5.96 mmol) were added to 20 mL of DMF. The mixture was refluxed for 5 h. The resultant solution was acidified with HCl aq. until pH~1. The precipitate was filtered off and washed with water. The obtained solid was purified by column chromatography over silica gel (EtOAc:hexane 50:50 to 100:0). First fraction contained unreacted carbazole, and second fraction was collected to afford the target compound as a white crystalline solid (651 mg, 56.7%). ¹H NMR (δ , DMSO-*d*₆): 12.37 (s, 1H), 8.14 (m, 2H), 7.62 (d, *J* = 8.2 Hz, 2H), 7.45 (ddd, *J* = 8.2 Hz, 7.1, 1.1, 2H), 7.20 (m, 2H), 4.63 (t, *J* = 6.8 Hz, 2H), 2.75 (t, *J* = 6.1 Hz, 2H).

Synthesis of Co₄O₄(czp)₄(py)₄ (I)

Co₄O₄(OAc)₄(py)₄ (100 mg, 0.125 mmol) and Hczp (230 mg, 0.96 mmol) was added to 10 mL of MeCN. The mixture was heated at 60 °C for 1 h. The reaction was monitored by TLC until the starting materials were disappeared. After the solvent was removed in vacuo, the residue was extracted by CH₂Cl₂/brine. The organic layer was dried over MgSO₄ and concentrated in vacuo. Olive green solid was purified by column chromatography over silica gel (CHCl₃:MeOH 90:10). Olive green fraction was collected. Deep green crystals were obtained from CH₂Cl₂/Et₂O (124 mg, 65.9%). ¹H NMR (δ , CD₂Cl₂): 8.11 (d, *J* = 7.6 Hz, 8H), 7.72 (s, 8H), 7.43 (m, 8H), 7.33 (m, 12H), 7.20 (m, 8H), 6.64 (m, 8H), 4.59 (m, 8H), 3.01 (m, 8H). Elemental analysis calcd (%) for Co₄O₄(czp)₄(py)₄·1.6CH₂Cl₂: C 57.48, H 4.21, N 6.57; found: C 57.36, H 4.37, N 6.52.

Preparation of Poly-1@GC

The **Poly-1** modified GC plate was made by cyclic voltammetry technique. Measurements was performed in 0.19 mM solution of **1** in a CH₂Cl₂ solution containing 0.1 M TBAPF₆ under Ar at a scan rate of 100 mV s⁻¹. Working electrode, GC plate; counter electrode, Pt wire; reference electrode, Ag/Ag⁺. CV scans were performed in the range of 0-1.5 V (vs. Ag/Ag⁺), 10 cycles and used as the working electrode.

Preparation of Co₄O₄(PhCOO)₄(py)₄@GC

The electrode modified with Co₄O₄(PhCOO)₄(py)₄ (Co₄O₄(PhCOO)₄(py)₄@GC) was made by drop cast method; 40 μL of 0.5 mM CH₂Cl₂ solution of Co₄O₄(PhCOO)₄(py)₄ was dropped on a GC plate and dried under air.

Preparation of cobalt phosphate modified ITO electrode

As a reference compound, oxidized cobalt phosphate inorganic materials were deposited on ITO electrode following the reported method.[29] 0.2 M phosphate buffer solution containing 0.5 mM of Co(NO₃)₂·6H₂O was electrolyzed for 3 h at 1.3 V vs. Ag/AgCl with ITO electrode as a working, Pt wire as a counter and Ag/AgCl as a reference electrode.

References

- [1] (a) D. G. Nocera, M. P. Nash, *Proc. Natl. Acad. Sci.* **2007**, *104* (43), 15729–15735. (b) P. V. Kamat, *J. Phys. Chem. C* **2007**, *111* (7), 2834–2860. (c) T. R. Cook, D. K. Dogutan, S. Y. Reece, Y. Surendranath, T. S. Teets, D. G. Nocera, *Chem. Rev.* **2010**, *110* (11), 6474–6502.
- [2] (a) X. Liu, F. Wang, *Coord. Chem. Rev.* **2012**, *256*, 1115–1136. (b) A. Singh, L. Spiccia, *Coord. Chem. Rev.* **2013**, *257*, 2607–2622. (c) M. D. Kärkäs, O. Verho, E. V. Johnston, B. Åkermark, *Chem. Rev.* **2014**, *114* (24), 11863–12001. (d) J. D. Blakemore, R. H. Crabtree, G. W. Brudvig, *Chem. Rev.* **2015**, *115*, 12974–13005. (e) M. Kondo, S. Masaoka, *Chem. Lett.* **2016**, *45* (11), 1220–1231. (f) B. Zhang, L. Sun, *Chem. Soc. Rev.* **2019**, *48*, 2216–2264. (g) S. Ye, C. Ding, M. Liu, A. Wang, Q. Huang, C. Li, *Adv. Mater.* **2019**, *31*, 1902069. (h) Z. N. Zahran, Y. Tsubonouchi, E. A. Mohamed, M. Yagi, *ChemSusChem* **2019**, *12*, 1775–1793.
- [3] (a) J. P. McEvoy, G. W. Brudvig, *Chem. Rev.* **2006**, *106* (11), 4455–4483. (b) T. J. Meyer, M. H. V. Huynh, H. H. Thorp, *Angew. Chem. Int. Ed.* **2007**, *46* (28), 5284–5304.
- [4] J. Barber, *Chem. Soc. Rev.* **2009**, *38* (1), 185–196.
- [5] (a) S. W. Gersten, G. J. Samuels, T. J. Meyer, *J. Am. Chem. Soc.* **1982**, *104* (14), 4029–4030. (b) Y. Naruta, M. Sasayama, T. Sasaki, *Angew. Chem. Int. Ed.* **1994**, *33* (18), 1839–1841. (c) J. Limburg, J. S. Vrettos, L. M. Liable-Sands, A. L. Rhingold, R. H. Crabtree, G. W. Brudvig, *Science* **1999**, *283*, 1524–1527. (d) J. L. Fillol, Z. Codolà, I. Garcia-Bosch, L. Gàmez, J. J. Pla, M. Costas, *Nat. Chem.* **2011**, *3* (10), 807–813. (e) L. Duan, F. Bozoglian, S. Mandal, B. Stewart, T. Privalov, A. Llobet, L. Sun, *Nat. Chem.* **2012**, *4* (5), 418–423. (f) S. M. Barnett, K. I. Goldberg, J. M. Mayer, *Nat. Chem.* **2012**, *4*, 498–502. (g) D. Wang, J. T. Groves, *Proc. Natl. Acad. Sci.* **2013**, *110* (39), 15579–15584.
- [6] (a) M. Okamura, M. Kondo, R. Kuga, Y. Kurashige, T. Yanai, S. Hayami, V. K. K. Praneeth, M. Yoshida, K. Yoneda, S. Kawata, et al. *Nature* **2016**, *530* (7591), 465–468. (b) V. K. K. Praneeth, M. Kondo, P. M. Woi, M. Okamura, S. Masaoka, *Chempluschem* **2016**, *81* (10), 1123–1128. (c) V. K. K. Praneeth, M. Kondo, M. Okamura, T. Akai, H. Izu, S. Masaoka, *Chem. Sci.* **2019**, *10* (17), 4628–4639. (d)

- M. Kondo, S. Masaoka, *Acc. Chem. Res.* **2020**, *53* (10), 2140-2151.
- [7] (a) J. Mola, E. Mas-Marza, X. Sala, I. Romero, M. Rodríguez, C. Viñas, T. Parella, A. Llobet, *Angew. Chem. Int. Ed.* **2008**, *47* (31), 5830–5832. (b) D. L. Ashford, A. M. Llapides, A. K. Vannucci, K. Hanson, D. A. Torelli, D. P. Harrison, J. L. Templeton, T. J. Meyer, *J. Am. Chem. Soc.* **2014**, *136* (18), 6578–6581. (c) D. L. Ashford, B. D. Sherman, R. A. Binstead, J. L. Templeton, T. J. Meyer, *Angew. Chem. Int. Ed.* **2015**, *54* (16), 4778–4781. (d) L. Wang, K. Fan, Q. Daniel, L. Duan, F. Li, B. Philippe, H. Rensmo, H. Chen, J. Sun, L. Sun, *Chem. Commun.* **2015**, *51* (37), 7883–7886.
- [8] (a) N. S. McCool, D. M. Robinson, J. E. Sheats, G. C. Dismukes, *J. Am. Chem. Soc.* **2011**, *133* (30), 11446–11449. (b) J. Li, Y. Jiang, Q. Zhang, X. Zhao, N. Li, H. Tong, X. Yang, L. Xia, *RSC Adv.* **2017**, *7* (7), 4102–4107. (c) Y. Wang, F. Li, X. Zhou, F. Yu, J. Du, L. Bai, L. Sun, *Angew. Chem. Int. Ed.* **2017**, *56* (24), 6911–6915.
- [9] K. Karon, M. Lapkowski, *J. Solid State Electrochem.* **2015**, *19* (9), 2601–2610.
- [10] L. Kortekaas, F. Lancia, J. D. Steen, W. R. Browne, *J. Phys. Chem. C* **2017**, *121* (27), 14688–14702.
- [11] X. Fan, J. You, T. Jiao, G. Tan, X. Yu, *Org. Prep. Proced. Int.* **2000**, *32* (3), 284–287.
- [12] A. I. Nguyen, J. Wang, D. S. Levine, M. S. Ziegler, T. D. Tilley, *Chem. Sci.* **2017**, *8* (6), 4274–4284.
- [13] R. Chakrabarty, S. J. Bora, B. K. Das, *Inorg. Chem.* **2007**, *46* (22), 9450–9462.
- [14] S. H. Hsiao, S. W. Lin, *Polym. Chem.* **2016**, *7* (1), 198–211.
- [15] M. L. Rigsby, S. Mandal, W. Nam, L. C. Spencer, A. Llobet, S. S. Stahl, *Chem. Sci.* **2012**, *3* (10), 3058–3062.
- [16] D. J. Wasylenko, C. Ganesamoorthy, J. Borau-Garcia, C. P. Berlinguette, *Chem. Commun.* **2011**, *47* (14), 4249–4251.
- [17] D. Das, S. Pattanayak, K. K. Singh, B. Garai, S. S. Gupta, *Chem. Commun.* **2016**, *52* (79), 11787–11790.
- [18] H. Lei, A. Han, F. Li, M. Zhang, Y. Han, P. Du, W. Lai, R. Cao, *Phys. Chem. Chem. Phys.* **2014**, *16* (5), 1883–1893.
- [19] J. F. Khosrowabadi Kotyk, C. M. Hanna, R. L. Combs, J. W. Ziller, J. Y. Yang, *Chem.*

- Sci.* **2018**, *9* (10), 2750–2755.
- [20] S. Biswas, S. Bose, J. Debgupta, P. Das, A. N. Biswas, *Dalton Trans.* **2020**, *49* (21), 7155–7165.
- [21] D. K. Dogutan, R. McGuire, D. G. Nocera, *J. Am. Chem. Soc.* **2011**, *133* (24), 9178–9180.
- [22] S. Liu, Y. J. Lei, Z. J. Xin, R. J. Xiang, S. Styring, A. Thapper, H. Y. Wang, *Int. J. Hydrogen Energy* **2017**, *42*, 29716–29724.
- [23] H. A. Younus, N. Ahmad, A. H. Chughtai, M. Vandichel, M. Busch, K. V. Hecke, M. Yusubov, S. Song, F. Verpoort, *ChemSusChem* **2017**, *10* (5), 862–875.
- [24] R. Chakrabarty, P. Sarmah, B. Saha, S. Chakravorty, and B. K. Das, *Inorg. Chem.* **2009**, *48*, 6371–6379.
- [25] CrysAlisPro, Oxford Diffraction Ltd., Version 1.171.39.46.
- [26] G. M. Sheldrick, *Acta Cryst.* **2015**, *A71*, 3-8.
- [27] O. V. Dolomanov, L. J. Bourhis, R. J. Gildea, J. A. K. Howard and H. Puschmann, *J. Appl. Crystallogr.* **2009**, *42*, 339-341.
- [28] G.M Sheldrick., *Acta Cryst.* **2015**, *C71*, 3-8.
- [29] M. W. Kanan and D. G. Nocera, *Science* **2008**, *321*, 1072-1075.

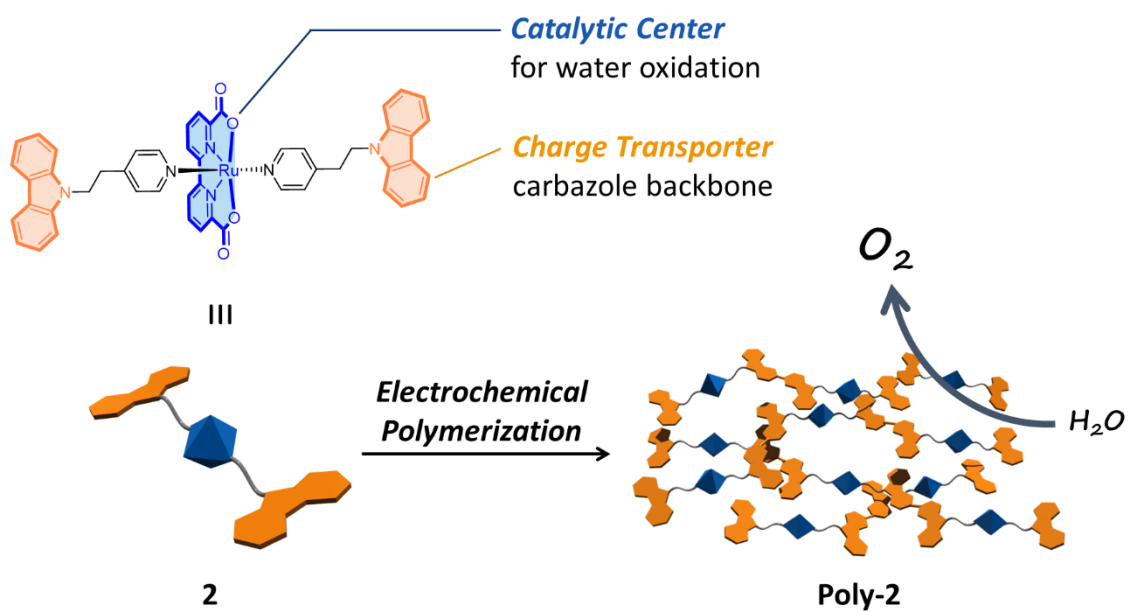
Chapter 2

Facile Construction of Function-Integrated Water Oxidation System *via* Electrochemical Polymerization

Introduction

Four-electron oxidation of water ($2\text{H}_2\text{O} \rightarrow \text{O}_2 + 4\text{H}^+ + 4\text{e}^-$) is a key reaction in artificial photosynthesis which could address global energy problems.[1] However, this reaction is energetically unfavorable due to the removal of four electrons and four protons with O-O bond formation.[2] Therefore, the efficient catalyst for water oxidation is highly desired. Particularly, the electrochemical process is a promising way for water oxidation in a clean manner because the working electrode receives the electrons, and any harmful oxidant is not required. For these reasons, it is an important issue that development of the electrochemically active catalyst for water oxidation.

As described in chapter 1, I demonstrated that the integration of charge transporter and water oxidation catalyst enhances electrocatalytic activity. The introduction of carbazole moiety into the tetranuclear cobalt complex allows the direct polymerization of complex **1** and the reduction of charge transfer resistance during the catalytic reaction. In this chapter, I demonstrated that a mononuclear Ru complex bearing carbazole moieties also underwent electrochemical polymerization and the deposited polymer worked as a good electrocatalyst for water oxidation.



Scheme 1. (Top) Structure of the mononuclear Ru complex monomer (**2**) developed in this study. (Bottom) Schematic illustration of the preparation of function-integrated catalytic system for water oxidation via the electrochemical polymerization of **2**.

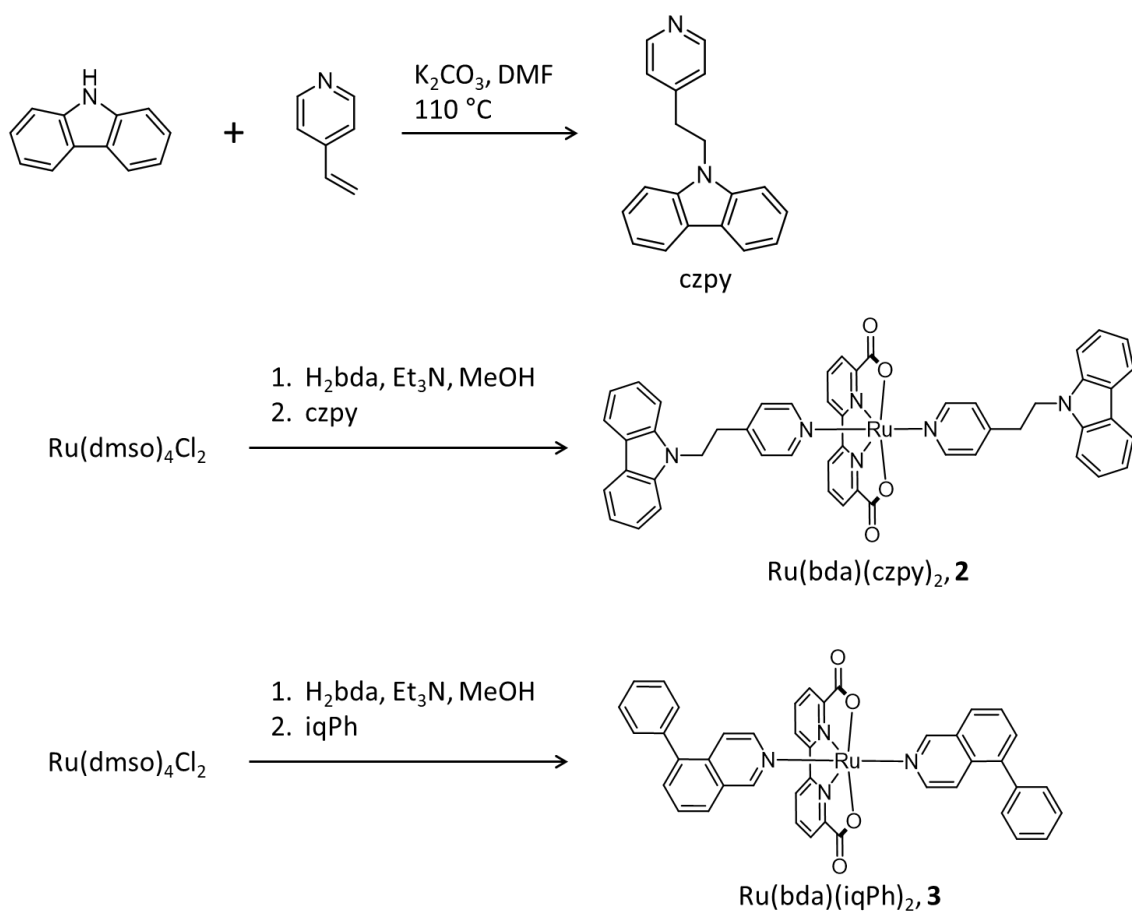
Results and discussions

The structure of mononuclear Ru complex monomer, **2**, is shown in Scheme 1. **2** is composed of two different functional units: (i) Ru(bda) (bda²⁻ = 2,2'-bipyridine-6,6'-dicarboxylate) core as a water oxidation catalyst, (ii) carbazole for polymerizing backbone and charge transporter. Catalytic water oxidation ability of mononuclear Ru(bda) core was first reported by L. Sun and co-workers in 2012.[3] Experimental and theoretical studies suggested that the 7-coordinated Ru center is the catalytic intermediate, which is expected to provide a stable catalyst system.[4] Carbazole derivatives are known to dimerize at 3- or 6-position under oxidative conditions.[5] In addition, the formed biscarbazole exhibits hole-transfer ability,[6] which should favor the oxidative catalytic reaction. Therefore, integration of catalytic centers and hole transporters should be also accessible (**Poly-2**, Scheme 1, bottom) by the electrochemical polymerization of **2**.

Synthesis of complex **2** and **3**

The Ru complex monomer, **2**, was synthesized by following Scheme 2. Initially, 9-[2-(4-pyridinyl)ethyl]carbazole (czpy) was synthesized by N-alkylation of carbazole with 4-vinyl pyridine. Subsequently, Ru(dmsO)₄Cl₂ (dmsO = dimethylsulfoxide) was reacted with H₂bda in MeOH and Et₃N under N₂ atmosphere. Following addition of czpy, **2** was formed by substitution of the axial position from dmsO into czpy. After the purification over alumina column chromatography and recrystallization, complex **2** was isolated in 33.6% yield. Complex **2** was characterized by ¹H NMR spectroscopy, elemental analysis, MALDI-MS, and single-crystal X-ray diffraction analysis.

Ru(bda)(iqPh)₂ (iqPh = 5-phenylisoquinoline, complex **3** was synthesized for the comparisons of electrochemical properties in heterogeneous system (*vide infra*). iqPh was introduced in the axial ligand of Ru(bda) core, which decreased the solubility in water and allowed us to verify the detailed electrochemical analysis. The synthesis method was identical to **2** except for the axial ligand. Complex **3** was also characterized by ¹H NMR spectroscopy, elemental analysis, MALDI-MS, and single-crystal X-ray diffraction analysis.



Scheme 2. Synthetic scheme of complex **2** and **3**.

Single crystal structure analysis

Single crystals of **2** suitable for X-ray diffraction measurements were obtained by vapor diffusion of ^tBuOMe into the mixture of MeOH and MeCN at room temperature. **2** crystallized in $P\bar{1}$, and contains MeOH, MeCN, and H₂O as crystal solvents. One carboxylate of bda ligand did not coordinate to Ru and one MeCN molecule coordinated instead in the crystals (Figure 1). For this reason, Ru-N2 bond was elongated and Ru-O1 bond was shortened compared with complex **3** (Table 3). The coordination angles in the same plane to bda ligand were close to 90° because of less restriction of the tridentate bda ligand than that of tetradentate. The coordinating MeCN molecule can be removed by drying under reduced pressure because the elemental analysis and MALDI-MS were matched with the formula without any solvents.

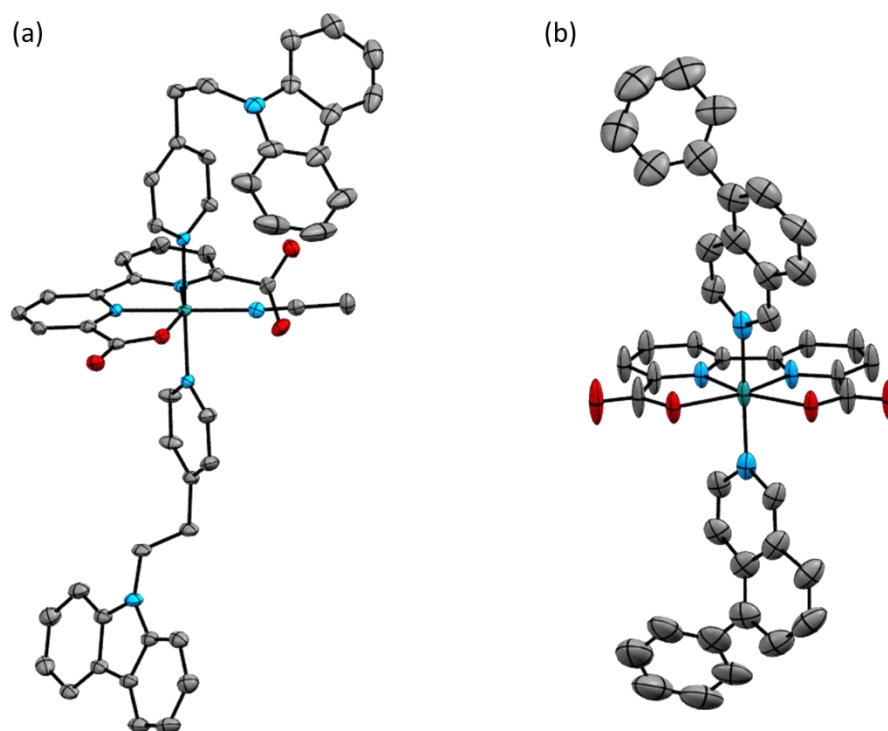


Figure 1. ORTEP drawings of (a) **2** and (b) **3**. Solvent molecules and hydrogen atoms are omitted for clarity. Thermal ellipsoids are shown at the 50% for **2** and 30% probability level for **3**. Color chart: green: Ru, grey: C, cyan: N, red: O.

Table 1. Crystallographic parameters of complexes **2** and **3**.

Formula	RuC ₅₂ H ₄₁ N ₇ O ₄ ·CH ₃ OH· CH ₃ CN·0.5H ₂ O (2)	RuC ₄₂ H ₂₈ N ₄ O ₄ ·H ₂ O· 0.5CHCl ₃ (3)
Fw	1011.09	964.32
Crystal color, habit	Brown, block	Brown, needle
Crystal size (mm ³)	0.406 × 0.108 × 0.065	0.462 × 0.58 × 0.57
Crystal system	Triclinic	Monoclinic
Space group	<i>P</i> $\bar{1}$	<i>C</i> 2/ <i>m</i>
<i>a</i> (Å)	9.1381(3)	8.0216(2)
<i>b</i> (Å)	15.8358(4)	25.5228(11)
<i>c</i> (Å)	17.5492(5)	20.9876(5)
α (°)	67.752(3)	90
β (°)	86.199(3)	96.734(2)
γ (°)	85.407(2)	90
<i>V</i> (Å ³)	2341.14(13)	4267.2(2)
<i>Z</i>	2	4
F(000)	1046	1950
<i>T</i> (K)	123	143
<i>R</i> ₁	0.0545	0.0846
<i>wR</i> ₂	0.1390	0.2504
GooF	1.005	1.088

Table 2. Selected structural parameters of **2** and **3**.

2		3	
Ru1-O1	2.115(2) Å	Ru1-O1	2.189(4) Å
Ru1-N1	1.939(2) Å	Ru1-N1	1.927(4) Å
Ru1-N2	2.072(2) Å	Ru1-N2	1.947(4) Å
Ru1-N7	2.044(2) Å	Ru1-O3	2.187(4) Å
O1-Ru1-N1	79.58(8)°	O1-Ru1-N1	77.52(17)°
N1-Ru1-N2	80.00(8)°	N1-Ru1-N2	81.22(19)°
N2-Ru1-N7	103.80(9)°	N2-Ru1-O3	77.68(17)°
N7-Ru1-O1	96.64(8)°	O3-Ru1-O1	123.58(15)°

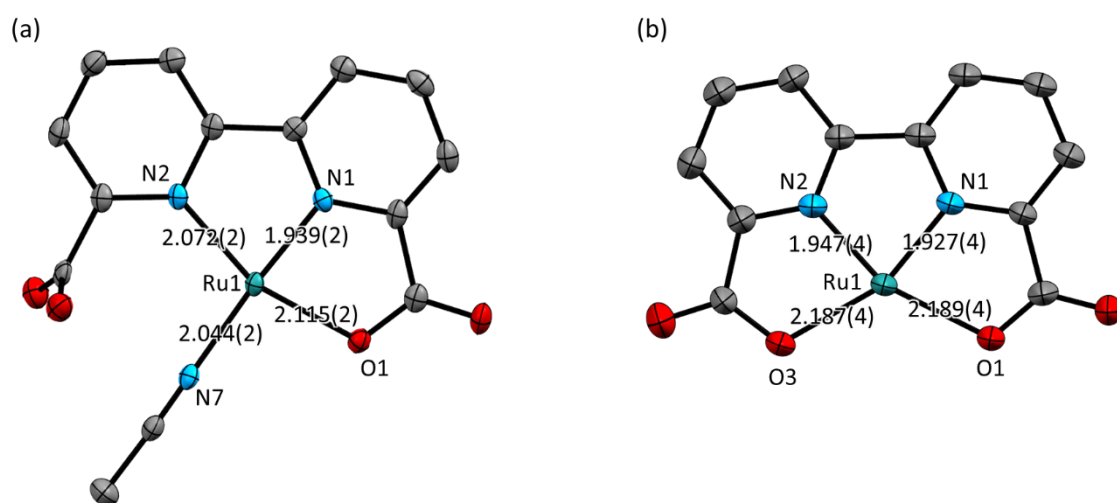


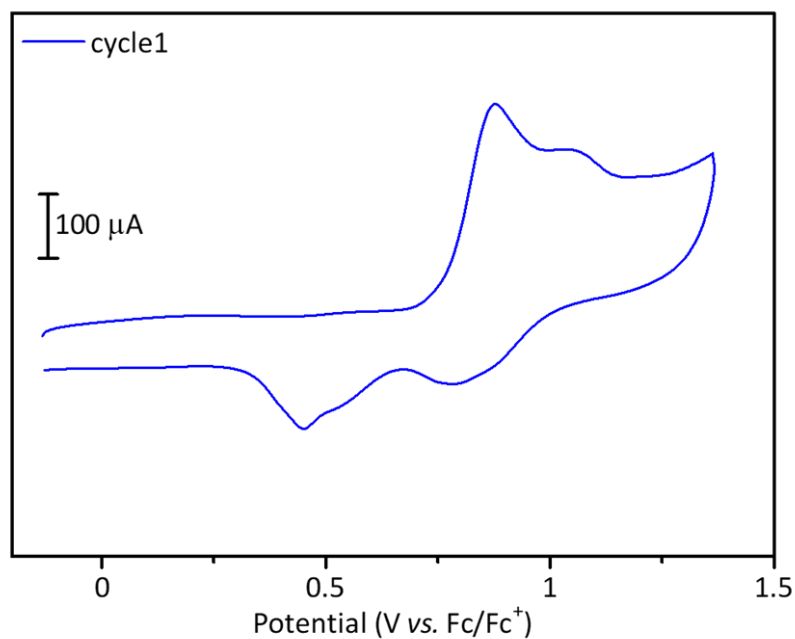
Figure 2. Crystal structure around Ru centers of **2** (a) and **3** (b).

Electrochemistry

The electrochemical behaviors of **2** were investigated by cyclic voltammetry (CV) in the organic solvent (0.1 M tetra-*n*-butylammonium perchlorate (TBAP) in MeCN). 1% of trifluoroacetic acid (TFA) was added before the measurements because of the low solubility of **2** in pure MeCN. In the first scan, a large peak was observed at approximately 0.7 V (vs. Fc/Fc⁺), which is attributed to the oxidation and subsequent dimerization of carbazole moieties. In the reverse scan and following scans, two reversible redox peaks around 0.5 and 0.8 V were observed. These peaks could be assigned to two-step redox of biscarbazole moieties.[6] The electrochemical behavior of **2** was similar to that of complex **1** described in chapter 1. Therefore, it is suggested that **2** polymerized by electrochemical oxidation via the dimerization of the carbazole moiety.

Cyclic voltammogram and square wave voltammogram (SWV) of **3** were shown in Figure 4. The first oxidation peak at -0.04 V was attributed Ru^{III}/Ru^{II} redox,[7] and latter small peaks could be further oxidation of Ru center. Because the peaks were broad and split, the clear assignment was unsuccessful.

(a)



(b)

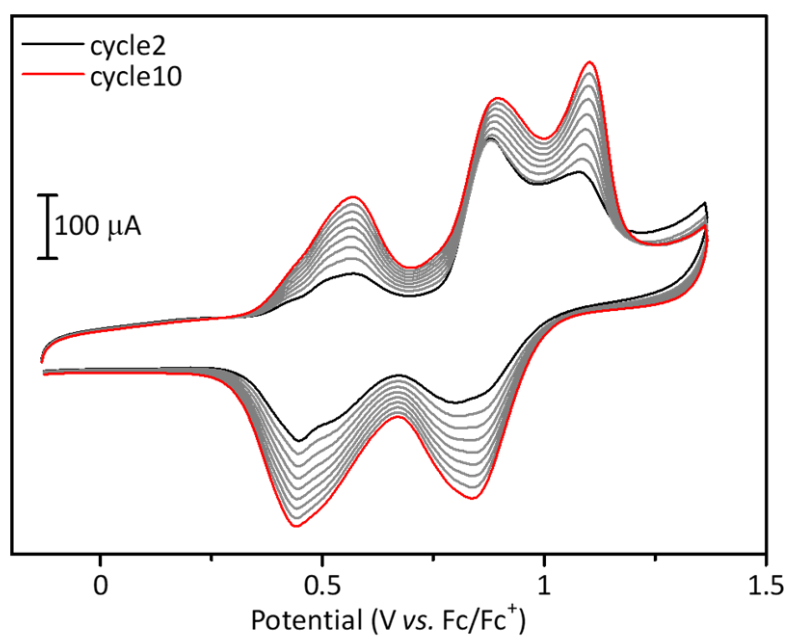


Figure 3. Cyclic voltammograms of a 0.2 mM solution of **2**. (a) 1st scan and (b) 2nd to 6th scans. Measurements were performed in a MeCN solution containing 0.1 M TBAP and 1% of TFA under Ar at a scan rate of 100 mV s⁻¹. Working electrode, glassy carbon; counter electrode, Pt wire; reference electrode, Ag/Ag⁺. CV scans were initiated from the open-circuit potential.

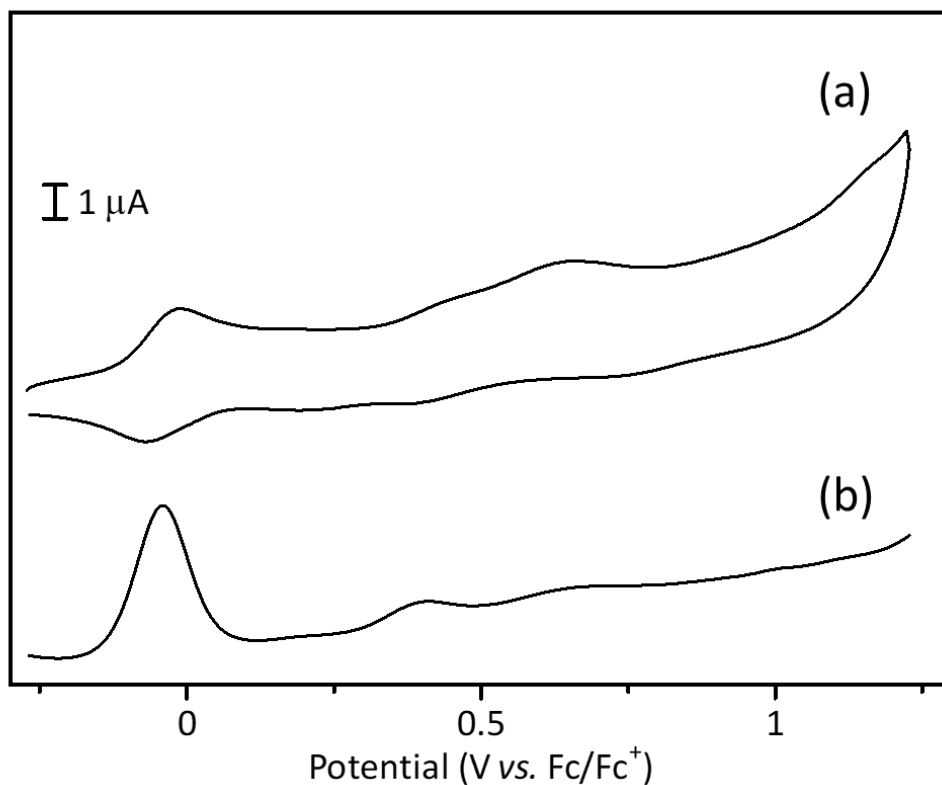


Figure 4. (a) Cyclic voltammogram of a 0.2 mM solution of **3** at a scan rate of 100 mV s⁻¹. (b) Square wave voltammogram of 0.2 mM solution of **3** at a scan rate of 60 mV s⁻¹. Measurements were performed in a MeCN solution containing 0.1 M TBAP and 1% of TFA under Ar. Working electrode, glassy carbon; counter electrode, Pt wire; reference electrode, Ag/Ag⁺. CV scans were initiated from the open-circuit potential.

Characterization of Poly-2

To verify the formation of **Poly-2**, UV-Vis-NIR spectra of **Poly-2** were measured with a transparent electrode (ITO plate) as a working electrode. In a 0.1 M TBAP-MeCN solution containing 1% of TFA and 0.2 mM of **1**, a constant potential (1.3 V vs. Ag/Ag⁺) was applied for 30-150 s. The UV-Vis-NIR absorption spectra after the electrolysis are shown in Figure 5. A band center at approximately 420 nm and a broad band at approximately 800 nm were observed in all cases, and the intensities of the bands gradually increased as the electrolysis time increased. The band around 1000 nm can mainly be attributed to the intervalence charge transfer (IVCT) transitions of mixed-valent biscarbazole units or charge-resonance bands in the case of Robin-Day class III systems.[6,8] These characters were similar to **Poly-1**, and the formation of biscarbazole was indicated.

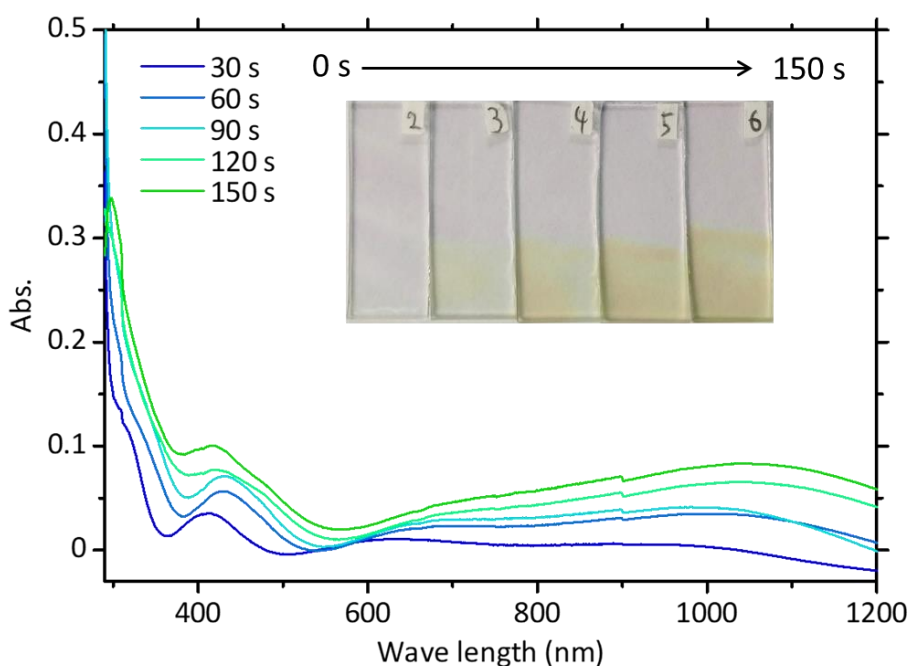


Figure 5. UV-Vis-NIR absorption spectra of the ITO electrodes electrolyzed at 1.3 V vs. Ag/Ag⁺ for 10-90 s using a 0.1 M TBAP-MeCN (1% TFA) solution containing 0.2 mM of **2**. (Inset) Photographs of the ITO electrodes after the electrolysis.

Poly-2 was further analyzed by FT-IR spectroscopy. Absorption bands at coordinating COO^- and pyridine (1600 cm^{-1}) and pyridine ring vibration mode ($\sim 750\text{ cm}^{-1}$) were observed before and after the polymerization. In the case of **Poly-2**, a specific absorption at 1100 cm^{-1} which is originated from ClO_4^- to compensate for the total charge of as-synthesized **Poly-2**. [9] The data suggested that complex **2** was polymerized without losing the structure of the catalytic center.

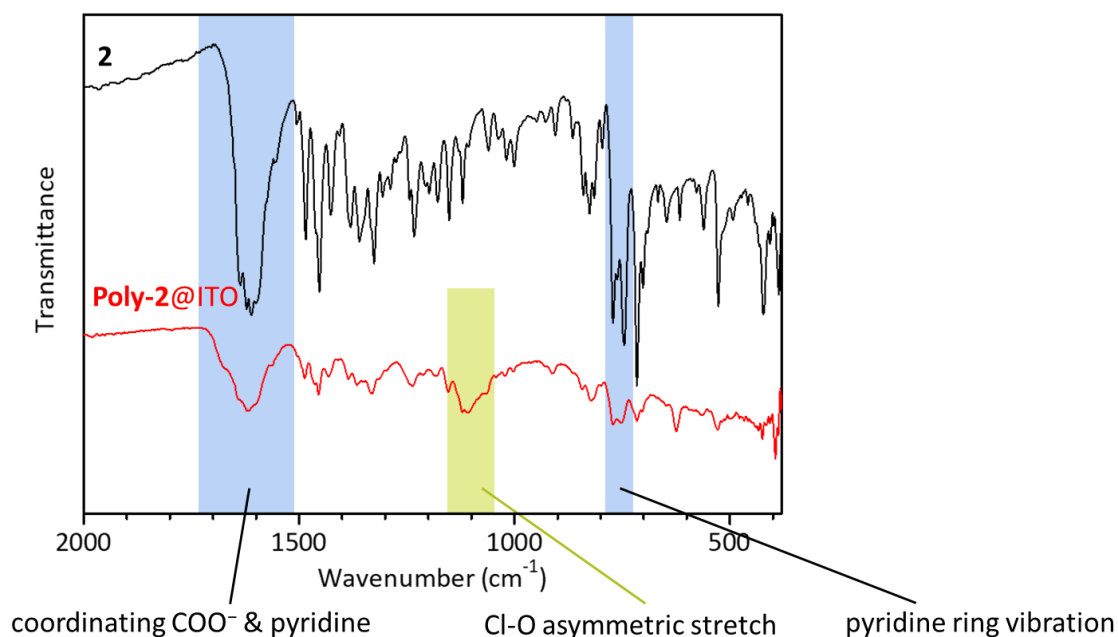


Figure 6. FT-IR spectra of **2** (black line) and **Poly-2@ITO** (red line).

Scanning electron microscopy (SEM) analysis was also conducted. The SEM image of the polymer shows some spherical aggregates on ITO (Figure 7, left). However, the energy dispersive X-ray (EDX) map image suggested a homogeneous distribution of ruthenium (Figure 7, right). Therefore, **Poly-2** covered ITO electrode uniformly and the spherical aggregates could be inorganic impurities or dissociated czpy ligand. In EDX spectrum (Figure 8), peaks attributable to ruthenium and chlorine were observed very close energy region. From the insight of complex **1**, **Poly-2** and ClO_4^- were expected to be detected, however, they could not be distinguished. For further investigation, different anions (e.g. BF_4^- or PF_6^-) should be used as an electrolyte. These observations indicate that **2** is also electrochemically polymerized to uniform polymer, **Poly-2**.

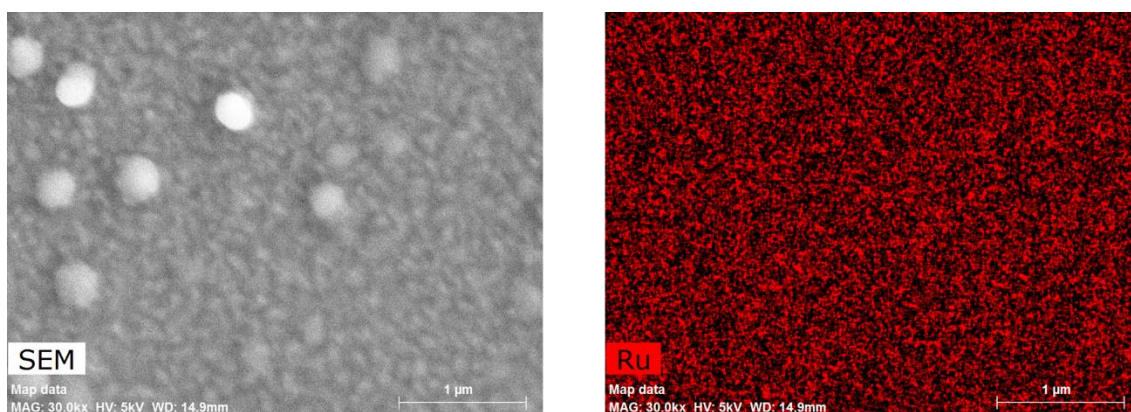


Figure 7. A SEM image (left) and an EDX elemental map (right) of **Poly-2** fabricated on an ITO electrode by controlled potential electrolysis at 1.3 V vs. Ag/Ag^+ for 180 s using a 0.1 M TBAP-MeCN (1% TFA) solution containing 0.2 mM of **2**.

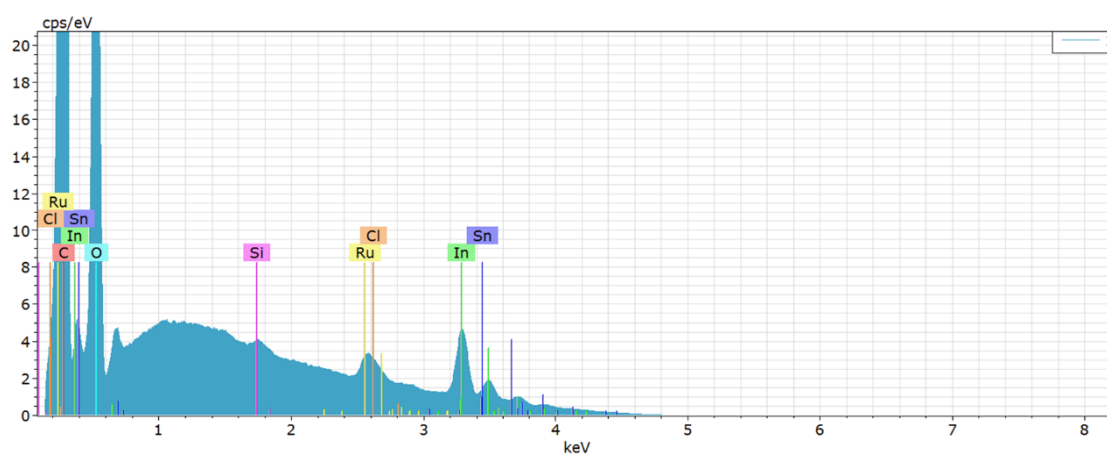


Figure 8. An EDX spectrum of **Poly-2** fabricated on an ITO electrode by controlled potential electrolysis at 1.3 V vs. Ag/Ag^+ for 180 s using a 0.1 M TBAP-MeCN (1% TFA) solution containing 0.2 mM of **2**.

Electrochemical impedance spectroscopy

To clarify the charge transfer ability of **Poly-2**, electrochemical impedance spectra (EIS) were measured. EIS were measured for a bare glassy carbon (GC) electrode, the GC electrode modified with **Poly-2** (**Poly-2@GC**) and **3** (**3@GC**). Figure 9 shows the EIS measured at 1.30 V vs. Ag/AgCl of the bias potential. The diameters of semicircles in Nyquist plots were decreased in the order of a bare GC, **3@GC**, and **Poly-2@GC**. Fitted charge transfer resistance (R_{CT}) values with the equivalent circuit (Figure 9 inset) of a bare GC, **3@GC**, and **Poly-2@GC** were 4908, 2000, and 190.8 Ω respectively (Table 3). R_{CT} of **Poly-2@GC** was reduced to 3.8% of bare GC and 9.6% of **3@GC**. These results clearly demonstrate that charge transfer ability is largely enhanced due to the biscarbazole moieties embedded in **Poly-2**.

Table 3. Fitting results of electrochemical impedance spectrometry for different working electrodes. R_{CT} : charge transfer resistance, R_{ele} : electrolyte resistance, Q : constant phase element (CPE) value, α : CPE index.

	GC only	3	Poly-2@GC
R_{CT} (Ω)	4908	2000	190.8
R_{ele} (Ω)	29.62	76.37	27.85
Q (μ F)	55.89	140.1	358.4
α	0.8446	0.798	0.8115

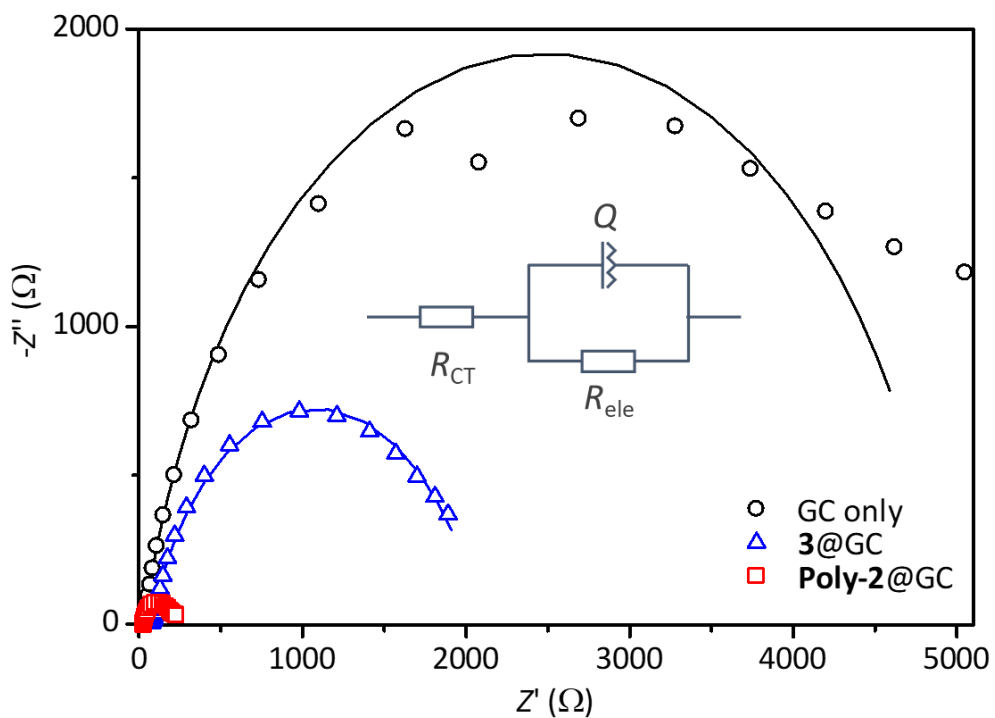


Figure 9. Nyquist plots of a bare GC (black), **3@GC** (blue) and **Poly-2@GC** (red). Measurements were performed in 0.2 M phosphate buffer (pH = 7.06) under an argon atmosphere. (Inset) the equivalent circuit for fitting data. Applied potential: 1.30 V vs. Ag/AgCl, measurement range: 0.1 Hz - 100 kHz. 20 nmol of **3** was mounted by drop-cast method to prepare **3@GC**.

Catalytic activity

To investigate the catalytic activity, **Poly-2** was immobilized on a glassy carbon electrode. Figure 10 shows the cyclic voltammograms of **Poly-2@GC** in a phosphate buffer solution (pH = 7.0). **Poly-2@GC** showed a slight increase of current corresponding water oxidation reaction, besides **3@GC** showed a smaller current increase than that of **Poly-2@GC**. Linear sweep voltammetry was also measured at the scan rate of 5 mV s^{-1} (Figure 11). The catalytic current was obviously observed above $\sim 1.2 \text{ V}$ (vs. Ag/AgCl) which demonstrated the catalytic activity of **Poly-2**. The onset potential and overpotential (η) were estimated to be 1.163 V and 346 mV , respectively. Figure 12 shows SWV result of **Poly-2**. Each regions separated by the peaks in SWV could be assigned Ru^{II} , Ru^{III} , Ru^{IV} , and Ru^{V} as the potential increased.[7]

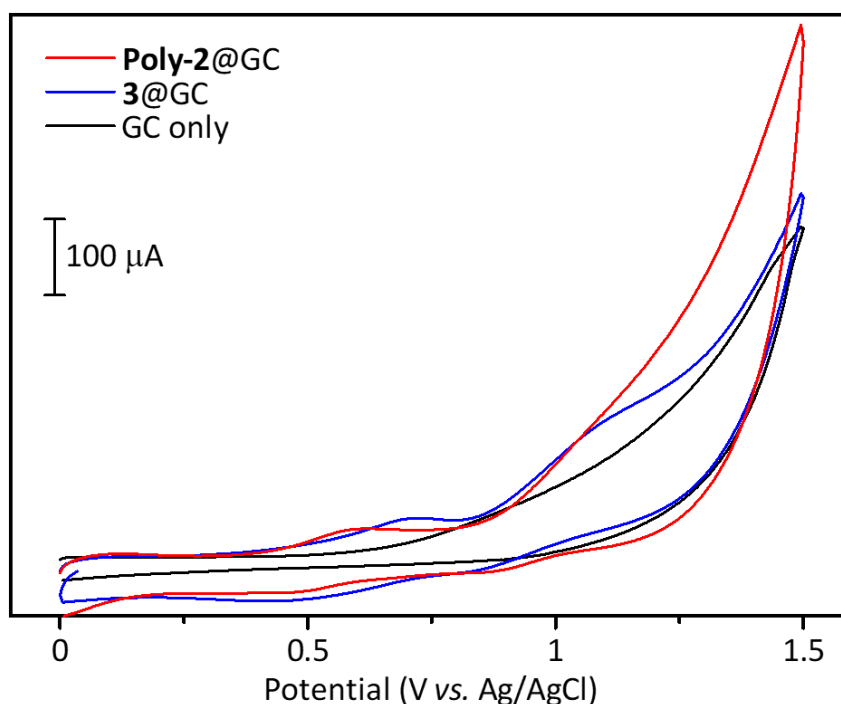


Figure 10. Cyclic voltammograms of a **Poly-2@GC** (red line) and a bare GC (black dashed line) electrode in phosphate buffer solutions (pH = 7.0). Measurements were performed under Ar at a scan rate of 100 mV s^{-1} .

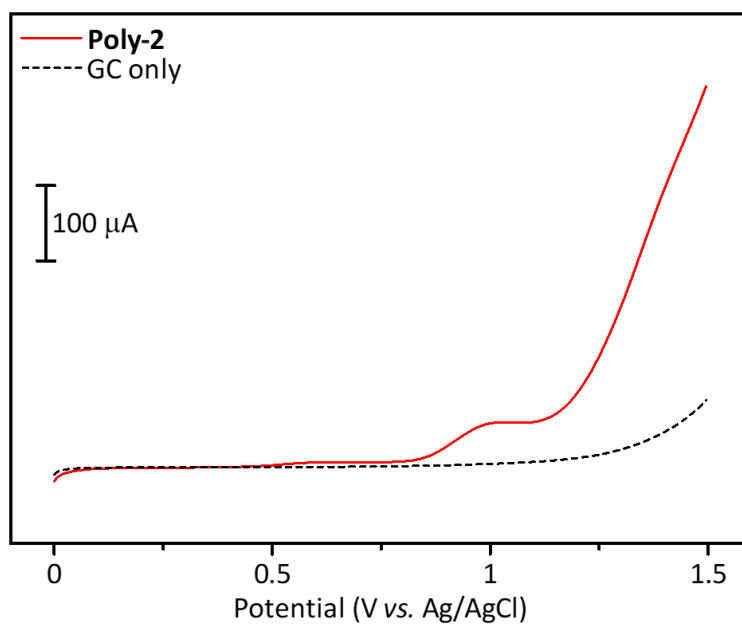


Figure 11. Linear sweep voltammograms of a **Poly-2@GC** (red line) and a bare GC (black dashed line) electrode in phosphate buffer solutions (pH = 7.0). Measurements were performed under Ar at a scan rate of 5 mV s^{-1} .

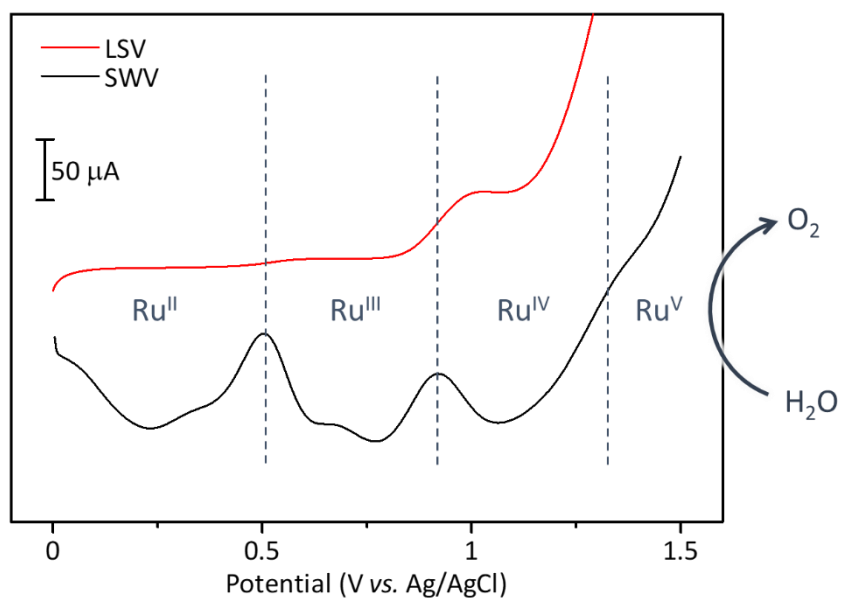


Figure 12. Linear sweep voltammogram (red line) and square wave voltammogram (black line) of a **Poly-2@GC** electrode in phosphate buffer solutions (pH = 7.0). Measurements were performed under Ar at a scan rate of 5 mV s^{-1} for LSV and 60 mV s^{-1} for SWV.

Finally, controlled potential electrolysis was performed to evaluate the catalytic ability of **Poly-2**. After 1 h of electrolysis of **Poly-2@GC** at 1.30 V (vs. Ag/AgCl), 1.28 C of charge was passed, and 3.01 μmol of O_2 as the major product was detected by gas chromatography (Figure 13 and Table 4). The maximum Faradaic efficiency of the reaction based on the $4e^-$ process was estimated to be 90.1%. These results demonstrate that **Poly-2** can promote electrocatalytic water oxidation. Moreover, the catalytic activity is almost suppressed under the identical experimental conditions when the electrode modified with the complex without biscarbazole moieties, **3@GC**, was used (Figure 13, blue line). The result together with the EIS behaviors strongly suggested that the combination of biscarbazole moieties as charge transporters with reaction centers is essential to achieve efficient catalysis. These properties are identical to that of **Poly-1** described in chapter 1. Therefore, it is successfully confirmed that the integration of charge transporting units close to the catalytic center is potentially applicable to various metal complex catalysts.

Table 4. The amounts of evolved O_2 , charge and Faradaic efficiencies over 1 h of controlled potential electrolysis of **Poly-2@GC**.

Potential (V vs. Ag/AgCl)	O_2 (μmol)	Faradaic Efficiency (%)
1.30	3.01	90.1
1.35	2.60	70.8
1.40	3.89	68.1

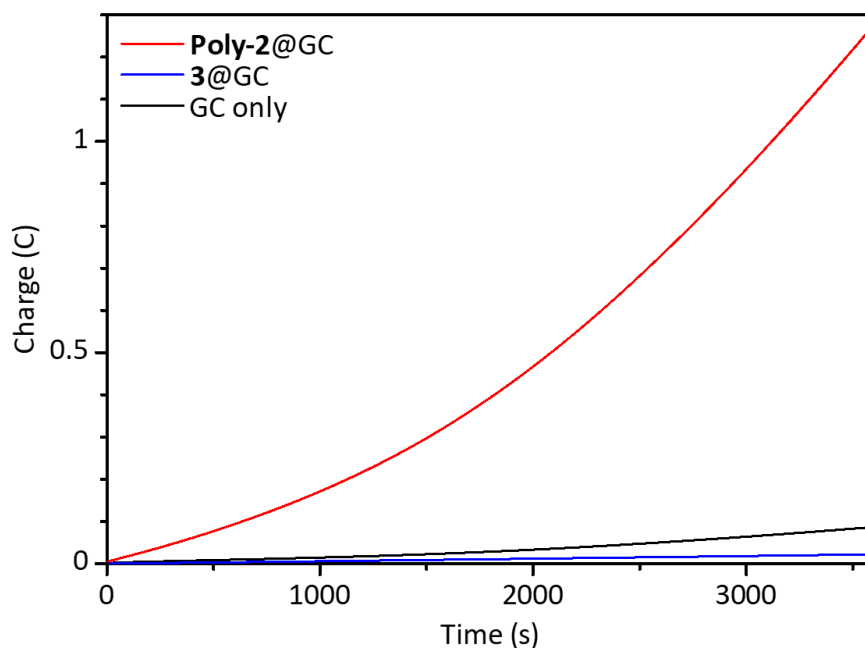


Figure 13. Controlled potential electrolysis data of **Poly-2@GC** (red line), **3@GC** (blue line) and a bare GC (black line) in phosphate buffer solutions (pH = 7.0) under an argon atmosphere. Applied potential: 1.30 V vs. Ag/AgCl.

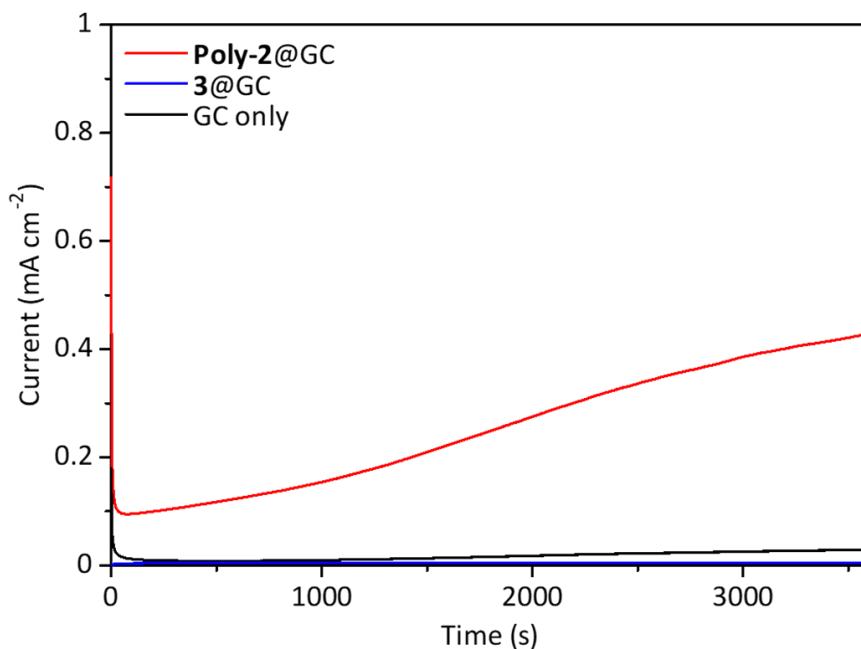


Figure 14. *I-t* curves of **Poly-2@GC** (red line), **3@GC** (blue line), and a bare GC electrode (black line) during 1 h of electrolysis at 1.30 V vs. Ag/AgCl.

Conclusion

In conclusion, the function-integrated electrocatalytic system for water oxidation was successfully constructed by electrochemical polymerization of complex **2**. Electrochemical impedance spectra and controlled potential electrolysis results were clearly suggested that biscarbazole moiety was necessary for efficient water oxidation. This is a second example that exhibits catalytic performance was enhanced by the introduction of charge transporting materials close to the catalytic center. I demonstrated the potential application of the function-integrated catalyst system for a variety of metal complexes.

Experimental section

Materials

All reagents were purchased from Tokyo Chemical Industry Co., Ltd., FUJIFILM Wako Pure Chemical Co., Kanto Chemical Co. Inc. and used without further purification. Ru(dmsO)₄Cl₂ and 5-phenylisoquinoline (iqPh) were synthesized according to reported procedures.[10,11]

Measurement apparatus

¹H NMR spectra were acquired on a JEOL JNM-LA400 spectrometer, where chemical shifts in CD₃CN and CDCl₃ were referenced to internal tetramethylsilane. Elemental analyses were carried out on a J-SCIENCE LAB MICRO CORDER JM10 elemental analyser. UV-Vis absorption spectra were recorded on a Shimadzu UV-3600 UV-Vis-NIR spectrophotometer. FT-IR spectra were measured on a Perkin Elmer Spectrum 100 spectrometer by attenuated total reflection method. SEM-EDX spectra were recorded a Hitachi high-technologies SU-6600 and a BrukerAXS XFlash5060FQ (5 kV acceleration voltage). Gas analysis for O₂ was performed using a Shimadzu GC-2014 gas chromatograph equipped with a thermal conductivity detector (TCD) and fitted with a molecular sieve 5A column (Ar carrier gas).

X-ray crystal structure analysis

Single crystal X-ray diffraction data were collected on a HyPix-6000 diffractometer equipped with confocal monochromated Mo-K α radiation ($\lambda = 0.71069 \text{ \AA}$) coated with Paratone-N (Hampton Research Corp., Aliso Viejo, CA, USA). Data was processed using CrysAlisPro system software.[12] The structure was solved by dual-space algorithm using SHELXT program[13] through the Olex2 interface.[14] All non-hydrogen atoms were refined anisotropically using a least-squares method, and hydrogen atoms were fixed at calculated positions and refined using a riding model. SHELXL-2014/7 was used for structure refinement.[15] Full-matrix least-squares refinements on F^2 based on unique reflections with unweighted and weighted agreement factors of $R = \Sigma||F_o| - |F_c||/\Sigma|F_o|$ ($I > 2.00 \sigma(I)$) and $wR = [\Sigma w(F_o^2 - F_c^2)^2/\Sigma w(F_o^2)^2]^{1/2}$ were performed. Mercury 4.0.0 was used for visualization and analysis of the structure.

Electrochemistry

All measurements were conducted at 20 °C, under Ar atmosphere. A standard three-electrode configuration was employed in conjunction with a CH Instruments potentiostat interfaced to a computer with CH Instruments 650 DKMP software. A platinum auxiliary electrode and leakless Ag/AgCl reference electrode were used if there is not mentioned. The redox potentials were calibrated against the redox potential for the ferrocene/ferrocenium (Fc/Fc⁺) couple in organic solvents.

Electrochemical impedance spectroscopy

The **poly-2** and **3** modified GC plate was used as a working electrode. 0.2 M Na₂HPO₃ buffer solution (pH = 7) was bubbled with Ar for 10 min before measurements. Electrochemical impedance spectra were recorded on bias potential at 1.30 V vs. Ag/AgCl and 0.1 Hz -100 kHz measurement range. Recorded data were fitted with the equivalent circuit shown in Fig. 9.

Cyclic voltammetry

Cyclic voltammetry was performed using a GC disk (diameter 3 mm, from BAS Inc.) and plate (30 × 7 × 2 mm³) working electrode. The working electrode was polished with 0.05 μm alumina paste (from BAS Inc.) and washing with purified water before the measurements.

Controlled potential electrolysis

In an H-shaped two compartments cell, 0.2 M Na₂HPO₃ buffer solution (pH = 7) was bubbled with Ar for 10 min and electrolyzed for 1 h (potential was referred to Ag/AgCl (sat. KCl aq.)). After the electrolysis, gaseous phase was analysed by a gas chromatography (GC-2014, molecular sieve 5A column, Ar carrier gas) equipped with a thermal conductivity detector (TCD). The amount of O₂ was reported as subtracted value by considering air leakage.

Synthesis of 9-[2-(4-Pyridinyl)ethyl]carbazole (czpy)

Carbazole (1.67 g, 10.0 mmol) and K₂CO₃ (2.76 g, 20.0 mmol) were added to 10 mL of DMF. The mixture was stirred at room temperature to dissolve the solids. 1.05 mL (10.0 mmol) of 4-vinylpyridine was added to the mixture and heated at 110 °C overnight. The resulted solution was extracted with CH₂Cl₂ and washed with brine. The organic layer was concentrated, and white precipitates were filtered and washed with Et₂O. Target compound was obtained as a white crystalline solid (1.58 g, 57.9%) and used without further purification. ¹H NMR (δ, CDCl₃): 8.44 (d, J = 5.2 Hz, 2H), 8.09 (d, J = 8.4 Hz, 2H), 7.42 (m, 2H), 7.25 (m, 4H), 7.05 (d, J = 5.5 Hz, 2H), 4.56 (t, J = 7.3, 2H), 3.14 (t, J = 7.3, 2H).

Synthesis of Ru(bda)(czpy)₂ (2)

Ru(dmsO)₄Cl₂ (242 mg, 0.50 mmol) and 2,2'-bipyridine-6,6'-dicarboxylic acid (H₂bda, 122 mg, 0.50 mmol) was added to 10 mL of MeOH containing 0.4 mL of Et₃N. The mixture was degassed by bubbling N₂ gas for 10 min and refluxed for 30 min under N₂ atmosphere. The color was changed yellow to deep red. Then czpy (272 mg, 0.50 mmol) was added to the mixture and refluxed overnight. The resulted solution was cooled to room temperature and filtered to collect precipitates. The obtained solid was purified with column chromatography over neutral alumina (CHCl₃: MeOH 95:5). The deep red fraction was collected to afford the target complex. Obtained solid was dispersed in MeCN then MeOH was added until the solution became clear. Vapor diffusion of ^tBuOMe into the solution afforded reddish brown crystals (149.2 mg, 33.6%). ¹H NMR (δ, CD₃CN): 8.11 (d, J = 7.6, 8H), 7.72 (s, 8H), 7.43 (m, 8H), 7.33 (m, 12H), 7.20 (m, 8H), 6.64 (m, 8H), 4.59 (m, 8H), 3.01 (m, 8H). Elemental analysis calcd for Ru(bda)(czpy)₂: C 67.63, H 4.31, N 9.46; found: C 67.28, H 4.39, N 9.65. MALDI-MS: [M]⁺ calcd.: 888.20, found: 888.20.

Synthesis of Ru(bda)(iqPh)₂ (3)

Ru(bda)(iqPh)₂ was synthesized by the same procedure as **1** with iqPh instead of czpy. Single crystal suitable for X-ray diffraction measurement was grown by vapor diffusion of ^tBuOMe into the CHCl₃ solution afforded reddish brown crystals (83.1 mg, 22.0%). ¹H NMR (δ, DMSO-*d*₆): δ 8.82 (s, 2H), 8.76 (d, J = 5.0 Hz, 2H), 8.10 (d, J = 7.8 Hz, 2H), 7.90 (t, J = 6.6 Hz, 4H), 7.70-7.77 (m, 4H), 7.47 (q, J = 7.2 Hz, 8H), 7.41 (t, J = 7.3 Hz, 6H). MALDI-MS: [M]⁺ calcd.: 754.12, found: 754.10.

Preparation of Poly-2@GC

The **poly-2** modified GC plate was made by cyclic voltammetry technique (0-1.5 V vs. Ag/AgCl, 10 cycles).

Preparation of 3@GC

Complex **3** was mounted on a GC plate by the drop-cast method: 40 μL of 0.5 mM solution of **3** was dropped on a GC plate and dried *in vacuo*.

References

- [1] (a) X. Liu, F. Wang, *Coord. Chem. Rev.* **2012**, *256*, 1115–1136. (b) A. Singh, L. Spiccia, *Coord. Chem. Rev.* **2013**, *257*, 2607–2622. (c) M. D. Kärkäs, O. Verho, E. V. Johnston, B. Åkermark, *Chem. Rev.* **2014**, *114* (24), 11863–12001. (d) J. D. Blakemore, R. H. Crabtree, G. W. Brudvig, *Chem. Rev.* **2015**, *115*, 12974–13005. (e) M. Kondo, S. Masaoka, *Chem. Lett.* **2016**, *45* (11), 1220–1231. (f) B. Zhang, L. Sun, *Chem. Soc. Rev.* **2019**, *48*, 2216–2264. (g) S. Ye, C. Ding, M. Liu, A. Wang, Q. Huang, C. Li, *Adv. Mater.* **2019**, *31*, 1902069.
- [2] (a) A. J. Bard, M. A. Fox, *Acc. Chem. Res.* **1995**, *28* (3), 141–145. (b) E. Amouyal, *Sol. Energy Mater. Sol. Cells* **1995**, *38*, 249–276.
- [3] L. Duan, F. Bozoglian, S. Mandal, B. Stewart, T. Privalov, A. Llobet, L. Sun, *Nat. Chem.* **2012**, *4*, 418–423.
- [4] (a) L. Duan, A. Fischer, Y. Xu, L. Sun, *J. Am. Chem. Soc.* **2009**, *131* (30), 10397–10399. (b) J. Nyhlén, L. Duan, B. Åkermark, L. Sun, T. Privalov, *Angew. Chem. Int. Ed.* **2010**, *49* (10), 1773–1777.
- [5] K. Karon, M. Lapkowski, *J. Solid State Electrochem.* **2015**, *19* (9), 2601–2610.
- [6] L. Kortekaas, F. Lancia, J. D. Steen, W. R. Browne, *J. Phys. Chem. C* **2017**, *121* (27), 14688–14702.
- [7] L. Duan, F. Bozoglian, S. Mandal, B. Stewart, T. Privalov, A. Llobet, L. Sun, *Nat. Chem.* **2012**, *4* (5), 418–423.
- [8] S. H. Hsiao, S. W. Lin, *Polym. Chem.* **2016**, *7* (1), 198–211.
- [9] Y. Chen, Y. Zhang, L. Zhao, *Phys. Chem. Chem. Phys.* **2003**, *6* (3), 537–542.
- [10] E. Alessio, *Chem. Rev.* **2004**, *104* (9), 4203–4242.
- [11] D. V. Horváth, F. Domonyi, R. Palkó, A. Lomoschitz, T. Soós, *Synth.* **2018**, *50* (33), 2181–2190.
- [12] CrysAlisPro, Oxford Diffraction Ltd., Version 1.171.39.46.
- [13] G. M. Sheldrick, *Acta Cryst.* **2015**, *A71*, 3–8.
- [14] O. V. Dolomanov, L. J. Bourhis, R. J. Gildea, J. A. K. Howard and H. Puschmann, *J. Appl. Crystallogr.* **2009**, *42*, 339–341.
- [15] G.M Sheldrick., *Acta Cryst.* **2015**, *C71*, 3–8.

Chapter 3

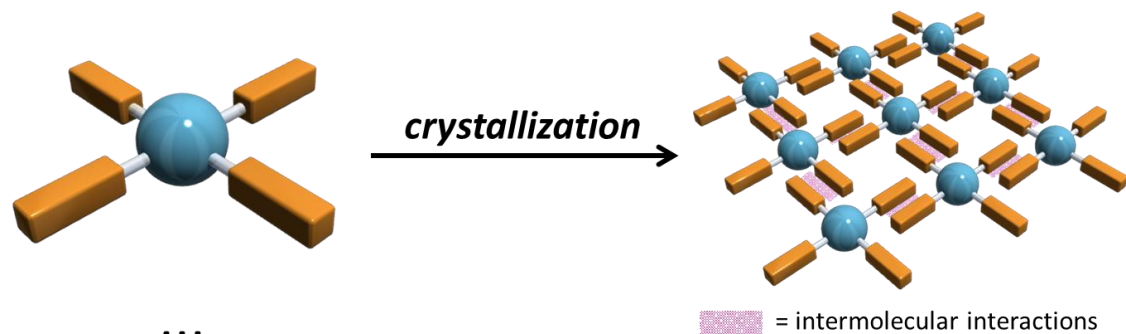
Construction of Self-Assembled Frameworks of Cubane-Type Tetranuclear Cobalt Complexes

Introduction

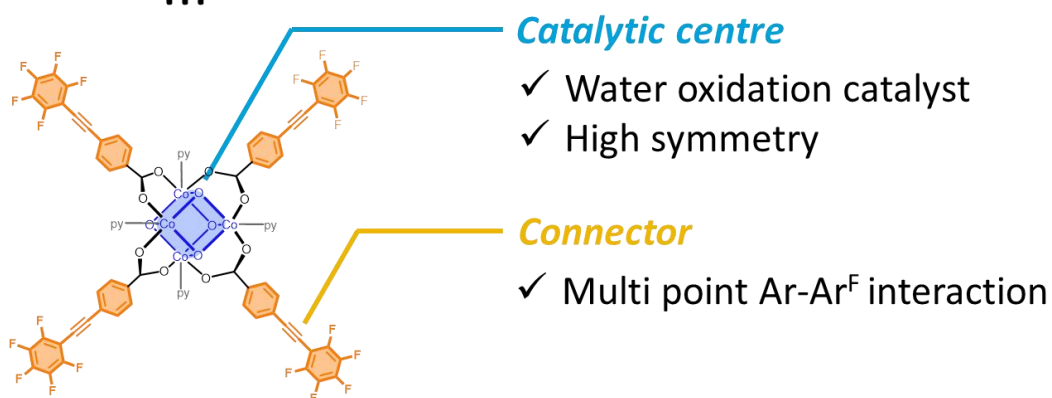
Four-electron oxidation of water ($2\text{H}_2\text{O} \rightarrow \text{O}_2 + 4\text{H}^+ + 4\text{e}^-$) provides protons and electrons that are necessary for the production of reduced chemical energy (e.g. H_2 , CH_3OH).^[1] Although the reaction is valuable, it requires high energy to overcome the activation barrier.^[2] In nature, water oxidation reaction is catalyzed by manganese-oxo cluster complex known as oxygen evolving complex (OEC) in photosystem II (PS II).^[3] OEC is located at the node of water channels that supply water and release oxygen.^[4] In this context, it could be effective for water oxidation reaction to construct porous catalyst.

Metal-organic frameworks (MOFs) have porous structures derived from coordination bond networks.^[5] Therefore, catalytic applications of MOFs have been interested and reported including water oxidation.^[6] Nevertheless, the introduction of catalytic centers into MOFs is still challenging.

In this chapter, I focused on a supramolecular approach to construct porous materials with well-defined catalytic centers. Discrete molecular modules composed of catalytic center and intermolecular interaction sites can be assembled into framework structures.^[7] My approach achieved ordered catalytic centers and controllable assembled structures. In this study, new molecular modules for a framework catalyst were designed and synthesized. Additionally, framework structure can be controlled over the number of substituted ligands. The catalytic activity of the obtained framework was also investigated.



III



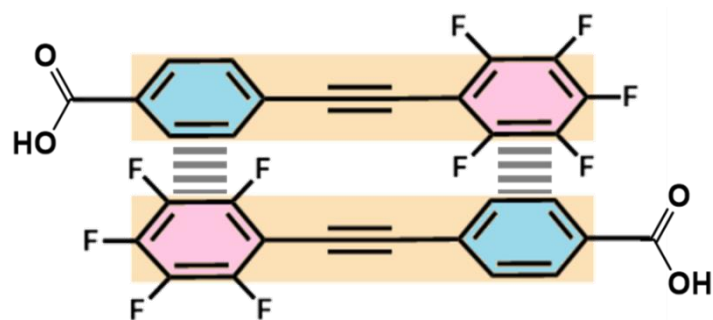
Scheme 1. (Top) Schematic illustration of molecular-based framework catalyst. (Bottom) Structure of molecular module in this study.

Results and discussions

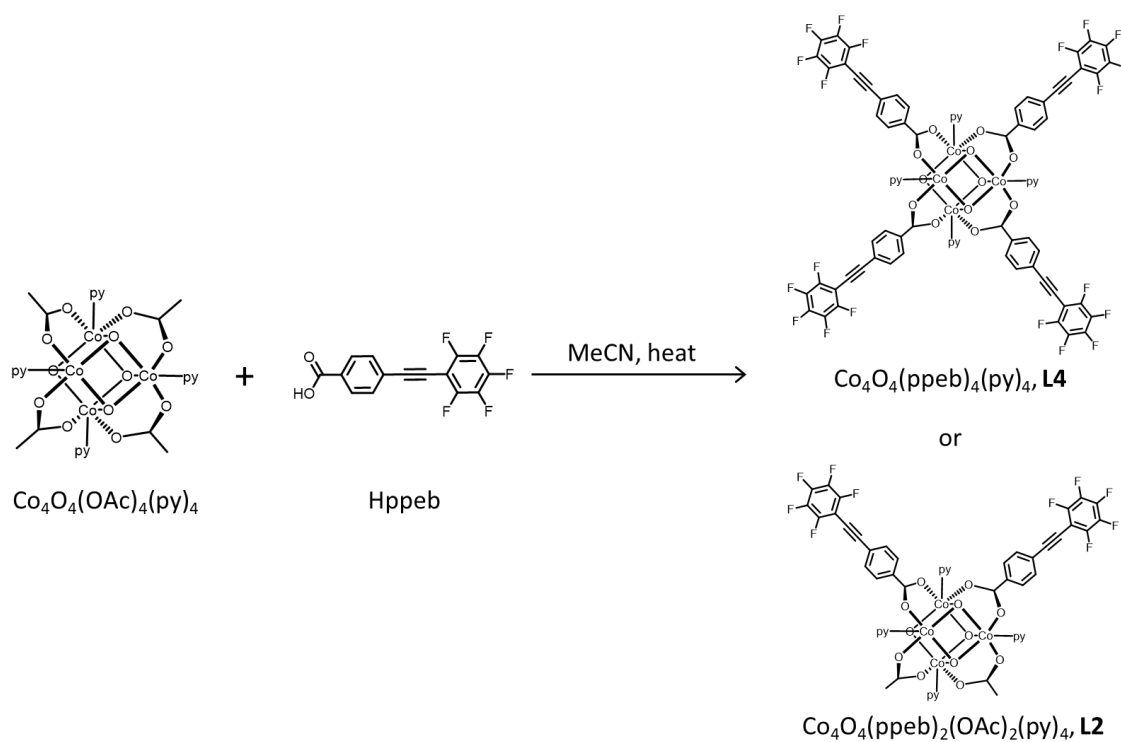
The design of the catalyst module is shown in Scheme 1. The catalytic centre is a cubane-shaped Co complex, $\text{Co}_4\text{O}_4(\text{OAc})_4(\text{py})_4$ (OAc : acetate anion, py: pyridine), which is known as a water oxidation catalyst.[8] Pseudo-4-fold symmetry at acetate ligands in $\text{Co}_4\text{O}_4(\text{OAc})_4(\text{py})_4$ complex makes molecular modules suitable for assembly. The acetate ligand was substituted into 4-[(perfluorophenyl)ethynyl]-benzoic acid (Hppeb) which is reported to form a supramolecular framework through multi-point arene-perfluoroarene ($\text{Ar}-\text{Ar}^{\text{F}}$) interactions (Scheme 2).[7a-b,9]

Synthesis of the molecular modules

Synthesis of molecular modules was conducted following scheme 3. Firstly, 4-[(perfluorophenyl)ethynyl]-benzoic acid (Hppeb) and $\text{Co}_4\text{O}_4(\text{OAc})_4(\text{py})_4$ complex were synthesized according to reported procedures.[7a,10,11] Tetra-substituted complex, $\text{Co}_4\text{O}_4(\text{ppeb})_4(\text{py})_4$ (**L4**) was synthesized by ligand exchange reaction of $\text{Co}_4\text{O}_4(\text{OAc})_4(\text{py})_4$ and Hppeb in MeCN at 80 °C overnight. Purification over silica gel afforded dark green solid in 6.89% yield. **L4** was characterized by single crystal X-ray diffraction (XRD) and powder XRD measurement. To promote ligand exchange reaction, an alternative procedure was examined: to remove released acetic acid, azeotropic distillation with toluene was carried out after heating at 80 °C for 2 h. This heating and azeotropic distillation process was repeated to complete the reaction. As a result, **L4** was obtained in 27.5% yield after the purification. Di-substituted complex, $\text{Co}_4\text{O}_4(\text{ppeb})_2(\text{OAc})_2(\text{py})_4$ (**L2**) was synthesized by heating the reaction mixture containing $\text{Co}_4\text{O}_4(\text{OAc})_4(\text{py})_4$ and Hppeb at 60 °C overnight. The crude product was purified over silica gel chromatography. **L2** was also characterized by single crystal XRD and powder XRD analysis.



Scheme 2. Multi-point arene-perfluoroarene (Ar-Ar^F) interaction of Hppeb ligand.



Scheme 3. Synthetic scheme of **L4** and **L2**.

Single crystal X-ray diffraction analysis

Single crystals of **L4** were obtained by vapor diffusion of pentane into CHCl_3 solution of **L4** at room temperature. An ORTEP drawing of **L4** is shown in Figure 1a. All acetate ligands of $\text{Co}_4\text{O}_4(\text{OAc})_4(\text{py})_4$ were substituted for ppeb^- ligands. **L4** crystalized in $P2_1/c$ with the large void space which may contain solvent molecules. Because of the large void space (summarized in Table 3), solvent molecules could not be assigned, and SQUEEZE treatment was applied for the refinement. The distances between Co ions and bridging oxygen atoms were 1.848-1.871 Å, which were comparable to the reported values.[11]

From the alternative synthesis procedure, **L4** formed only different crystal packing (**L4'**). **L4'** crystalized in $P2_1/n$ and three CHCl_3 molecules were taken in the unit cell as a crystal solvent. The difference from the structure of **L4** was the ppeb ligands that were bent to shrink along b axis.

Single crystals of **L2** suitable for X-ray diffraction measurement were obtained by layering hexane on CH_2Cl_2 solution of **L2**. Two acetate ligands at *cis* position were exchanged. Relevant di-substituted $\text{Co}_4\text{O}_4(\text{OAc})_4(\text{py})_4$ complex was previously reported [12] and *cis* form of **L2** agreed with the previously reported complex. **L2** crystalized in $I2/a$ with the large void space which may contain solvent molecules. Because of the large void space (detailed discussing latter), solvent molecules could not be assigned, and SQUEEZE treatment was applied for the refinement as performed in the structural analysis of **L4**.

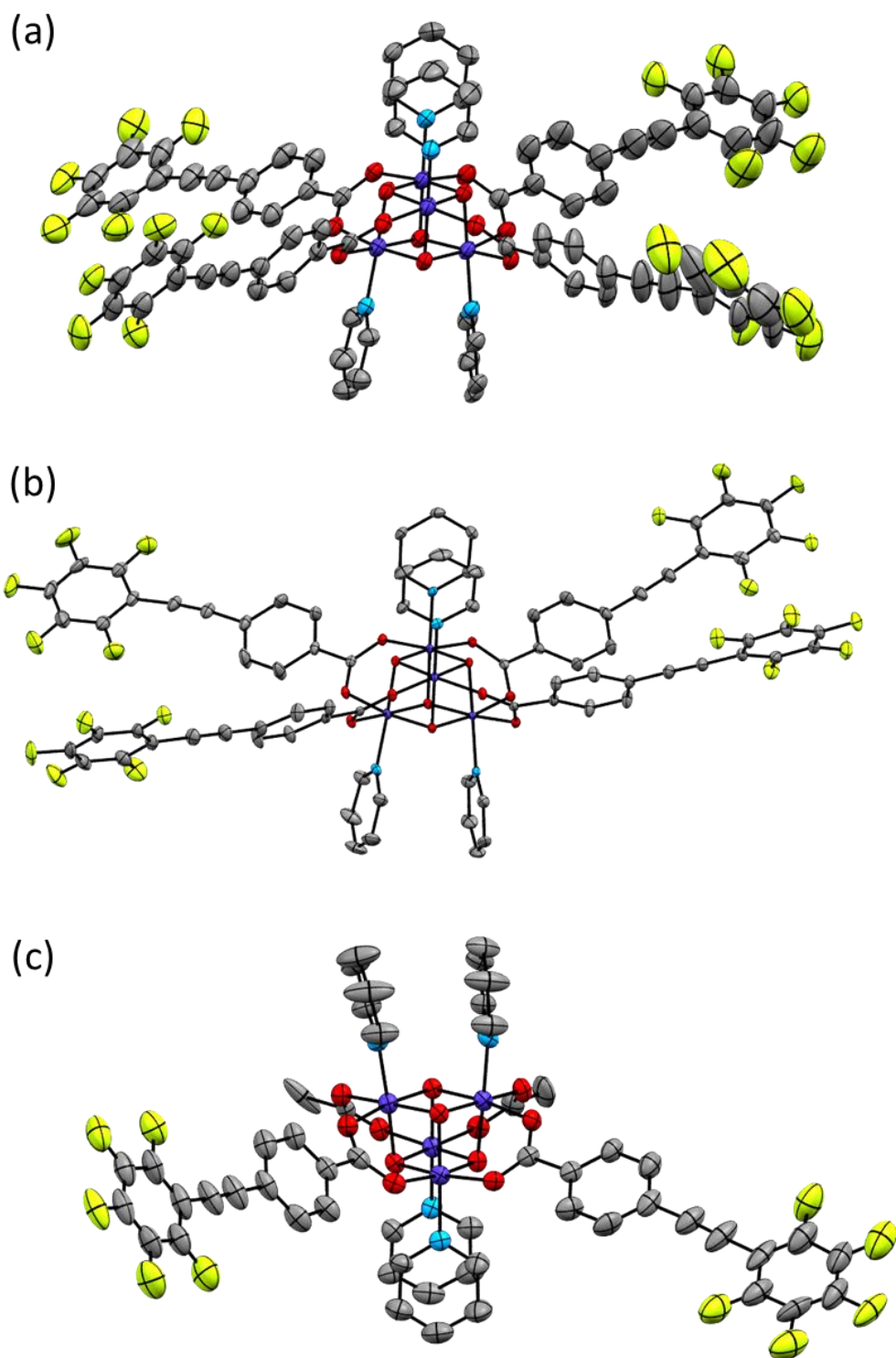


Figure 1. ORTEP drawings of (a) **L4**, (b) **L4'** and (c) **L2**. Solvent molecules and hydrogen atoms are omitted for clarity. Thermal ellipsoids are shown at the 50% for **L4'** and 30% probability level for **L4** and **L2**. Color chart: purple: Co, grey: C, cyan: N, red: O, yellow: F.

Table 1. Crystallographic data of **L4**, **L4'**, and **L2** (*squeezed data).

Compound	Co ₄ O ₄ (ppeb) ₄ (py) ₄ (L4)	Co ₄ O ₄ (ppeb) ₄ (py) ₄ ·3CHCl ₃ (L4')	Co ₄ O ₄ (ppeb) ₂ (OAc) ₂ (py) ₄ (L2)
Formula	C ₈₀ H ₃₆ Co ₄ F ₂₀ N ₄ O ₁₂	C ₈₀ H ₃₆ Co ₄ F ₂₀ N ₄ O ₁₂ (C ₃ H ₃ Cl ₉)	C ₅₄ H ₃₄ Co ₄ F ₁₀ N ₄ O ₁₂
Crystal system	monoclinic	monoclinic	monoclinic
Space group	<i>P2₁/c</i>	<i>P2₁/n</i>	<i>I2/a</i>
<i>a</i> / Å	23.3439(5)	15.1832(3)	19.3867(4)
<i>b</i> / Å	30.1856(6)	32.4695(6)	30.1658(9)
<i>c</i> / Å	19.3958(3)	18.0525(4)	40.8090(10)
<i>β</i> / °	103.201(2)	105.915(2)	95.113(2)
<i>V</i> / Å ³	13306.1	8558.59	23770.8(10)
<i>Z</i>	4	4	8
<i>R</i> ₁	0.1129 (0.0692*)	0.0524 (0.0445*)	0.1268 (0.0743*)
<i>wR</i> ₂	0.3934 (0.2344*)	0.1342 (0.1012*)	0.3660 (0.2166*)
GooF	1.055 (0.900*)	1.068 (1.097*)	1.918 (0.900*)

Table 2. Selected bond lengths of $\text{Co}_4\text{O}_4(\text{OAc})_4(\text{py})_4$, **L4**, **L4'**, and **L2**.

	$\text{Co}_4\text{O}_4(\text{OAc})_4(\text{py})_4$	L4	L4'	L2
C-O _{oxo}	1.860-1.876	1.848-1.871	1.858-1.872	1.852-1.872
Co-O _{COOH}	1.948-1.962	1.950-1.968	1.930-1.977	1.945-1.959
Co-N	1.96	1.948-1.957	1.950-1.970	1.939-1.959

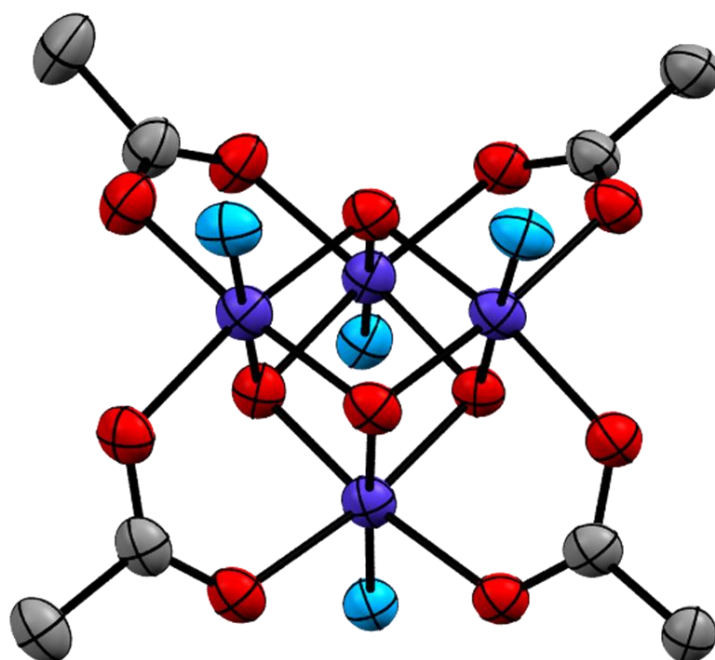


Figure 2. The structure of cubane-type core in **L4**. Color chart: purple: Co, grey: C, cyan: N, red: O.

Comparisons of packing structures

The crystal packing of **L4** (**FL4**) is shown in Figure 3a. **FL4** has infinite nanopores along the *c* axis and the aperture was diamond shape $9.46 \times 12.7 \text{ \AA}^2$. The void space of **FL4** was estimated to be 52.4% by SQUEEZE treatment. **L4** molecules formed a 2D sheet on the *ab* plane and layering the sheets led to the framework structure (Figure 3b). Two kinds of ppeb ligands (A and B in Figure 4a) were stacked in order of ABBA or BAAB through Ar-Ar^F and π - π interactions (Figure 4b). In the case of ligands A and B, four ligands were stacked in one group everywhere in **FL4**. The distances between ligand A and B were 3.307-3.373 \AA that are comparable to reported π - π interactions. The ligand D had Ar-Ar^F interactions with another ligand D in the next **L4** molecule (Figure 4c). Different from ligands A and B, D exists only a dimer form in **FL4**. In contrast, ligand C was the only ligand that had any interactions between other ligands. However, two ligand C may sandwich a pentane molecule which was used as a poor solvent (Figure 4d) because several residual peaks were observed that could not be assigned due to the disorder.

Table 3. Summary of SQUEEZE treatment.

	L4	L4'	L2
Void space (\AA^3)	6978	1829	14574
Void space (% _{unit cell})	52.44	21.37	61.31
Electron counts	1334	704	2357

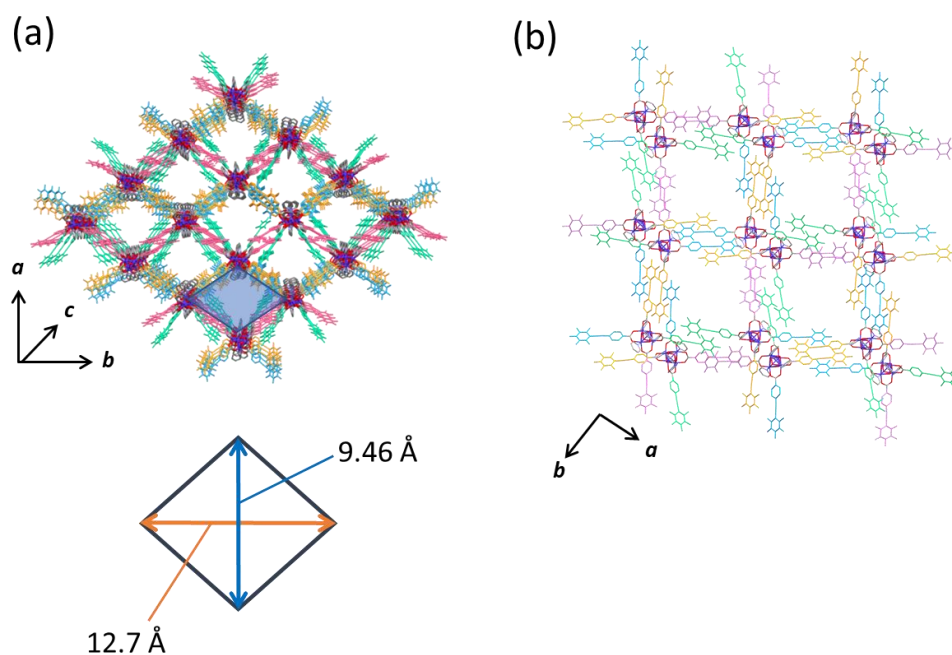


Figure 3. (a) Packing structure of and the diagram of aperture of **L4 (FL4)**. (b) 2D sheet structure in **FL4**.

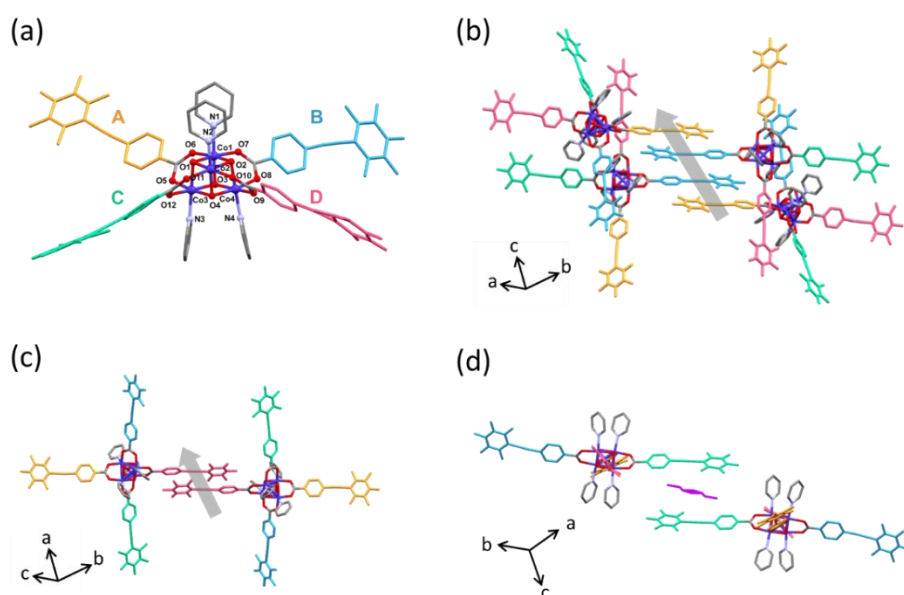


Figure 4. (a) Crystallographically independent four ppeb ligands in **L4** distinguished by different colors; A: orange, B: blue, C: green, D: pink. (b) Ar-Ar^F interactions along *c* axis in **FL4**. (c) Ar-Ar^F interactions along *a* axis in **FL4**. (d) The residual solvent peaks between the ligand C. Magenta colored sticks represent residual Q peaks which was not included final refinement.

A framework structure derived from **L2** molecules (**FL2**) is shown in Figure 5. In a similar way to **FL4**, 2D sheets on *bc* plane composed of **L2** and the sheets were stacked to form a framework structure. **FL2** has infinite channels along *a* axis. The aperture was a hexagonal shape, and the distances of the longest diagonal line and width were 18.9 and 19.6 Å, respectively (Figure 5, bottom). The void volume of **L2** was estimated to be 61.3% by SQUEEZE. **FL2** has a larger void space than **FL4**, which is consistent with the pore sizes. As for the intermolecular interactions, both ppeb ligands (A and B in Figure 6a) were stacked in order of ABBA similarly to **L4**. The distances of Ar-Ar^F and π - π interactions shown in Figure 6b were 3.798 and 3.337-3.359 Å, respectively. In addition, the framework structure was also supported by CH-O interactions between pyridine rings and Co₄O₄-carboxylate core. The hydrogen atom of the 3-position of pyridine was located close to some oxygen atoms of the next **L2** molecules. The distances were 2.578 Å for CH-O_{oxo} and 2.471 Å for CH-O_{COOH}.

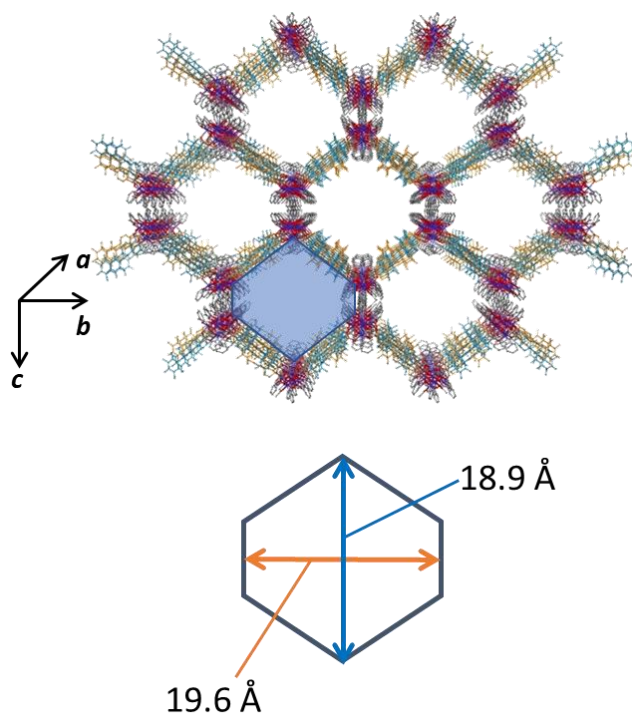


Figure 5. (top) Packing structure of **L2** (**FL2**). (bottom) The diagram of aperture of **FL2**.

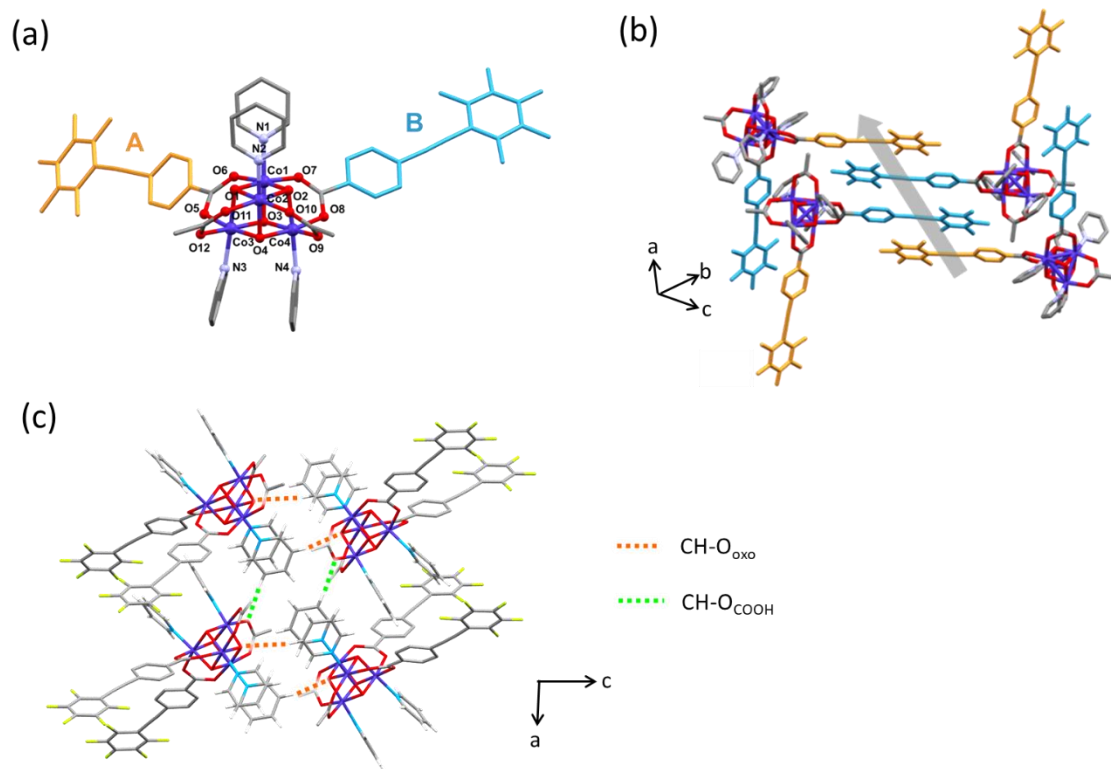


Figure 6. (a) Crystallographically independent four ppeb ligands in **L2** distinguished by different colors; A: orange, B: blue. (b) Ar-Ar^F interactions along *a* axis in **FL2**. (c) CH-O interactions between **L2** molecules. Orange dotted lines represent CH-O_{oxo} and green dotted lines represent CH-O_{COOH} interactions, respectively.

In the case of **L4'**, the packing structure was completely different from **FL4**. All ppeb ligands did not have multipoint Ar-Ar^F interaction, which led to the dense packing. The perfluorobenzene ring of ligand C and the benzene ring of ligand D in Figure 7 had face-to-face interaction. The distance of the ring centers was 3.729 Å, which was consistent with the reported Ar-Ar^F interaction. The void space was occupied with CHCl₃ and there was no aperture to release the crystal solvents.

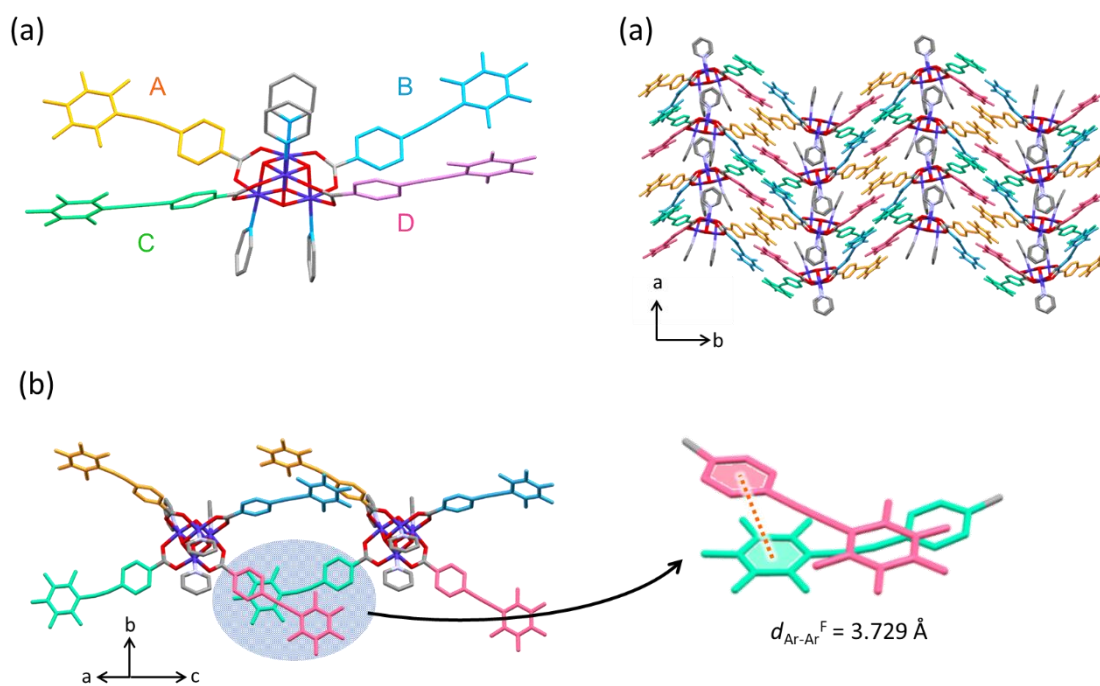


Figure 7. (a) Crystallographically independent four ppeb ligands in **L4** distinguished by different colors; A: orange, B: blue, C: green, D: pink. (b) Packing structure of **L4'**. (c) Ar-Ar^F interactions in **L4'** crystal.

Powder X-ray diffraction analysis

Prior to electrochemical measurements, powder X-ray diffraction (XRD) measurement was conducted to confirm crystal polymorphs. The recrystallized samples were triturated in pentane or 2-propanol, and sealed in a glass capillary with solvents to prevent the sample drying. Powder XRD patterns of **FL4** were shown in Figure 8. The peaks appeared slightly lower 2θ value than the simulated pattern, however, the data were almost agreed with simulation, and **FL4** maintained its crystallinity both in pentane and 2-propanol. The powder XRD pattern of **L4'** was also measured in pentane. **L4'** showed two intense peaks below $2\theta = 5^\circ$ which are different from that of **FL4** (Figure 9). These results suggested that **FL4** and **L4'** are completely different phases of **L4** molecule.

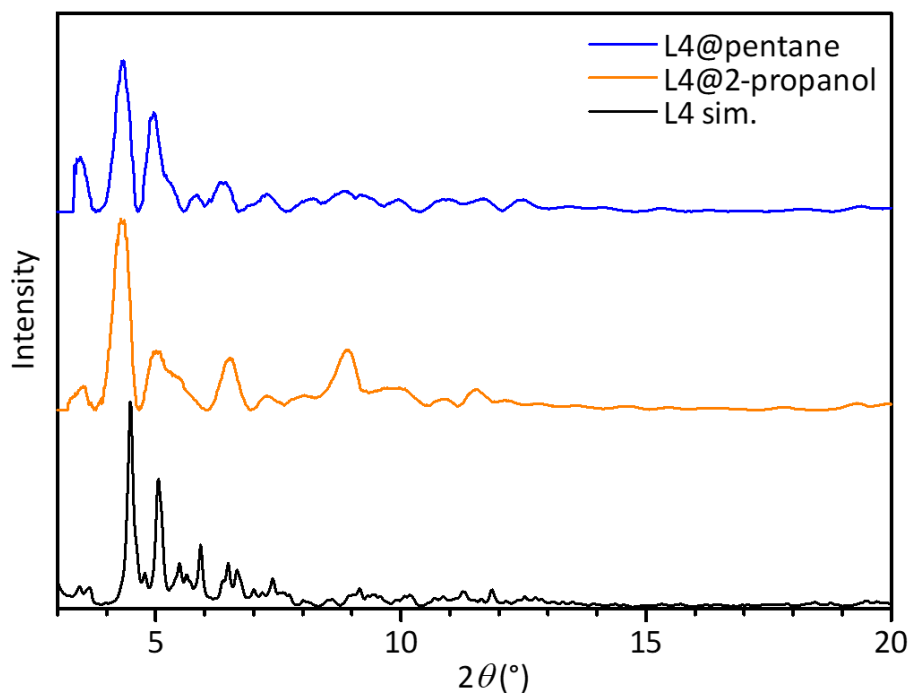


Figure 8. Powder X-ray diffraction patterns of **L4@pentane**, **L4@2-propanol**, and simulated pattern of **L4**, from top to bottom.

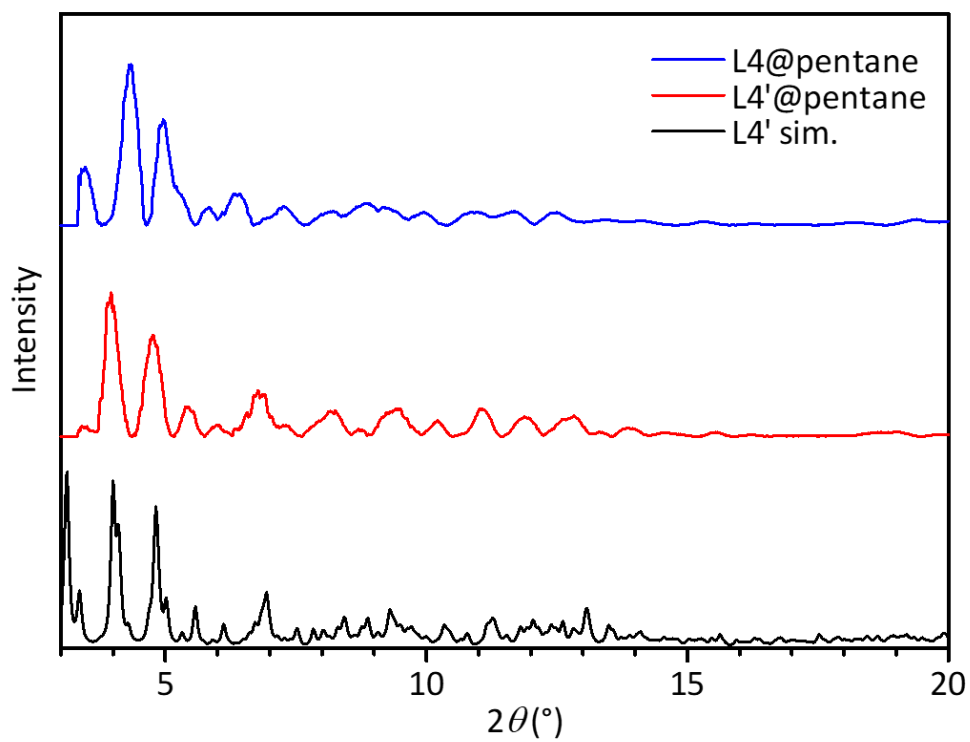


Figure 9. Powder X-ray diffraction patterns of **L4@pentane**, **L4'@pentane**, and simulated pattern of **L4'**, from top to bottom.

Electrochemistry

To elucidate the electrochemical properties of **L4**, cyclic voltammetry (CV) was measured in an organic medium (0.1 M tetra-*n*-butylammonium perchlorate (TBAP) in γ -butyrolactone). Resulted voltammogram was shown in Figure 10. One reversible oxidation peak was observed at 0.45 V (vs. Fc/Fc⁺), and this peak was assigned to the redox couple of Co center [Co^{IV}Co^{III}₃]⁵⁺/[Co^{III}₄]⁴⁺. [11] After adding water into the solution (10% of γ -butyrolactone, Figure 11), the oxidation wave of Co center was shifted 70 mV positive, which suggested a structural change of Co center. In addition, a large irreversible current was observed above 1.2 V, which indicated **L4** can catalyze water oxidation reaction electrochemically.

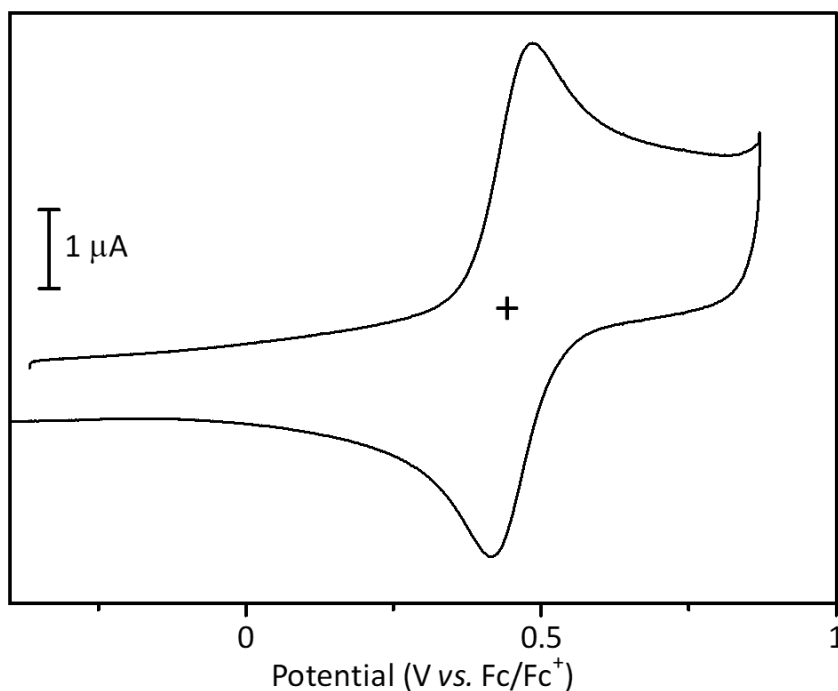


Figure 10. Cyclic voltammograms of a 0.5 mM solution of **L4**. Measurements were performed in a γ -butyrolactone solution containing 0.1 M TBAP under Ar at a scan rate of 100 mV s⁻¹. Working electrode, glassy carbon; counter electrode, Pt wire; reference electrode, Ag/Ag⁺. CV scans were initiated from the open-circuit potential.

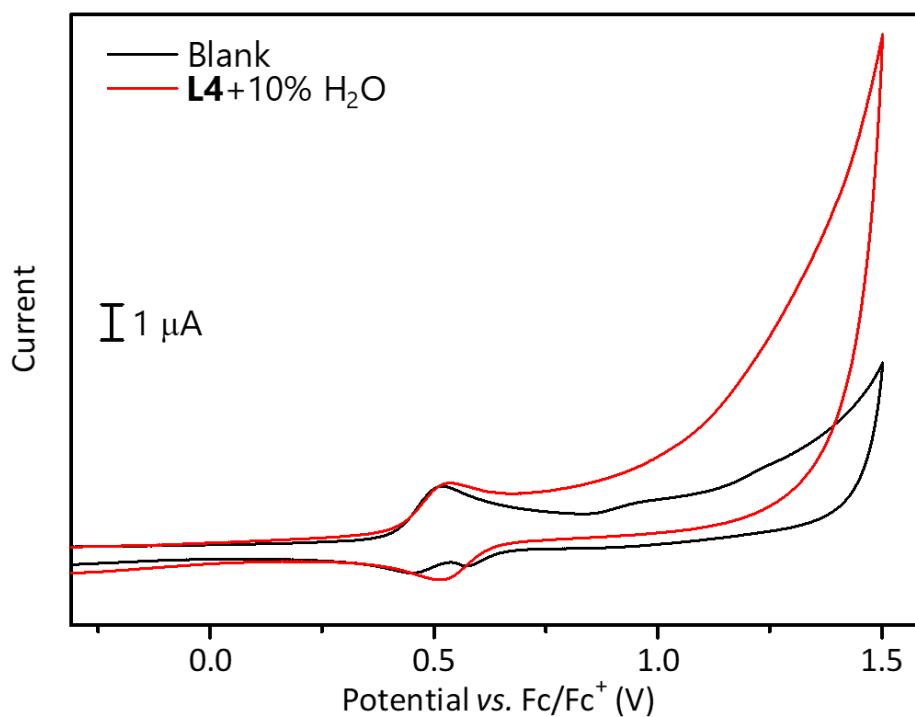


Figure 11. Cyclic voltammograms of a 0.5 mM solution of **L4** (a) without H₂O and (b) with 10% of H₂O. Measurements were performed in a γ -butyrolactone solution containing 0.1 M TBAP under Ar at a scan rate of 100 mV s⁻¹. Working electrode, glassy carbon; counter electrode, Pt wire; reference electrode, Ag/Ag⁺. CV scans were initiated from the open-circuit potential.

CV of the heterogeneous systems were also examined. **L4** modified electrode was made by drop cast method: 5 μL of 0.2 mM MeCN solution of **L4** was dropped on a glassy carbon electrode and dried in air. Figure 12 shows the result of CV under the heterogeneous conditions in phosphate buffer solution (pH = 7). The irreversible current increase was observed with **L4** modified electrode which showed **L4** can catalyze water oxidation at a neutral condition.

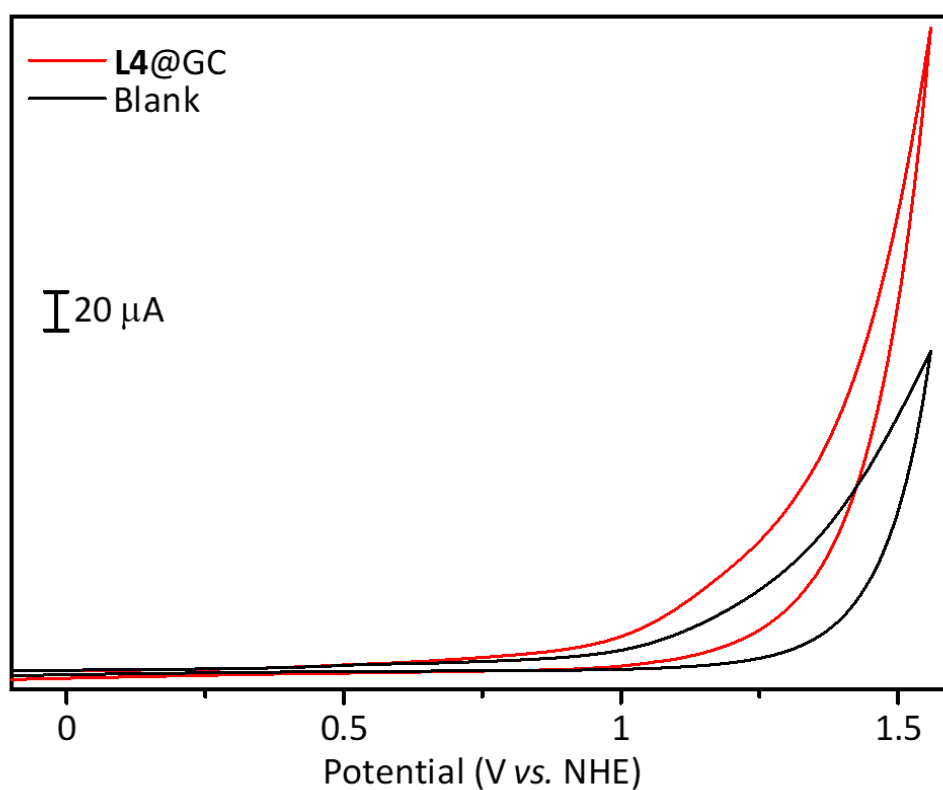


Figure 12. Cyclic voltammograms of **L4@GC** (red line) and blank (black line) in a 0.2 M phosphate buffer (pH 7). Measurements were performed under Ar at a scan rate of 100 mV s^{-1} . Working electrode, glassy carbon; counter electrode, Pt wire; reference electrode, SCE. CV scans were initiated from the open-circuit potential.

To evaluate the effect of the packing structure on catalytic activity, cyclic voltammetry of **FL4** and **L4'** were examined. Considering the porosity of **FL4**, the cavities of **FL4** were occupied with hydrophobic pentane, and it may affect the catalytic ability. Therefore, as-synthesized **FL4** was triturated in 2-propanol and mounted on the GC electrode. For the comparison, **L4'** was also measured in a crystalline state. As shown in Figure 13, the current was slightly increased when the GC electrode was modified with **FL4** crystal. In contrast, the catalytic current was not observed in the case of **L4'** which has less porosity. The data indicated that porous framework structure is key for the electrocatalytic reaction.

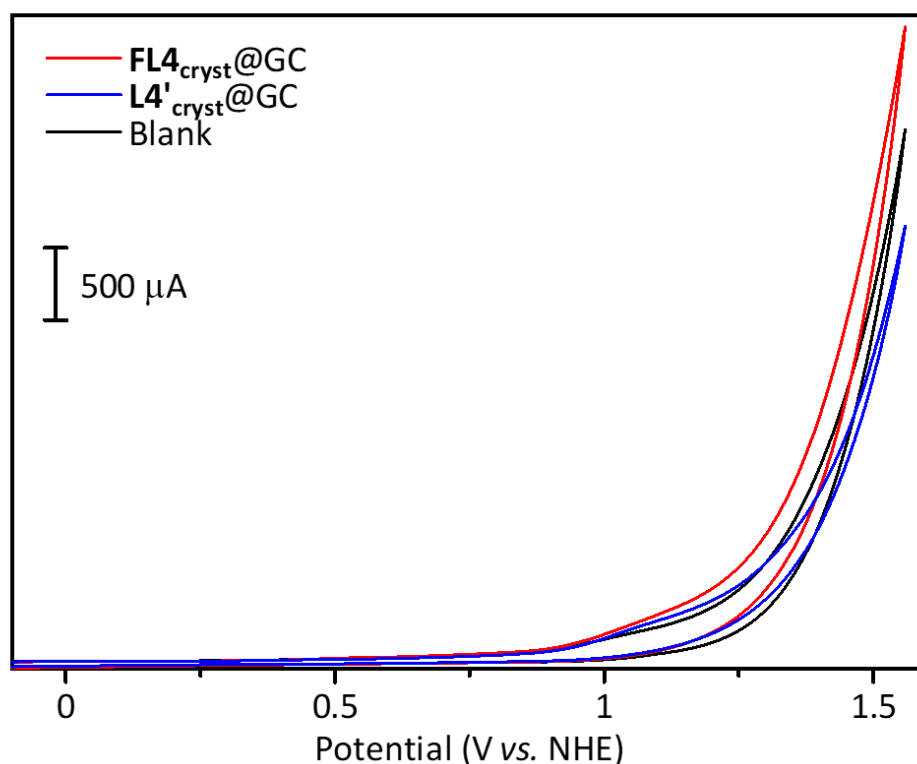


Figure 13. Cyclic voltammograms of **FL4**_{cryst}@GC (red line), **L4'**_{cryst}@GC and blank (black line) in a 0.2 M phosphate buffer (pH 7). Measurements were performed under Ar at a scan rate of 100 mV s⁻¹. Working electrode, glassy carbon; counter electrode, Pt wire; reference electrode, SCE. CV scans were initiated from the open-circuit potential.

Conclusion

In summary, two supramolecular frameworks based on cubane-shaped cobalt complexes were synthesized and characterized by single crystal X-ray diffraction measurement. The introduction of multi-point Ar-Ar^F interactions was a key to assembly the catalyst modules. In the crystalline state, two- and four-substituted complexes (**L2** and **L4**) gave porous structures (**FL2** and **FL4**) with large void spaces (>50% volume) via self-assembly. Electrochemical measurements revealed that only porous **FL4** showed catalytic activity for water oxidation where **L4'** did not show any activity.

Experimental section

Materials

All reagents were purchased from Tokyo Chemical Industry Co., Ltd., FUJIFILM Wako Pure Chemical Co., Kanto Chemical Co. Inc. and used without further purification if not mentioned. Unsubstituted cubane complex $\text{Co}_4\text{O}_4(\text{OAc})_4(\text{py})_4$ was synthesized according to published procedure.[11] Hppeb ligand was synthesized following literature procedures.[7a,10]

Measurements apparatus

^1H and ^{19}F NMR spectra were acquired on a JEOL JNM-LA400 spectrometer, where chemical shifts in acetone- d_6 was referenced to internal tetramethylsilane for ^1H nuclei (0.00 ppm) and external trifluoroacetic acid for ^{19}F nuclei (-76.55 ppm). Cyclic voltammograms were measured at room temperature on a Biologic SP-50 electrochemical analyser. Glassy carbons (disk and plate) and platinum wire were used as the working and auxiliary electrodes. Ag/Ag^+ electrode ($\text{Ag}/0.01 \text{ M AgNO}_3$) and saturated calomel electrode (SCE) were used as reference electrodes in organic and aqueous medium, respectively. The redox potentials were calibrated against the redox potential for the ferrocene/ferrocenium (Fc/Fc^+) couple in organic solvents and Normal hydrogen electrode (NHE, $\text{NHE} = \text{SCE} - 0.244 \text{ V}$) in aqueous solutions.

X-ray crystal structure analysis

Single crystal X-ray diffraction data were collected on a Rigaku MicroMax-007HF/XtalLAB SynergyCustom with confocal monochromated Mo-K α radiation ($\lambda = 0.71069 \text{ \AA}$) at 123 K. coated with Paratone-N (Hampton Research Corp., Aliso Viejo, CA, USA). Data was processed using CrysAlisPro system software.[13] The structure was solved by dual-space algorithm using SHELXT program[14] through the Olex2 interface.[15] All non-hydrogen atoms were refined anisotropically using a least-squares method, and hydrogen atoms were fixed at calculated positions and refined using a riding model. SHELXL-2014/7 was used for structure refinement.[16] Full-matrix least-squares refinements on F^2 based on unique reflections with unweighted and weighted agreement factors of $R = \sum||F_o| - |F_c||/\sum|F_o|$ ($I > 2.00 \sigma(I)$) and $wR = [\sum w(F_o^2 - F_c^2)^2/\sum w(F_o^2)^2]^{1/2}$ were performed. Mercury 4.0.0 was used for visualization and analysis of the structure.

Powder X-ray diffraction measurement

Powder X-ray diffraction data were collected on a Rigaku MicroMax-007HF/XtalLAB SynergyCustom with confocal monochromated Mo-K α radiation ($\lambda = 0.71069 \text{ \AA}$) at room temperature (20 K). The samples were filled in glass capillaries (outer diameter of 0.80 mm) with solvents and sealed with glue. Data was processed using CrysAlisPro system software[13] for background subtraction.

Synthesis of Co₄O₄(ppeb)₄(py)₄ (L4)

Co₄O₄(OAc)₄(py)₄ (100 mg, 0.117 mmol) and Hppeb (146 mg, 0.468 mmol) were added to 10 mL of MeCN. The mixture was heated at 80 °C overnight. The volatiles were removed under vacuum. The residue was purified by column chromatography over silica gel (CHCl₃:MeOH 95:5). Black needle crystals were obtained from CHCl₃/pentane (15 mg, 6.89%).

Synthesis of Co₄O₄(ppeb)₄(py)₄ (L4')

L4' was synthesized by different procedure: Co₄O₄(OAc)₄(py)₄ (100 mg, 0.117 mmol) and Hppeb (146 mg, 0.468 mmol) were added to 10 mL of MeCN. The mixture was heated at 80 °C for 2.5 h. 5 mL of toluene was added to the mixture and all volatiles were removed under vacuum. This process was repeated, and the residue was heated 80 °C for 2.5 h in 10 mL of MeCN. The volatiles were removed under vacuum. Resulted solid was purified by column chromatography over silica gel (CHCl₃:MeOH 95:5). Black needle crystals were obtained from CHCl₃/pentane (60 mg, 27.5%). ¹H NMR (acetone-*d*₆) δ 8.63 (d, J = 5.0 Hz, 8H), 8.01-8.04 (m, 8H), 7.75 (t, J = 7.5 Hz, 4H), 7.62 (d, J = 8.2 Hz, 8H), 7.24 (t, J = 6.9 Hz, 8H). ¹⁹F NMR (acetone-*d*₆) δ -137.20 (s, 1F), -138.95 (s, 1F), -154.73 (dd, J = 286.1, 23.8 Hz, 1F), -164.21 (td, J = 53.6, 27.8 Hz, 2F).

Synthesis of Co₄O₄(ppeb)₂(OAc)₂(py)₄ (L2)

Co₄O₄(OAc)₄(py)₄ (50 mg, 58.5 μmol) and Hppeb (149 mg, 0.479 mmol) were added to 5 mL of MeCN. The mixture was heated at 60 °C overnight. The volatiles were removed under vacuum. The residue was purified by column chromatography over silica gel (CHCl₃:MeOH 95:5). Black needle crystals were obtained from CH₂Cl₂/hexane.

References

- [1] (a) X. Liu, F. Wang, *Coord. Chem. Rev.* **2012**, *256*, 1115–1136. (b) A. Singh, L. Spiccia, *Coord. Chem. Rev.* **2013**, *257*, 2607–2622. (c) M. D. Kärkäs, O. Verho, E. V. Johnston, B. Åkermark, *Chem. Rev.* **2014**, *114* (24), 11863–12001. (d) J. D. Blakemore, R. H. Crabtree, G. W. Brudvig, *Chem. Rev.* **2015**, *115*, 12974–13005. (e) M. Kondo, S. Masaoka, *Chem. Lett.* **2016**, *45* (11), 1220–1231. (f) B. Zhang, L. Sun, *Chem. Soc. Rev.* **2019**, *48* (7), 2216–2264. (g) S. Ye, C. Ding, M. Liu, A. Wang, Q. Huang, C. Li, *Adv. Mater.* **2019**, *31* (50), 1902069. (h) Z. N. Zahran, Y. Tsubonouchi, E. A. Mohamed, M. Yagi, *ChemSusChem* **2019**, *12* (9), 1775–1793.
- [2] (a) A. J. Bard, M. A. Fox, *Acc. Chem. Res.* **1995**, *28* (3), 141–145. (b) E. Amouyal, *Sol. Energy Mater. Sol. Cells* **1995**, *38*, 249–276.
- [3] (a) K. N. Ferreira, T. M. Iverson, K. Maghlaoui, J. Barber, S. Iwata, *Science*, **2004**, *303*, 1831–1838. (b) T. J. Meyer, M. H. V. Huynh, H. H. Throp, *Angew. Chem. Int. Ed.* **2007**, *46* (28), 5284–5304.
- [4] (a) Y. Umena, K. Kawakami, J. Shen, N. Kamiya, *Nature* **2011**, *473*, 55–60. (b) J. Shen, *Annu. Rev. Plant Biol.* **2015**, *66*, 23–48. (c) N. Sakashita, H. C. Watanabe, T. Ikeda, K. Saito, H. Ishikita, *Biochemistry* **2017**, *56* (24), 3049–3057.
- [5] (a) G. Férey, *Chem. Soc. Rev.* **2008**, *37* (1), 191–214. (b) H. Furukawa, K. E. Cordova, M. O’Keeffe, O. M. Yaghi, *Science* **2013**, *341*, 1230444.
- [6] (a) K. Meyer, M. Ranocchiari, J. A. van Bokhoven, *Energy Environ. Sci.* **2015**, *8* (7), 1923–1937. (b) Q. Shao, J. Yang, X. Huang, *Chem. Eur. J.* **2018**, *24* (57), 15143–15155. (c) D. Li, H. Xu, L. Jiao, H. Jiang, *EnergyChem* **2019**, *1* (1), 100005.
- [7] (a) T. Itoh, M. Kondo, M. Kanaïke, S. Masaoka, *CrystEngComm* **2013**, *15* (31), 6122. (b) T. Itoh, M. Kondo, H. Sakamoto, K. Wakabayashi, M. Kanaïke, K. Itami, S. Masaoka, *Dalt. Trans.* **2015**, *44* (34), 15334–15342. (c) P. Chinapang, M. Okamura, T. Itoh, M. Kondo, S. Masaoka, *Chem. Commun.* **2018**, *54*, 1174–1177.
- [8] (a) N. S. McCool, D. M. Robinson, J. E. Sheats, G. C. Dismukes, *J. Am. Chem. Soc.* **2011**, *133* (30), 11446–11449. (b) J. Li, Y. Jiang, Q. Zhang, X. Zhao, N. Li, H. Tong, X. Yang, L. Xia, *RSC Adv.* **2017**, *7* (7), 4102–4107. (c) Y. Wang, F. Li, X. Zhou, F. Yu, J. Du, L. Bai, L. Sun, *Angew. Chem. Int. Ed.* **2017**, *56* (24), 6911–6915.
- [9] (a) J. H. Williams, *Acc. Chem. Res.* **1993**, *26* (11), 593–598. (b) C. R. Partrick, G.

- S. Prosser, *Nature* **1960**, *187*, 1021.
- [10] (a) W. B. Austin, N. Bilow, W. J. Kelleghan, K. S. Y. Lau, *J. Org. Chem.* **1981**, *46* (11), 2280–2286. (b) Z. Yadong, W. Jianxun, *J. Fluor. Chem.* **1990**, *47*(3), 533–535. (c) A. Schaate, P. Roy, T. Preuße, S. J. Lohmeier, A. Godt and P. Behrens, *Chem.–Eur. J.* **2011**, *17* (34), 9320–9325.
- [11] R. Chakrabarty, S. J. Bora, B. K. Das, *Inorg. Chem.* **2007**, *46* (22), 9450–9462.
- [12] A. I. Nguyen, J. Wang, D. S. Levine, M. S. Ziegler, T. D. Tilley, *Chem. Sci.* **2017**, *8* (6), 4274–4284.
- [13] CrysAlisPro, Oxford Diffraction Ltd., Version 1.171.39.46.
- [14] G. M. Sheldrick, *Acta Cryst.* **2015**, *A71*, 3-8.
- [15] O. V. Dolomanov, L. J. Bourhis, R. J. Gildea, J. A. K. Howard and H. Puschmann, *J. Appl. Crystallogr.* **2009**, *42*, 339-341.
- [16] G.M Sheldrick., *Acta Cryst.* **2015**, *C71*, 3-8.

Concluding Remarks

The research described in this thesis has investigated the construction of function-integrated systems for electrochemical water oxidation. Chapter 1 demonstrates a novel approach for developing artificial catalytic systems for water oxidation *via* electrochemical polymerization. The introduction of carbazole moieties as charge transporting units enables direct electrochemical polymerization of a Co-based water oxidation catalyst molecule. The polymer-based catalyst system exhibits high catalytic activity. The discovery offers an important concept for the development of efficient artificial water oxidation systems.

Chapter 2 describes a Ru-based electrocatalytic water oxidation system derived from electrochemical polymerization. The key to the success is integrating charge-transporting units close to the catalytic center. The Ru-complex-based polymer shows significant enhancement of catalytic ability compared with a discrete molecular system. The result shows the potential applicability of the current strategy.

Chapter 3 presents the construction of supramolecular frameworks by the self-assembly of Co-based catalysts. The introduction of multi-point Ar-Ar^F interactions provides infinite well-defined pores which can work as mass transporting paths. The development of structure-regulated catalysts with permanent porosity attracting considerable interest for efficient catalysis.

Collectively, these results suggest the significance of function-integrated approaches for artificial water oxidation. Catalytic performance can be improved by the incorporation with or into additional functional units, and proper modification provides simple fabrication methods. The results in this thesis may give useful insights into function-integrated catalyst systems.

Acknowledgements

This thesis summarizes my Ph.D studies from April 2018 to March 2021 at the Department of Structural Molecular Science, School of Physical Sciences, the Graduate University for Advanced Studies (SOKENDAI) under the direction of Dr. Shigeyuki Masaoka, Associate Professor of SOKENDAI (the present Professor of the Graduate School of Engineering, Osaka University).

First of all, I would like to show my greatest appreciation to Professor Shigeyuki Masaoka and Associate Professor Mio Kondo for their gracious care, precise guidance, and warm encouragement. I have the really good fortune to join Masaoka group and research in a wonderful environment. I could never complete my Ph.D course without their supports.

I am grateful to Associate Professor Genki Kobayashi and Ms. Ai Suzuki for the generous permission of the administrative supports in Institute for Molecular Science.

I would like to express my appreciation to Associate Professor Tetsuro Kusamoto and Assistant Professor Ryota Matsuoka for their kind helps and supports to use single crystal X-ray diffraction instruments.

I am grateful to staff in Instrument Center (Institute for Molecular Science), Mr. Osamu Ishiyama and Ms. Aya Toyama for their helps and supports in SEM-EDX measurements.

I would like to express my gratitude to current and alumni of Masaoka group, Dr. Masaya Okamura, Dr. Vijayendran K. K. Praneeth, Dr. Yuki Okabe, Dr. Pondchanok Chinapang, Dr. Lee Sze Koon, Dr. Yutaka Saga, Dr. Arisa Fukatsu, Dr. Takafumi Enomoto, Dr. Hitoshi Izu, Mr. Kento Kosugi, Mr. Masahiro Tasaki, Mr. Takuya Akai, Mr. Soshi Kato, Mr. Ryo Tomiyasu, Mr. Hirotaka Hamaguchi, Mr. Hayato Tatewaki, Mr. Yusuke Nakayama, Mr. Shinki Fujisawa, Mr. Nozomi Yamaguchi, Mr. Taito Watanabe, Mr. Shangxing Li, Ms. Mami Kachi, Ms., Misa Tomoda, Ms. Mayu Fujisawa, Ms. Mei Ishihara, Ms. Chiharu Akatsuka, Ms. Kanako Okuda, and Ms. Hina Kashima for their kind friendship and precious discussions. I also appreciate the secretaries, Ms. Mayuko Taniwake, Ms. Kyoko Nogawa, Ms. Kyoko Kawashima, and Ms. Kiyomi Lee for administration supports. I would like to thank the technician staff, Ms. Miho Matsuda for the assistance with laboratory management. My special thanks are due to Dr. Hitoshi Izu who always encourages me and discusses a lot and Ms. Mayu Fujisawa who advances the research with me from the beginning.

I would like to acknowledge Professor Masahiro Yamashita for giving me advises and encouragement to continue my research. I would also like to thank staff and members of Yamashita group for their discussions and friendships even after I left the group.

I would like to thank Mr. Ryosuke Tanii and Mr. Kohei Kawano for their kind friendship which gives me a pleasant time in Okazaki. I would also like to acknowledge Dr. Kiyohiro Adachi for his friendly and helpful advises especially on crystallography.

I would like to thank for the financial support from IMS SRA and RA work at Osaka University during my Ph.D course.

After all, my deepest appreciation goes to my parents, Masayuki Iwami and Miyako Iwami, and my brother, Ryota Iwami for immense supports of my life and heartfelt encouragements throughout my Ph.D course.

List of Publications

Chapter 1

“Electrochemical Polymerization Provides a Function-Integrated System for Water Oxidation”

Hikaru Iwami, Masaya Okamura, Mio Kondo, Shigeyuki Masaoka

Angew. Chem. Int. Ed. **2021**, *in press*.

Chapter 2

“Facile Construction of Function-Integrated Water Oxidation System via Electrochemical Polymerization”

Hikaru Iwami, Mio Kondo, Shigeyuki Masaoka

Manuscript in preparation.

Chapter 3

“Construction of Self-Assembled Frameworks of Cubane-Type Tetranuclear Cobalt Complexes”

Hikaru Iwami, Mayu Fujisawa, Mami Kachi, Tetsuro Kusamoto, Mio Kondo, Shigeyuki Masaoka

Manuscript in preparation.

Other Publications

- [1] “Metal-Organic Framework of Lanthanoid Dinuclear Clusters Undergoes Slow Magnetic Relaxation”
Hikaru Iwami, Ryo Nakanishi, Yoji Horii, Keiichi Katoh, Brian K. Breedlove, Masahiro Yamashita, *Materials* **2017**, *10* (1), 81.
- [2] “Cocrystals of Li⁺ Encapsulated Fullerenes and Tb(iii) Double-Decker Single Molecule Magnet in a Quasi-Kagome Lattice”
Hikaru. Iwami, Junfei Xing, Ryo Nakanishi, Yuji Horii, Keiichi Katoh, Brian K. Breedlove, Kazuhiko Kawachi, Yasuhiro Kasama, Eunsang Kwon, Masahiro Yamashita, *Chem. Commun.* **2020**, *56* (84), 12785–12788.
- [3] “Rational Synthetic Strategy for Heterometallic Multinuclear Complexes”Hitoshi Izu, Mio Kondo, Yutaka Saga, **Hikaru Iwami**, Shigeyuki Masaoka, *Chem. Lett.* **2020**, *49* (2), 125-128.
- [4] “Modulation of Self-Assembly Enhances the Catalytic Activity of Iron Porphyrin for CO₂ Reduction”, *Small*, *accepted*.
Masahiro Tasaki, Yuki Okabe, **Hikaru Iwami**, C. Akatsuka, K. Kosugi, K. Negita, S. Kusaka, R. Matsuda, Mio Kondo, Shigeyuki Masaoka,

